



HAL
open science

Electrical impedance tomography for void fraction measurements of harsh two-phase flows: prototype development and reconstruction techniques

Antoine Dupre

► **To cite this version:**

Antoine Dupre. Electrical impedance tomography for void fraction measurements of harsh two-phase flows: prototype development and reconstruction techniques. Fluids mechanics [physics.class-ph]. Ecole Centrale Marseille, 2017. English. NNT : 2017ECDM0005 . tel-01656977

HAL Id: tel-01656977

<https://theses.hal.science/tel-01656977>

Submitted on 6 Dec 2017

HAL is a multi-disciplinary open access archive for the deposit and dissemination of scientific research documents, whether they are published or not. The documents may come from teaching and research institutions in France or abroad, or from public or private research centers.

L'archive ouverte pluridisciplinaire **HAL**, est destinée au dépôt et à la diffusion de documents scientifiques de niveau recherche, publiés ou non, émanant des établissements d'enseignement et de recherche français ou étrangers, des laboratoires publics ou privés.

École Doctorale : Physique et sciences de la matière (ED352)
Laboratoire d'Hydromécanique des cœurs et circuits, CEA Cadarache

THÈSE DE DOCTORAT

pour obtenir le grade de
DOCTEUR de l'ÉCOLE CENTRALE de MARSEILLE

Discipline : Instrumentation

ELECTRICAL IMPEDANCE TOMOGRAPHY FOR VOID FRACTION MEASUREMENTS OF HARSH TWO-PHASE FLOWS : PROTOTYPE DEVELOPMENT AND RECONSTRUCTION TECHNIQUES

par

DUPRE Antoine

Directeurs de thèse : BOURENNANE Salah, RICCIARDI Guillaume

Soutenue le 10 octobre 2017

devant le jury composé de :

H-M. Prasser	Professeur, ETH Zürich	Président du jury
B.M.E. Moldestad	Professeure, University College of Southeast Norway	Rapporteur
L. Rossi	Expert senior, CEA	Rapporteur
C. Bellis	Chargé de recherche, LMA CNRS	Examineur
S. Mylvaganam	Professeur, University College of Southeast Norway	Examineur
S. Bourennane	Professeur, Ecole Centrale Marseille	Directeur de thèse
G. Ricciardi	Expert senior, CEA	Examineur

Abstract

Recent developments with data acquisition equipment have reduced the time required for image acquisition with electrical tomography, thereby bringing new opportunities for the study of fast-evolving two-phase flows. Amongst the numerous advantages of this imaging technique for multiphase flow related research are non-intrusiveness, high acquisition rates, low-cost and improved safety. A set of electrodes placed on the periphery of the pipe to be imaged is used to impose an electrical excitation and measure the system response. The distribution of phases inside the study volume distorts the electrical field in a characteristic manner. The objective of this thesis is to assess the potential of electrical impedance tomography at high acquisition rate. The first stage consists in developing a prototype sensor and assessing its performance with simplistic experiments. The system architecture employs voltage control of the excitation and therefore does not require the implementation of the conventional voltage-to-current converter module. A novel data collection method, the full scan strategy, is considered and provides correcting factors for the parasitic impedances in the system. The second stage is the image reconstruction from the measurement data. The approach considered in the thesis is to assume that flow regime identification techniques may provide valuable information on the phase distribution that can be injected in the inverse problem for imaging, thereby tackling the challenge of the non-linearity of the inverse problem. A method for horizontal air-water flow regime identification has been elaborated with an electrical capacitance tomography sensor and multiphase flow rig tried and tested. It is being adapted to the fast electrical impedance tomography prototype and upgraded to include vertical flow regimes. In parallel, an image reconstruction method has been developed based on the NOSER algorithm and a pseudo-2D postulate. The analysis of the reconstructed images for a set of benchmark experiments provide insights on the merits and deficiencies of the algorithm and of the prototype.

Key words: Electrical Impedance Tomography, Instrumentation, Two-phase Flows, Void Fraction

Résumé

Les récentes avancées technologiques des matériels d'acquisition de données ont permis de réduire le temps d'acquisition d'image en tomographie électrique, ce qui offre des opportunités pour l'étude des écoulements diphasiques transitoires. Parmi les nombreux atouts de cette technique d'imagerie d'écoulements diphasiques, on peut citer son caractère non-intrusif, sa haute fréquence d'acquisition, son faible coût et sa fiabilité en termes de sûreté. Un ensemble d'électrodes placées sur le pourtour d'une conduite servent à transmettre une excitation électrique au milieu et à le sonder. Ainsi, la distribution des phases perturbe les champs électriques de manière caractéristique. L'objectif de cette thèse est d'évaluer le potentiel de la tomographie d'impédance électrique rapide. La première étape consiste au développement d'un prototype de capteur et à l'évaluation de sa performance par des essais simplifiés. L'architecture du système utilise un contrôle en potentiel du signal d'excitation et ne nécessite donc pas d'implémenter un module de conversion tension-courant. La seconde étape est la reconstruction de l'image à partir des données mesurées. L'approche qui a été considérée est de supposer une image approchée de la distribution des phases grâce à une identification du régime d'écoulement. Ainsi, le défi de résoudre un problème inverse fortement non-linéaire est simplifié. Une méthode d'identification de régimes d'écoulements horizontaux eau-air a été élaborée avec un module de tomographie de capacitance électrique et une boucle d'essais hydrauliques déjà éprouvés. Cette technique est en cours d'adaptation au prototype de tomographie d'impédance électrique rapide et en amélioration grâce à l'inclusion des régimes d'écoulements verticaux. En parallèle, une méthode de reconstruction d'image a été développée, basée sur l'algorithme NOSER et un postulat pseudo-2D. L'analyse des images reconstruites à partir d'un set d'expériences de référence procure un aperçu des avantages et des défauts de la méthode et du prototype.

Mots clefs : Tomographie d'impédance électrique, Instrumentation, Ecoulements diphasiques, Taux de vide

Contents

Abstract (English/Français)	i
List of figures / List of tables	vii
1 Introduction	1
2 Prototype development	5
2.1 Overview of instrumentation for flow imaging	5
2.1.1 Characteristic length and time scales of multiphase flows	5
2.1.2 Main imaging techniques	6
2.1.3 Electrical tomography techniques	9
2.2 Overview of electrical impedance tomography	12
2.2.1 Electromagnetism and forward problem	12
2.2.2 Basic principle of data collection for EIT	14
2.2.3 Towards high frame acquisition rates	17
2.3 Hardware	19
2.3.1 Test section	19
2.3.2 Electrodes	21
2.3.3 Signal generation and data acquisition	24
2.3.4 Multiplexing	25
2.4 Software and procedures	28
2.4.1 Excitation signal	28
2.4.2 Data collection strategy	28
2.4.3 Digital signal processing	29
2.4.4 Full procedure for fast EIT	31
2.5 Performance assessment of ProME-T	34
2.5.1 Noise and uncertainties in signals of ProME-T	34
2.5.2 Repeatability of the EIT measurements	36
2.5.3 Comparison with analytical and numerical solutions	39
2.5.4 Acquisition of image sequence in fast mode	41
2.6 Studies for fundamental understanding	43
2.6.1 Signal settling time	43
2.6.2 Electrode-electrolyte contact impedance	44
2.6.3 Calibration procedure for impedance mismatch	49

Contents

3	Flow regime identification	53
3.1	Overview of flow regime identification	53
3.1.1	Multiphase flow regimes	53
3.1.2	Flow regime identification	56
3.1.3	Research with electrical tomography	57
3.2	Experimental setup and campaign	59
3.2.1	Multiphase flow rig	59
3.2.2	Instrumentation and ECT sensor	61
3.2.3	Experiments	62
3.3	Methodology for identification	66
3.3.1	Data collection strategy of raw ECT signal	66
3.3.2	Time series analysis for extracting dynamical features	67
3.3.3	Eigenvalues analysis for extracting geometrical features	68
3.4	Results	71
3.4.1	Intermittent against continuous flows	72
3.4.2	Annular against stratified flows	72
3.4.3	Stratified smooth against wavy flows	73
3.4.4	Plug against slug flows	75
3.5	Extended methodology with simulations	79
3.5.1	Numerical model and simulations	79
3.5.2	Numerical validation of the criteria	80
3.5.3	Estimation of phase fractions	82
3.5.4	Adaptation to ProME-T EIT sensor	83
4	Imaging	89
4.1	Overview of EIT image reconstruction	89
4.1.1	Inverse problem	90
4.1.2	Regularisation	92
4.1.3	Image segmentation techniques	93
4.2	Two-phase flow imaging method	95
4.2.1	Forward problem with EIDORS solver	95
4.2.2	3D inversion with NOSER algorithm	98
4.2.3	Pseudo-2D image reconstruction	101
4.3	Assessment of reconstruction images	102
4.3.1	Benchmark experiments	102
4.3.2	Cross-sectional average phase fraction	103
4.3.3	Comparing adjacent, opposite and full scan strategies	103
5	Conclusion	107
	Bibliography	118
	Appendix	119

List of Figures

2.1	Bubble-size histogram in fast pressure transient experiment. Adapted from Nakath et al. (2013)	6
2.2	Flow measurement downstream of heating section, $P=7.7$ bar, $G=300 \frac{kg}{m^2 s}$, $\Delta T_{sub} = 35^\circ C$, $q=7.64 \frac{kW}{m^2}$. Adapted from Park (2013)	6
2.3	Principle of the ROFLEX sensor. Adapted from Hampel et al. (2016)	8
2.4	Typical echo sequence of MRI. Adapted from Joseph-Mathurin et al. (2010)	8
2.5	Wire-mesh sensor with orthogonal sets of transmitter and receiver wire-electrodes. Adapted from www.hzdr.de	9
2.6	Most sensitive configurations to detect centre region of the model for neighbouring, opposite, cross and adaptive strategies. The black lines indicate the delimitation between zones of positive and negative sensitivity. Adapted from Kauppinen et al. (2006)	16
2.7	Illustrations of adjacent (left), opposite (middle) and cross (right) data collection strategies	16
2.8	Picture of the ProME-T prototype sensor	20
2.9	CAD models of the test section in 3D configuration (left) and 2D configuration (right)	20
2.10	Side view of the test section	21
2.11	System for positioning of rods	21
2.12	Simulation of total impedance for each of 120 excitation patterns, for different heights of the test section: $Z=2, 10, 200$ mm	22
2.13	Two illustrative cases of misplacement of electrodes	23
2.14	Outline schematic of the ProME-T hardware - test section, multiplexing circuit and PXI card with the coupling leads to the test section with electrodes	24
2.15	3D CAD model of the PCB board used in multiplexing	26
2.16	Wiring details (schematic) of the PCB board used in multiplexing	27
2.17	Wiring details (integration) of the PCB board used in multiplexing	27
2.18	Flow diagram of frame acquisition procedure with ProME-T	33
2.19	10 periods of low and high amplitude signals	35
2.20	Spectra of high and low amplitude signals for a 1 Volt 5 kHz excitation	36
2.21	THD and SNR of signals on 16 measurement channels for 1 V_{AC} 5 kHz excitation	37
2.22	Relative standard deviation of repeated identical measurements	38
2.23	Comparison of analytical, numerical solutions and measurements on 16 channels	40

List of Figures

2.24	Comparison of numerical, analytical voltage profiles and experimental prediction	41
2.25	Image sequence at 667 fps of two gravitationally falling spheres: on the left, S_1 with $D_1=22$ mm, $\rho_1=5697$ kg·m ⁻³ ; on the right, S_2 with $D_2=25$ mm, $\rho_2=1144$ kg·m ⁻³	42
2.26	Illustration of settling signals in the four categories	44
2.27	Analysis of the settling of signals in the four categories in terms of relative error	45
2.28	Electrical circuit model of the EIT system	46
2.29	Modulus of impedance response of global impedance for various liquid conductivities	46
2.30	Phase of impedance response of global impedance for various liquid conductivities	47
2.31	Conductivity dependence of the indicators R_t and $X_t(1\text{Hz})$	48
2.32	Attenuation of capacitive effects with increasing excitation frequency	49
2.33	Measured and calibrated impedance (3D)	51
2.34	Measured and calibrated impedance (2D)	51
3.1	Sketches of flow regimes for flow of air/water mixtures in a horizontal, 5.1cm diameter pipe. Adapted from Brennen (2005)	54
3.2	Flow regime map for the horizontal flow of an air/water mixture in a 5.1 cm diameter pipe. Hatched regions are observed regime boundaries, lines are theoretical predictions. Adapted from Brennen (2005)	55
3.3	Sketches of flow regimes for two-phase flow in a vertical pipe. Adapted from Brennen (2005)	55
3.4	The vertical flow regime map of Hewitt and Roberts (1969) for flow in a 3.2 cm diameter tube, validated for both air/water flow at atmospheric pressure and steam/water flow at high pressure. Adapted from Brennen (2005)	56
3.5	P&ID of the multiphase flow loop with ECT and GRM	60
3.6	Photograph of the multiphase flow loop with ECT and GRM	60
3.7	Test section with sensor placements, transparent section for high-speed camera based studies, multi-modal tomographic systems and differential pressure transmitters	60
3.8	Twin plane ECT tomographic system – Arrays of 12 electrodes on the periphery of the pipe section with stratified flow in this schematic, $C_{a,b}$ is the capacitance between electrodes a and b, with a,b = 1,2,...,12	62
3.9	Set of 115 experiments in the horizontal configuration, and the flow regimes as identified by experimental means (visual observation, GRM and high-speed camera recordings)	63
3.10	Images of typical flow regimes (a) stratified smooth (b) low frequency waves (c) high frequency waves (d) annular (e) rear, bulk, and front of a plug (f) rear, bulk, and front of a slug	65

3.11	Representative arrays of 12 eigenvalues of the \mathbf{C}_{mean} matrix for annular (in red), stratified (in blue), intermittent flows (in green) and homogeneous flow (in black), obtained by averaging over the 115 measurements in the database. Error bars indicate standard deviation in the data set	70
3.12	Representative arrays of 12 eigenvalues of the \mathbf{C}_{SD} matrix for annular (in red), stratified (in blue), intermittent flows (in green) and homogeneous flow (in black), obtained by averaging over the 115 measurements in the database. Error bars indicate standard deviation in the data set	70
3.13	Flow diagram for regime identification method	71
3.14	Parameter and indicator for <i>Criterion I</i> , on flow regime map	72
3.15	Parameter and indicator for <i>Criterion II</i> , on flow regime map	73
3.16	Spectra of normalised capacitance measurement $\hat{C}_{12,12}$ in 3 experiments: stratified smooth (blue), transitional (green) and stratified wavy (red) flows. The 5 Hz cut-off frequency empirically set is indicated in black	74
3.17	Illustrative example of slow instabilities	75
3.18	Signal of the γ -ray densitometer for low frequency intermittent flow	75
3.19	Parameter and indicator for <i>Criterion III</i> , on flow regime map	76
3.20	Spectra of normalised capacitance measurement $\hat{C}_{3,5}$ in 3 experiments: plug (blue), transitional (green) and slug (red) flows. The 10 Hz cut-off frequency empirically set is indicated in black	77
3.21	Parameter and indicator for <i>Criterion IV</i> , on flow regime map	78
3.22	2D FEMM model of the ECT sensor, and mesh, illustrated for example of wavy flow	79
3.23	Array of 12 eigenvalues λ_{mean} for stratified flows with various water fill levels .	82
3.24	Relationship between the cross-sectional averaged water fraction (WF) and the sum of eigenvalues $\sum_{i=1}^{12} \lambda^{(i)}$, for stratified flows	83
3.25	Sensitivity of the estimate for cross-sectional averaged water fraction (WF) to the sum of eigenvalues $\sum_{i=1}^{12} \lambda^{(i)}$	84
3.26	Relationship between the cross-sectional averaged water fraction (WF) and the leading eigenvalue $\lambda^{(12)}$, for annular centred flows	84
3.27	Pictures of the two extreme experiments in terms of WF: 48% (left) and 97% (right)	85
3.28	15 first elements of the array of eigenvalues λ for annular flows with different water fraction	86
3.29	Relationship between the cross-sectional averaged water fraction (WF) and the sum of the 15 eigenvalues $\sum_{i=1}^{15} \lambda^{(i)} $, for annular centred flows	86
3.30	CAD schematic of the new EIT sensor array and test section: 16 electrodes in yellow/orange, seals in red, test section made of PMMA in gray. Connections to the EIT modules are not shown.	87
4.1	Accuracy of simulations for meshes with various levels of refinement (varying $\text{maxsz}_{\text{cyl}}$)	97
4.2	Accuracy of simulations for meshes with various levels of refinement (varying $\text{maxsz}_{\text{elec}}$)	97

List of Figures

4.3	L-curve method for assessing optimal regularisation parameter. Adapted from Wei et al. (2015)	99
4.4	Benchmark experiments result: real image on the left and reconstructed tomographic image on the right	103
4.5	Void fraction estimate from measurements, and real void fraction	104
5.1	Schematic of EMFT sensor. Adapted from Leeungculsatien and Lucas (2013) . .	109

List of Tables

2.1	Comparison table of 3 fast EIT systems	39
3.1	Summary table of the four criteria for eigenvalue based flow regime detection .	71
3.2	Numerical FEMM models, normalised capacitance matrices and arrays of eigenvalues, for each simulation of case study	81
4.1	Linear back projection and other inverse reconstruction algorithms. Adapted from Wei et al. (2015).	93
4.2	Set of images obtained with 5 inversion matrices ($\lambda_{reg}=0.00, 0.01, 0.05, 0.10$ and 0.40). On the left, large cylinder ex-centred; on the right, large cylinder centred	100
4.3	Comparative table of adjacent, opposite and full scan data collection strategies	104

Abbreviations

AT3NA	Algorithme de Tomographie en 3D NOSER et Aplanissement (French)
CAD	Computer aided design
CT	Computed Tomography
DFT	Discrete Fourier transform
ECT	Electrical capacitance tomography
ERT	Electrical resistance tomography
EIDORS	Electrical Impedance Tomography and Diffuse Optical Tomography Re- construction Software
EIT	Electrical impedance tomography
FEM	Finite element methods
FEMM	Finite element method magnetics
fps	frames per second
FRI	Flow regime identification
GRM	Gamma-ray meter
LBP	Linear back projection
MRI	Magnetic resonance imaging
NOSER	Newton's one-step error reconstruction
OZS	Over-zero-switching scheme
PCA	Principal component analysis
PCB	Printed circuit board
PDF	Probability distribution function
PMMA	Polymethyl methacrylate
ProME-T	Prototype pour Mesures Electriques par Tomographie (French)
PSD	Power spectral density
SNR	Signal to noise ratio
THD	Total harmonic distortion
UCSN	University College of Southeast Norway
VCCS	Voltage controlled current source
WF	Water fraction

Notations and Symbols

A	Some square matrix
A_{eff}	Effective area for current flow in 1D model
A_l	Surface of electrode-electrolyte contact area
A_{lin}	Linear contribution to the derivative of the Jacobian matrix
A_{nl}	Non-linear contribution to the derivative of the Jacobian matrix
\vec{B}	Magnetic induction field
C	Capacitance matrix
$C_{a,b}$	Capacitance between electrodes a and b
$\hat{C}_{a,b}$	Normalized capacitance between electrodes a and b
C_x	Drag coefficient
C_{mean}	Capacitance matrix of mean of signals
C_{SD}	Capacitance matrix of standard deviation of signals
C_{LP_{kHz}}	Capacitance matrix of low-pass filtered signals
C_{HP_{kHz}}	Capacitance matrix of high-pass filtered signals
Δf	Frequency resolution of DFT
$\partial\Omega$	Periphery/boundary of the study volume Ω
\vec{D}	Electrical displacement field
D_{in}	Inner diameter of the ECT sensor
D_{out}	Outer diameter of the ECT sensor
dL	Misalignment of electrodes in 1D model
η_C	Sensitivity of the ECT sensor array
ϵ	Electrical permittivity
ϵ_0	Vacuum permittivity
ϵ_R	Relative permittivity of a medium
\vec{E}	Electrical field
E_l	Electrode number l
ϕ	Objective function of least-square method
f_{acq}	Sampling frequency for acquisition
f_{ECT}	Frame acquisition rate of ECT sensor
f_{exc}	Frequency of excitation signal
f_{fps}	Frame acquisition rate

List of Tables

γ	Electrical complex conductivity
G	Conductance
\hat{G}	Normalised conductance
\mathbf{G}	Conductance matrix
\vec{H}	Magnetic H-field
H	Axial separation of two rings of electrodes
$\mathbf{HP}_{x\text{kHz}}$	High-pass filter operator with cut-off frequency of x kHz
I	Electrical current
I_l	Electrical current at the electrode E_l
i	Unit imaginary number
$iRtR$	Sparse permutation matrix of the mesh
iRN	Regularisation matrix
\vec{J}	Electrical current field
$J _{\partial\Omega}$	Neumann boundary condition
\vec{J}_m	Lead field of current injection
\vec{J}_n	Lead field of voltage measurement
Jac	Jacobian matrix
λ_A	Set of eigenvalues of \mathbf{A} : $\{\lambda_A^{(i)}, i = 1, 2, \dots, 12\}$
λ_{reg}	Control parameter of the regularisation
L	Separation between electrodes in 1D model
$\mathbf{LP}_{x\text{kHz}}$	Low-pass filter operator with cut-off frequency of x kHz
L_C	Separation between sets of arrays of the ECT module
l_C	Length of electrodes of the ECT sensor
$maxsz_{cyl}$	Maximum size of mesh elements (cylinder)
$maxsz_{elec}$	Maximum size of mesh elements (electrodes)
mean	Mean operator
ν	Outward unit normal to the boundary
N_f	Number of frames per acquisition sequence
N_{mesh}	Mesh cells in the forward model
N_p	Number of periods per excitation pattern
N_s	Number of samples per excitation pattern
N_{spp}	Number of samples per period of the excitation signal
\vec{n}	Tangent to an infinitesimal surface
n_C	Number of electrodes of the ECT sensor
Ω	Study volume
Ω_k	Volume of element k of the mesh
ω	Angular frequency
Q	Electrical charge on an electrode
P	Parameter of a criterion

P_{reg}	Penalty term of the regularisation
ρ_v	Electrical charge density
R	Electrical resistance
R_{add}	Additional resistance in 1D model
RM	Inversion matrix in 3D
RM'	Inversion matrix in 2D
RMS_{rc}	Root mean square of relative changes
R_s	Sense resistor
R_t	Resistive component of Z
σ	Electrical conductivity
σ_b	Surface of electrode b
SD	Standard deviation operator
S	Sensitivity coefficient
$S(E_i, E_j)$	Excitation pattern with E_i as source and E_j as drain
S_i	Set of excitation patterns, $i=1,2,\dots,120$
τ	Transit time of the dispersed phase between two rings of electrodes
T	Threshold of a criterion
V	Electrical (scalar) potential
\hat{V}_i	Normalized voltage measurement on channel $n^\circ i$
$V _{\partial\Omega}$	Dirichlet boundary condition
V_i	Voltage measured on channel $n^\circ i$
V_{mea}	Set of voltages in the measurement frame
V_{ref}	Set of voltages in the reference frame
V_{sim}	Simulated set of voltages
\vec{v}_A	Set of eigenvectors of \mathbf{A}
v_{term}	Terminal velocity
v_z	Axial velocity of the dispersed phase
w_C	Width of electrodes of the ECT sensor
X_t	Reactive component of Z
x	Some point in the study volume Ω
x^{DFT}	DFT of sampled signal x^{sig}
x^{sig}	Sampled signal
Z	Total impedance of the EIT system
Z^{bulk}	Bulk impedance of the medium
Z^{drain}	Drain electrode-specific impedance
Z_{S_i}	Total impedance for the i^{th} excitation pattern
Z^{source}	Source electrode-specific impedance

1 Introduction

Background

Tomography refers to the imaging of a volume. The word is derived from ancient Greek: *τομή*, *tomi* for a volume or a section, and *γράφω*, *grafo* for writing. The underlying feature of tomography is the study of an excitation generated outside the boundary and interacting with the medium inside the volume. The science has emerged with the use of X-ray radiation as an extension of radiography. The discovery of X-rays by Röntgen in 1895 rapidly led to the birth of radiology as a medical imaging technique. Typically, X-rays are generated by the Bremsstrahlung effect. A voltage being set between an anode and cathode in a vacuum tube, stream of electrons are directed toward the anode where the sudden deceleration by collision generates electromagnetic radiation at wave-length corresponding to X-rays. The radiation propagates within the study volume or human body to a detector. In the early stage of radiology, a photographic film would be used to develop an image. Yet, each pixel would contain the condensed information on the material properties integrated along the transmission path of the rays, *i.e.* a projection. In other words, shadow effects were (and still are) challenging for the interpretation of radiographies. The earlier proposition of tomography could be traced back to Italian radiologist Alessandro Vallebona (Kevles, 1997) and his proposal of focal plane tomography. Moving synchronously and in opposite directions both the source and the detector, the optical focus is kept at the focal plane while the contribution of out-of-focus zones is effectively cancelled out. The mathematical foundations of the computed tomography have been formulated by Austrian mathematician Johann Radon (Radon, 1986). The contribution of each pixel in a cross-sectional image is obtained by the Radon transform of a set of line integrals obtained with multiple projections. Considerations of image acquisition speed led to new generations of radiation-based tomography, with multiple sensors and/or detectors. The principle of tomography has been applied in various research fields: geophysics, material sciences, archaeology, etc. Different types of excitations have been used: radiation (X-rays, γ -rays), pressure waves (sounds and ultrasounds), etc. Amongst others, low-frequency electrical currents brings interesting perspectives for flow monitoring research and industrial applications.

Chapter 1. Introduction

Multiphase flows are frequently encountered in many research fields and industrial applications. Understanding their dynamical evolution is important to assess heat transfer, fluid-structure interactions or reaction kinetics. A single phase flow is characterised by the density and velocity fields. The conservation of mass, momentum and energy provides the equations describing the dynamics. Viscous effects can play an important role. Single phase flows are frequently sorted into the laminar, intermediate and turbulent categories according to their Reynolds number. The comprehension of multiphase flows is more complex since interaction between phases needs to be taken into account. The topology of multiphase flows are relatively few and dependent on the prevailing rheological mechanisms. The basic approach of considering homogeneously mixed phases frequently fails and tomographic measurements are essential in order to provide reliability in identifying flow regimes and their characterisations. Imaging a multiphase flow consists in measuring the distribution of phases and provides information on the phase indicator functions. If either the spatial or temporal resolution cannot match the characteristic time and length scales of the flow under investigation, the locally space-averaged or time-averaged phase fraction takes a value in the range between 0 and 1. For gas-liquid two phase flows, this is often referred to as void fraction.

In imaging of multiphase flows, a high frame rate and fine spatial resolution are desirable. Instrumentation techniques can be categorised according to their intrusiveness. Intrusive sensors such as optical probes or wire-mesh do not necessarily perturb the flow significantly. However, their integration in high pressure high temperature flow facilities raises complex challenges. In some industrial applications, compatibility with harsh flows is required. Electrical Impedance Tomography (EIT) is an instrumentation technique for non-intrusive imaging of the distribution of the electrical properties of a medium (conductivity and/or permittivity). Under assumptions appropriate for specific experiments, this result can be transposed into images of phase distribution, temperature profiles, defects density, etc. Electrical tomography techniques feature non-intrusiveness, high acquisition rates, and low cost. However, low frequency electrical currents are so-called soft fields, which generates complexity in the image reconstruction. Active research in medical and geological applications has provided interesting findings regarding the spatial resolution of electrical tomography images. The research on high frame rate measurements with electrical tomography is far more recent.

Thesis organisation

The main objective of this thesis is to assess the capability of electrical tomography for the high acquisition rate measurements of void fraction in high pressure high temperature two-phase flow experiments. The long-term target is to integrate this instrumentation in experiments at conditions representative of the primary and secondary circuits of nuclear pressurised water reactors of generations II and III. This introductory chapter explains the motivation for the work. An overview of the recent knowledge of electrical tomography has helped selecting Electrical Impedance Tomography for the research. The main challenge foreseen at the start of the Ph.D. was the non-linearity of the inverse problem of electrical tomography for high

contrast conductivity imaging. However, a solution to mitigate this issue was postulated: consecutive images in the sequence are relatively similar for high frame rate measurements so the previous image may be used as the *a priori* solution of the linearised inverse problem.

The plan of the thesis has been oriented as follows. This first introductory chapter described the background of tomographic imaging of multiphase flows. The second chapter describes the development of a prototype fast EIT sensor. The electrical potential of the excitation signal is controlled, providing interesting feature to the prototype sensor. In particular, the implementation of a module for voltage-to-current conversion is not necessary. A novel data collection method is proposed: the full scan strategy with 120 excitation patterns for a 16 electrodes sensor. The design of the system enables frame acquisition rates up to 833 frames per seconds with the full scan strategy. An overview of research and reports on existing EIT systems gives the motivation for the main technological features of the prototype. The hardware, software and procedures of the prototype are presented. Studies have been performed to assess the performance of the system and will also be reported. The third chapter explains the approach of flow regime identification using the raw measurement data. The principle is to recognise the flow regime and obtain associated parameters (*e.g.* cross-sectional void fraction) with a set of unprocessed data. The results might be considered as an approximate model of the flow, or as *a priori* information for the inverse problem. A brief introduction on the concept of flow regimes and an overview of state-of-the-art flow regime identification methods are presented. The work has been performed in the framework of a collaboration with Professor Saba Mylvaganam of University College of South-East Norway, before the prototype had been finalised. Details on the set-up of the flow facility and the Electrical Capacitance Tomography (ECT) sensor used in this study are given. The experimental campaign is described and the criteria developed for the flow regime recognition are shown. The flow regime provides an input for the image reconstruction method suggested in this thesis. The fourth chapter concerns the development of an image reconstruction algorithm. An extensive overview of the state-of-the-art in this field is presented. A method for image reconstruction has been developed within the framework of this thesis. It is based on the NOSER algorithm and a pseudo-2D postulate. The different steps of the method are presented and explained. Experiments has been performed in order to build a set of benchmark data presented in Appendix. The performance of image reconstruction is tested and comparison are made to highlight the role of some parameters. A concluding chapter summarises the findings and suggests some strategies for continuation of the project.

Notes and publications

An effort was put on the communication of the results of the Ph.D. research towards the scientific research community. At the 7th International Symposium on Process Tomography (Dresden, Germany, September 2015), preliminary results on piecewise-constant binary reconstruction of tomogram have been presented (Dupré et al., 2015). At the Specialists Workshop on Advanced Instrumentation and Measurement Techniques for Nuclear Reactor Thermal

Chapter 1. Introduction

Hydraulics (Livorno, Italy, June 2016), the features of the ProME-T prototype sensor and performance assessment studies have been reported (Dupré et al., 2016a). The content has also been published in the IEEE Sensors Journal (Dupré et al., 2017). At the 8th World Congress on Industrial Process Tomography (Foz do Iguacu, Brazil, September 2016), the results of the flow regime identification study with the ECT sensor has been shown (Dupré et al., 2016b). The content has also been accepted by the IEEE Sensors Journal and will be published in a special issue on Process Tomography (Dupre et al., 2017).

2 Prototype development

The basic principle of data collection in Electrical Impedance Tomography (EIT) consists in sequentially generating electrical excitations at selected pairs of electrodes and measuring the resulting voltage on all other electrodes distributed around the study volume. This chapter concerns the development of the prototype fast EIT system. The problem of processing the data to extract information or an image is left for the subsequent Chapters 3 and 4.

2.1 Overview of instrumentation for flow imaging

For a correct understanding of two-phase flows, it is important to develop instrumentation capable of measuring locally the void fraction and the phase velocities with adequate spatial and temporal resolutions. Development for instrumentation for high pressure high temperature flows is challenging. The next Section 2.1.2 gives a brief description of many imaging modalities that have been widely used in multiphase flow studies. Electrical tomography techniques are explained in more details in the subsequent Section 2.1.3.

2.1.1 Characteristic length and time scales of multiphase flows

The spatial and temporal resolution of an instrument for imaging a multiphase flow ideally should match its characteristic length and time scales. This is specific to a given application and experimental set-up. With increasing pressure, the size of the bubbles in gas-liquid dispersed flows shrinks and their velocity increases. The study of Nakath et al. (2013) illustrates the effect of pressure on the bubble-size distribution during fast pressure transient in nuclear pressurised water reactors in accidental scenarios. The results of this study are shown in Figure 2.1. Small bubbles of diameter in the order of the millimetre are encountered in this study of multiphase flows.

Amongst many other examples, the heat transfer downstream of the heating section is an important phenomenon to be understood in many energy systems. The experimental data for understanding heat transfer not only consists of the cross-sectional average phase fraction,

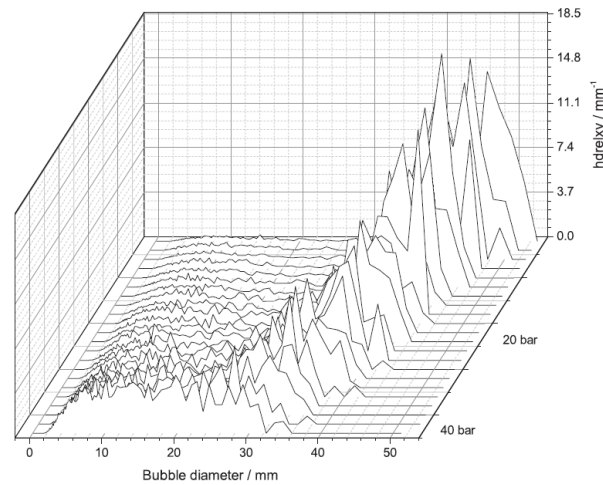
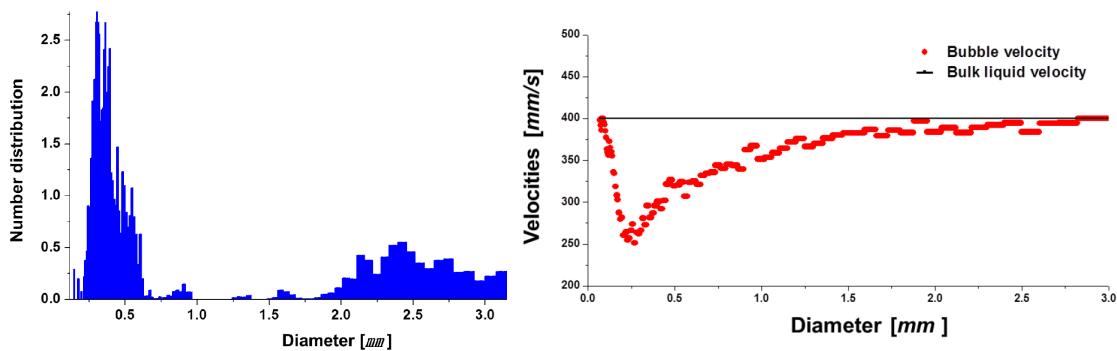


Figure 2.1: Bubble-size histogram in fast pressure transient experiment. Adapted from Nakath et al. (2013)

but also of the topology of the flow. Sub-cooled flow boiling for advanced compact heat exchangers has been analysed with a high-speed camera in Park (2013). Number distribution of bubble diameter and size-velocity diagram are shown in Figure 2.2. If the characteristic time scale of a bubble flow is taken as the minimum time for bubbles to move by their diameter, in Park's study it would be in the order of the millisecond (*e.g.* 0.002 s for the 0.5 mm diameter bubble group with velocity 250 mm · s⁻¹).



Number distribution of bubble diameter

Size-velocity diagram

Figure 2.2: Flow measurement downstream of heating section, $P=7.7$ bar, $G=300 \frac{kg}{m^2 \cdot s}$, $\Delta T_{sub} = 35^\circ C$, $q=7.64 \frac{kW}{m^2}$. Adapted from Park (2013)

2.1.2 Main imaging techniques

X-ray tomography is a widespread imaging technique that has emerged from medical applications. Electrons are accelerated from an anode to a cathode where the Bremsstrahlung effect

2.1. Overview of instrumentation for flow imaging

corresponding to the deceleration of electrical charges is responsible for the local emission of X-ray. The γ -ray tomography is a close relative that uses a radioactive material as a source of γ -rays. The attenuation of a collimated beam along a straight line (called ray sums) gives an information on the material composition along the path of the projection. A set of projections needs to be recorded in order to obtain information throughout the study volume. In the image reconstruction, also referred to as computed tomography (CT), mathematical operations such as the Radon transform are performed (Plaskowski et al., 1995). For a complete scan of all projections, both the source and the detectors had to be moved in systems of the first generation. In subsequent generations, detector panels and then source arrays were developed in order to speed up the acquisition. In ultra-fast X-ray tomography, an electron beam is directed to a metallic target thereby enabling fast scanning of all angular positions without any mechanical parts moving (see Figure 2.3). This state-of-the-art technique features a high spatial and temporal resolution in the order of 1 mm and 10000 frames per second (fps) respectively (Banowski et al., 2015; Hampel et al., 2016). While the imaging capabilities of X-ray and γ -ray tomography are outstanding, the safety measures associated with the use of ionising radiation and the operational costs are a burden. The reduction of the acquisition time comes at the expense of degraded spatial resolution, especially in the former generations of instruments. Finally, the high attenuation of the signal in metals associated with the dose limits are problematic for the use in metallic pipes and other complex geometries.

Magnetic Resonance Imaging (MRI) also originates from medical applications (Mansfield, 2003). In presence of a magnetic field, the magnetic moments of nucleus or electrons in the matter react in an identifiable manner to a sequence of radio-frequency pulses (see Figure 2.4). The study volume is scanned by controlling gradients of the magnetic field, thereby obtaining an image. The spatial resolution can be quite accurate when phases have similar magnetic susceptibility ensuring homogeneity of the applied magnetic field (≈ 1 mm resolution). The temporal resolution is dependent on the ratio between the field of view and the resolution limit. It ranges in the order of 100 ms for a 256×256 pixel image and 10 ms for a 64×64 pixel image (Mansfield, 2003). This imaging technique has been applied for analysis of oil-water flow (Lakshmana et al., 2015), and the proposed echo sequence took about 100 ms.

Ultrasound tomography scans a study domain via a pressure wave applied at multiple boundary source locations. The transmitted and reflected waves are characterised by an attenuation coefficient (frequency dependent) and a propagation time. The former is closely dependent on the void fraction in the sensitive volume while the latter yields valuable information on the topology of interfaces (Plaskowski et al., 1995). This measurement technique shows limitations for high void fraction content since a continuous incompressible phase is needed for the transmission of pressure wave. Furthermore, the propagation velocity in the domain puts a limit on the acquisition time of an image (in the order of 10-100 ms in the study of Opielinski and Gudra (2006)). Yet, the technique has been proven to be very successful for the precise measurements of micro-bubbles and ultra-low void fractions (Cavaro et al., 2013).

Wire-mesh sensor has been developed for multiphase flow monitoring applications (Prasser

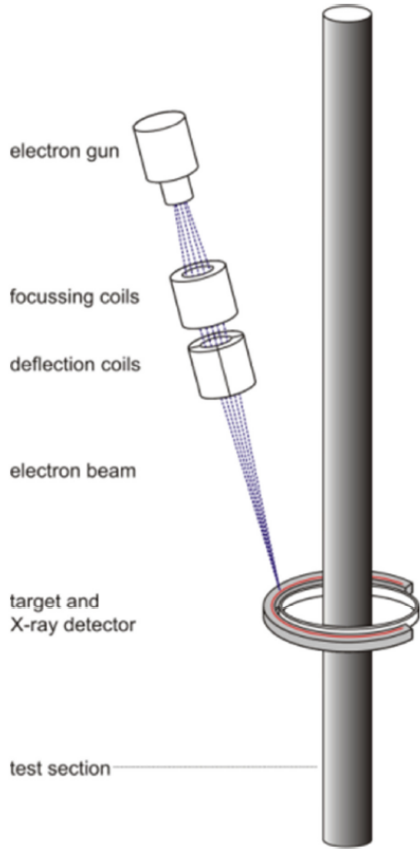


Figure 2.3: Principle of the ROFLEX sensor. Adapted from Hampel et al. (2016)

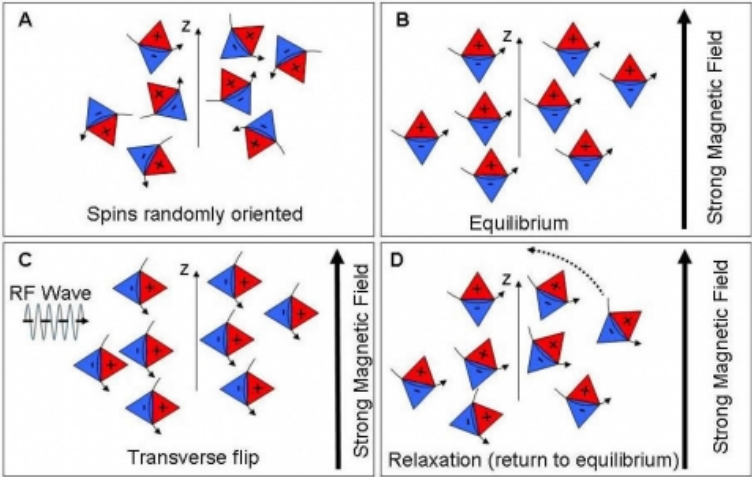


Figure 2.4: Typical echo sequence of MRI. Adapted from Joseph-Mathurin et al. (2010).

et al., 1998). A mesh of wire-electrodes covers the inner cross-section of a pipe. The sensor measures the capacitance between transmitter and receiver wire-electrodes, which can be related to the local volume-averaged void fraction within the sensitive volume around the

2.1. Overview of instrumentation for flow imaging

crossing of the two perpendicular wire-electrodes (see Figure 2.5). In order to capture an image, transmitters are activated sequentially using a multiplexing unit and the signals at the receivers are sampled simultaneously with parallel sample-and-hold circuits. The technique features a very high acquisition rate up to 10 kHz and an excellent resolution limit of the order of 3 mm (Banowski et al., 2015). Despite its intrusiveness, the design of the wire-mesh sensor has been improved and it has been used in the studies of harsh flows (Pietruske and Prasser, 2007). Also, interesting studies present the analytical method to determine interfacial area density from the gradient of void fraction which gives valuable insight on the heat transfer processes (Prasser et al., 2015). Yet, the integration in high pressure high temperature environments remains very challenging. Thicker wires need to be used to ensure sufficient robustness, so the intrusiveness of the sensor will be more pronounced. Higher vibrations of the wires mean the distance between the transmitters and the receivers needs to be increased, thereby requiring larger mesh and degraded spatial resolution.

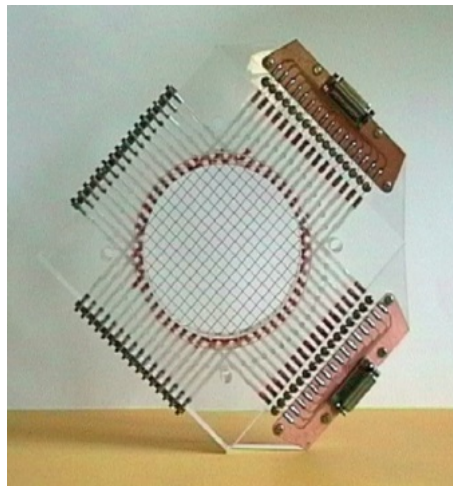


Figure 2.5: Wire-mesh sensor with orthogonal sets of transmitter and receiver wire-electrodes. Adapted from www.hzdr.de

2.1.3 Electrical tomography techniques

The key advantages of electrical tomography techniques are non-intrusiveness, high acquisition rates and cheap costs. An excellent overview of the instrumentation used in process tomography is given in Plaskowski et al. (1995), with a particular emphasis on electrical tomography. The principal categories of electrical tomography techniques are Electrical Impedance Tomography, Electrical Capacitance Tomography and Electromagnetic Tomography. As in any tomographic modality, the distribution of a parameter within a study volume is to be determined from a set of projections, *i.e.* measurements of the system response for a scan of excitations generated from the boundary of the test section. The Maxwell equations describe the electromagnetic behaviour in a given medium with known electrical properties. The major difference with radiation-based tomography techniques is that low-frequency electrical

currents are soft-fields: the sensitivity of a measurement is dependent on the distribution of materials in the study volume. Therefore, the concept of transmission paths or spatial resolution does not hold for soft-field tomography techniques though it can be approximated for a reference medium, as in Seagar and Bates (1985). The set of Maxwell equations and boundary conditions for all excitations used is referred to as the direct problem. Reciprocally, the distribution of electrical properties can be retrieved from a set of boundary excitations and measurements using reconstruction methods to solve the so-called Calderon's inverse problem (Calderón, 2006). In multiphase flow imaging, the distribution of phase (more specifically the local pixel-averaged void fraction) can be retrieved from the image of electrical properties via the Maxwell-Hewitt relation that assumes homogeneous mixing locally (George et al., 2000).

Electrical Impedance Tomography uses low frequency current excitations to probe the electrical conductivity and permittivity profiles of materials within a study volume. Electrodes are distributed around the test section. For each excitation pattern, a pair of electrodes is selected and connected to the current source and sink. The response of the system is measured either as the absolute voltages of electrodes or as the differential voltages between neighbouring electrodes. Electrodes are directly in contact with the conductive continuous phase within the study volume in order to ensure that the electrical conduction of the current is the prevailing electromagnetic phenomenon. In studies considering water as the continuous phase, it is frequent to consider the addition of electrolytes and select excitation frequencies in the range 10-100 kHz (George et al., 2000; Wang, 2005).

Electrical Capacitance Tomography uses high frequency voltage excitation to probe the electrical permittivity of materials within a study volume. Electrodes are mounted on the outer surface of the pipe, not in direct electrical conductive contact with the study volume. ECT systems are non-intrusive and non-invasive. A high amplitude high frequency electrical potential is set at one electrode while the resulting charges on the other electrodes (kept at ground potential) are measured and capacitance between each pair of electrodes computed. The procedure is repeated until all electrodes have acted as source once (Huang et al., 1988). Since the ECT signals are extremely weak, a considerable effort on pre-amplification and signal conditioning is crucial. Furthermore, a reasonable sensitivity can only be achieved with large surface electrodes (Ahmed and Ismail, 2008), which puts a limit on the spatial resolutions achievable with this modality. The prevalence of the displacement current means that there are no requirement on the conductivity of the materials to be imaged. As a result, this technique is appealing for studies on chemical bed reactors and gas-particle flows. Electrodes being mounted on the outer diameter of the pipe/vessel, a dielectric material needs to be selected. Therefore, ECT is not suitable for high pressure high temperature applications that requires a metallic pipe to withstand the mechanical and thermal loads.

Electromagnetic Tomography stimulates the study volume using a set of magnetic fields generated by coils distributed around the test section. The induce voltages at the non-activated coils are recorded, and they are impacted by the generation of eddy currents within the

2.1. Overview of instrumentation for flow imaging

sensitive volume. As a result, the signal is related to the electrical conductivity and/or the magnetic permeability of the materials (Terzija et al., 2011).

The main instrumentation techniques for imaging of multiphase flows present limitations at high pressure and temperature. In harsh flow imaging applications, the pipes or the vessel are inevitably made of metal which prevents the use of non-invasive arrays of ECT electrodes. The spatial resolution of EIT is better and its implementation easier.

2.2 Overview of electrical impedance tomography

This section is an introduction to the the electromagnetic theory and basic principles of data collection for EIT. An overview of reported fast EIT sensors, recent trends and findings is proposed so the reader will have a clear idea of the state-of-the-art for this active research field.

2.2.1 Electromagnetism and forward problem

Electromagnetism

Electrodynamics is the branch of physics relating electrical charges and currents. Maxwell equations describe electromagnetic phenomena up to the length scale and field strengths where quantum electrodynamics applies:

$$\vec{\nabla} \cdot \vec{D} = \rho_v, \quad (2.1)$$

$$\vec{\nabla} \cdot \vec{B} = 0, \quad (2.2)$$

$$\vec{\nabla} \times \vec{E} = -\frac{\partial}{\partial t} \vec{B}, \quad (2.3)$$

$$\vec{\nabla} \times \vec{H} = \vec{J} + \frac{\partial}{\partial t} \vec{D}. \quad (2.4)$$

with \vec{B} the magnetic induction field, \vec{H} the magnetic H-field, \vec{J} the electrical current, \vec{D} the electrical displacement, \vec{E} the electrical field and ρ_v the electrical charge density.

The constitutive equations (*i.e.* its electrical properties of materials) relate the electrical current \vec{J} and displacement \vec{D} to the electrical field \vec{E} :

$$\vec{J} = \sigma \vec{E}, \quad (2.5)$$

$$\vec{D} = \epsilon \vec{E}, \quad (2.6)$$

where σ and ϵ are the electrical conductivity and permittivity of a given material.

Considering the divergence of (2.4) and using the constitutive equations (2.5) and (2.6) results in:

$$\begin{aligned} \vec{\nabla} \cdot \left(\sigma \vec{E} + \epsilon \frac{\partial}{\partial t} \vec{E} \right) &= \vec{\nabla} \cdot (\vec{\nabla} \times \vec{H}) \\ &= 0. \end{aligned} \quad (2.7)$$

Electrical tomography techniques (EIT and ECT) are applications in which fluctuating magnetic fields play a negligible role in comparison with electrical current and/or displacement. As a result, one can notice in Equation (2.3) that the electrical field \vec{E} is conservative since $\vec{\nabla} \times \vec{E} = \vec{0}$ and its scalar potential V , the electrical potential can be defined: $\vec{E} = -\vec{\nabla}V$. Also,

2.2. Overview of electrical impedance tomography

Equation (2.7) can be recast in the frequency domain with a phasor transformation: $\frac{\partial}{\partial t} \vec{E} = i\omega \vec{E}$, with i the unit imaginary number and ω the angular frequency and results in the following formulation for the forward problem within the study volume Ω :

$$\vec{\nabla} \cdot (\gamma \vec{\nabla} V) = 0, x \in \Omega, \quad (2.8)$$

with $\gamma = \sigma + i\omega\epsilon$ the electrical complex conductivity. For the sake of clarity in equations, we use shorthand notation for V , γ , σ and ϵ though, as scalar fields, they are functions of $x \in \Omega$.

Bates (1984) gives a generalised theory of full-wave problems. Low-frequency electrical current belong to the simplified category of conservative fields (like stationary magnetic fields and streamlined fluid flow) (Seagar and Bates, 1985).

Tomography

In electrical tomography, electrical currents J are sourced or drained onto the periphery of the study volume $\partial\Omega$. The *continuum* model of electrodes (Cheney et al., 1990) gives the following boundary condition:

$$-\sigma \frac{\partial V}{\partial \nu} = J, x \in \partial\Omega, \quad (2.9)$$

with ν the outward unit normal to the boundary.

There are other approaches to model the electrodes with various degrees of approximation of the real physics. In the *gap* model, a current I_l is set at each electrode (E_l , $l=1,2,\dots,L$) and the current density is assumed to be constant throughout the electrode-electrolyte contact area A_l , as in equation (2.10) (Cheney et al., 1990). The *shunt* model adds the influence of the highly conducting electrode contact area on the electromagnetic behaviour near the electrodes. The complete electrode model is the compilation of the *continuum* model with the description of the shunt effect and of the contact impedance phenomenon (Hanke et al., 2011).

$$\sigma \frac{\partial V}{\partial \nu} = \begin{cases} \frac{I_l}{A_l} & \text{for } x \in E_l, l = 1, 2, \dots, L \\ 0 & \text{for } x \notin \bigcup_{i=1}^L E_i \end{cases}. \quad (2.10)$$

The materials within the study volume do not store electrical charges, as a result all currents flowing into the test section are necessarily flowing out:

$$\int_{x \in \partial\Omega} J dx = 0. \quad (2.11)$$

The reference electrical potential may be chosen arbitrarily as:

$$\int_{x \in \partial\Omega} V dx = 0. \quad (2.12)$$

The set of Equations (2.8), (2.9), (2.11) and (2.12) replicated for every excitation patterns considered in the data collection strategy is frequently referred to as *forward* or *direct* problem in the literature (Tanushev and Vese, 2007).

It can be solved numerically with the methods of finite elements (George et al., 2000), finite volumes (Tanushev and Vese, 2007) or boundary elements (Peytraud, 1995). Approximations or simplifications can be used to reduce the computational cost, in particular in simple geometric setups such as cylindrical study volumes (Kotre, 1988; Nissinen et al., 2013). A few special cases have known analytical solutions (Pidcock et al., 1995; Torczynski et al., 1996; Seagar and Bates, 1985).

An open-source free software has been developed within the framework of the Electrical Impedance Tomography and Diffuse Optical Tomography Reconstruction Software (EIDORS) project (Polydorides, 2002). A flexible set of Matlab routines is provided for solving the forward and inverse problems of electrical tomography. The meshing can be provided by Netgen. Many examples are available. The software is very popular within the electrical tomography community and has been used in this thesis.

2.2.2 Basic principle of data collection for EIT

In practice, a finite set of electrodes (typically 16 or 32 in EIT, 8 or 12 in ECT) is available for the generation and the acquisition of electrical signals. Generally, in research or industrial applications, a simplistic 2D or 3D cylindrical study volume is being considered and the electrodes are arranged as a ring (regularly spaced in one cross-sectional plane). In typical procedures for EIT, a current is generated with a Voltage Controlled Current Source (VCCS) and the source and drain ports are connected to the current injection electrodes. Multiplexers (MUXs) "*usually implemented using solid state switches*" control the selection of the current injection electrodes (York, 2001). In parallel, the resulting voltage are measured synchronously on all available electrodes. Some set-ups consider the measurement of differential voltages between neighbouring electrodes, while others measure the absolute electrode potentials with respect to a common ground reference. The former is an efficient method to suppress common-mode parasitic noises, while the latter can suffer from potential biases in the common ground. In this thesis, the set of measurements for all excitation pattern considered is referred to as a frame.

There are a variety of reported data collection strategies, including the adjacent method that remains the most employed method to date (Wang et al., 2005). This is a crucial feature because it has implications for the number of data (per frame) to be acquired and processed,

2.2. Overview of electrical impedance tomography

and also impacts the sensitivity of the sensor. Kauppinen et al. (2006) presents an overview of adjacent, opposite, cross and adaptive strategies and assess the sensitivity and selectivity of measurements for 2D and 3D standard cylindrical geometries. Sensitivity is the scalar product of the current injection and voltage measurement lead fields. Selectivity is the sensitivity in the target region relative to the total sensitivity. Irrespectively of the method employed, switching the current injection and voltage measurements pairs of electrodes results in an equivalent measurement that can be discarded (*i.e.* half of measurements).

- The adjacent (also called neighbouring) data collection strategy considers pairs of adjacent electrodes for the current injection (and often also for the voltage measurements). The measurements concerning 1 or 2 current-injection electrodes are discarded because they are potentially biased by the voltage drop within the electrodes. As a result, there are $\frac{16 \times 13}{2} = 104$ linearly independent measurements in a frame of a 16-electrodes sensor. The strategy yield a good sensitivity in the regions near the electrodes, but is almost insensitive to the centre of the study volume.
- The opposite strategy employs pairs of opposite electrodes for current injection. It yields an optimal sensitivity and selectivity at the centre of the study volume, and requires only 8 excitation patterns for an equivalent amount of linearly independent measurements.
- The cross (also called diagonal) method skips one in two electrodes for the current injection and yield $14 \times 13 = 182$ measurements per frame.
- The adaptive strategy enables simultaneous current flow from all the electrodes according to an optimised current pattern maximising the resulted voltage measurements for desired regions. The experimental set-up is obviously far more complex. *"For most applications this advantage of multiple-electrode excitation may not justify the price that must be paid in terms of higher system complexity"* (Gamio, 2002).

In Figure 2.6, the most sensitive configurations to detect centre region of the model for the standard data collection strategies are shown. The reader can notice the zone of negative sensitivity delimited with the black line (particularly wide for the adjacent strategy). This means that the presence of an inclusion in these regions would lower the voltage measurement as compared to the reference homogeneous medium.

The pairs of electrodes selected for the adjacent, opposite and cross methods are shown in Figure 2.7.

In EIT (unlike ECT), the electrodes are in direct contact with the materials inside the study volume. The instrumentation is therefore invasive (yet non-intrusive), but the surface area of the interface between the electrodes and the study volume can be kept very small. If there is a continuous conducting phase and the frequency of the electrical excitation signal is relatively low, there is a dominant contribution of the electrical conductivity (since $\gamma = \sigma + i\omega\epsilon$). Frequently, researchers control the conductivity of the liquid solutions by addition

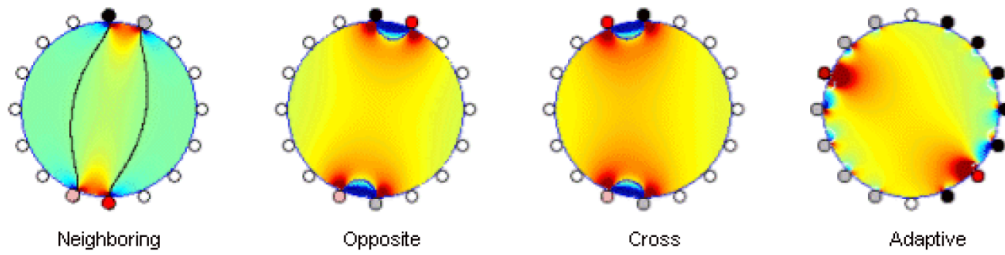


Figure 2.6: Most sensitive configurations to detect centre region of the model for neighbouring, opposite, cross and adaptive strategies. The black lines indicate the delimitation between zones of positive and negative sensitivity. Adapted from Kauppinen et al. (2006)

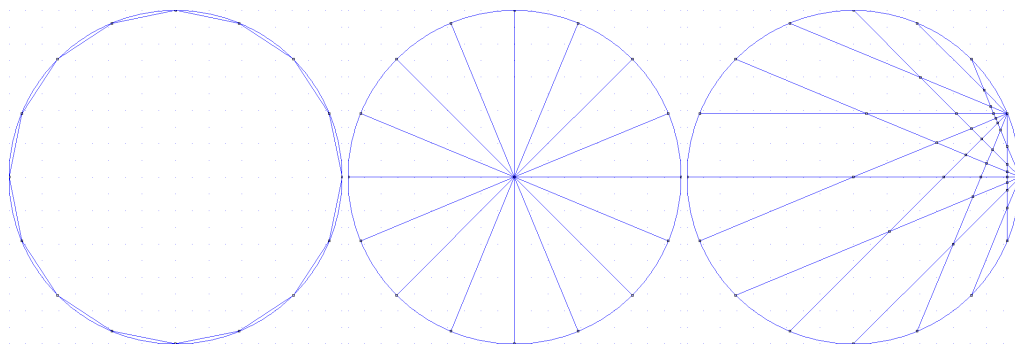


Figure 2.7: Illustrations of adjacent (left), opposite (middle) and cross (right) data collection strategies

of electrolytes and the excitation frequency in order to minimise the capacitive effects (George et al., 2000).

Though the geometry of the study volumes can be very complex (in particular in medical research), numerous research works consider simplistic geometries (*e.g.* 2D disks or 3D cylinders). In order to consider a 2D forward and inverse problems with 3D cylinders, it is frequent to use axially elongated electrodes with an axial extent of many cross-section diameters (Peytraud, 1995). Yet, the buckling of the electrical field lines at the extremities create a bias with the 2D models. However, electrode guards can be employed to contain, at a certain extent, the electrical field lines in a plane (Ma et al., 1999). This result is valid for a homogeneous medium. Guards electrodes at the two extremities of the sensing electrodes are kept at same potential with a guards driving unit (composed of a low input offset high input impedance and a high precision voltage follower operational amplifiers). In addition with a better approximation of the 2D forward problem, guard electrodes "*compress the distribution of the sensing field*" providing a better sensitivity. The need for electromagnetic field lines contained in two-dimensions for computing the forward problem in 2D has become obsolete with the increased capabilities of modern computers. Often, the electrodes are arranged around the cylinder at regular angular separation, and are referred to as *electrode ring*. In multiphase flow studies, two electrode rings or more may be placed on different planes

(separated by one or more diameters of the test section) in order to obtain information on the velocity using cross-correlation techniques (Wang et al., 2005). Given the axial separation H of the planes, the cross-correlation function of the two signals is maximum for the transit time τ of a coherent feature (*e.g.* a bubble) and the axial velocity of the disperse phase can be inferred: $v_z = \frac{H}{\tau}$ (Plaskowski et al., 1995).

2.2.3 Towards high frame acquisition rates

In multiphase flow studies, time-resolved imaging provides extremely valuable information. Depending on the specific applications, the flow characteristic time at a resolved spatial scale can be less than the millisecond, as was illustrated in Section 2.1.1. Developing fast EIT systems and procedures with an adequate frame acquisition rate is a real challenge, despite the technological leap in electronics. Since the 2000s, parallel sampling of all measurement channels has been the main driver of the improvements in frame rates. Many teams have focused on the development of fast EIT systems with different approaches.

A high performance EIT system at Leeds University has been reported in Wang et al. (2005). The excitation signal is an AC sinusoidal current waveform. The breakthrough in frame acquisition rate is explained by the parallel acquisition of voltage measurements on all 16 channels and by the novel *over-zero-switching* (OZS) scheme implemented to limit the transient effects caused by residual potentials arising after multiplexers switch. The adjacent data collection strategy (16 excitation patterns) is used, and data acquisition rates up to 1164 fps have been achieved. The management of the data transfer is also a complex task. Last but not least, the distinction must be made between systems for online or offline image reconstruction. The online implementation requires more efforts on the computing modules and reconstruction algorithms. With a sine-wave excitation signal, at least a full-period need to be captured, with at least 4 samples per excitation pattern for reconstruction of the complex impedance. When the multiplexer is operated to switch the current to different source and drain electrodes, the residual potential at the previous source electrode decays with an AC coupling time constant. This parasitic effect is caused by the contact impedance at the electrode-electrolyte interface, and has can be modelled (Wang and Ma, 2006; Pollak, 1974). In the past systems, the system would wait the parasitic to have faded before starting the sampling or the process would be accelerated "*by either the use of a direct coupling, a higher order filter or a clamping and discharging circuit*" (Wang et al., 2005). The researchers at Leeds University came up with the OZS scheme that consists in controlling the operation of the multiplexers at the peak value of the current, thereby limiting the amplitude of this transient potential (but not its decay time).

The 1000-measurement frames per second EIT system at Cape Town University has been reported in Wilkinson et al. (2005). A switched DC current pulse technique is used to generate the excitation signal. The differential measurements between positive and negative half-cycles effectively cancel out the transient potentials resulting from double-layer capacitance and solution interface (Wilkinson et al., 2005). This system also implements parallel data sampling

Chapter 2. Prototype development

of all measurement channels. The diagonal data collection strategy is implemented, with 14 excitation patterns per frame. A sustained rate of 1000 frames per second is reported.

The EVT4 ECT system at Warsaw University has been reported lately in Smolik et al. (2016a) and Smolik et al. (2016b). For completeness, we mention this Electrical Capacitance Tomograph under development. The design is claimed to provide 10000 fps (but it has only been demonstrated in practical tests at 30 fps for a 16 electrodes sensor). The technological challenges and applications are very different for fast ECT systems, but higher frame rates can be achieved because the excitation signal frequency is not restricted to the resistive domain.

The forward problem of electrical tomography relates the distributions of electrical potential and current on the boundary of the study volume. EIT consists in applying a set of excitation patterns from selected boundary electrodes and simultaneously measuring electrical potentials resulting on the electrodes. The fast operation of the EIT system raises several challenges.

2.3 Hardware

A prototype sensor (named *ProME-T*, standing for "*Prototype pour Mesures Electriques par Tomographie*" in French) for fast EIT measurements of multiphase flows has been developed within the framework of this Ph.D. thesis at the Laboratory of Hydromechanics of Core and Circuits of CEA Cadarache. Its design was conceived for a maximal frame acquisition rate of 833 fps, considering the most complete data collection method (referred to as *full scan strategy*). This section unveils details on the test section, the electrodes, the equipment for signal generation and data acquisition and the multiplexing of the excitation signal.

2.3.1 Test section

At this proof-of-principle stage of the development of ProME-T, the experimental conditions have been kept as simple as possible: measurements of acrylic rods (electrically insulating inclusions) immersed in a cylindrical tank made of Polymethyl methacrylate (PMMA) and filled with tap water, at ambient temperature and pressure. Yet, provided the acquisition rate in these simplistic experiments adequately matches characteristic time scales of real flows, the outcome will be similar to dynamic two-phase flows experiments. It was verified that there are scratch resistant ceramic coatings and able to withstand up to 482 °C in continuous operations that could provide insulation to a standard steel pipe used in industry. Water tightness of openings for electrodes is not an issue since existing solutions already exists (*e.g.* for differential pressure measurements). The tests in the simple test section are equivalent in terms of electrical behaviour to those in a metallic test section with insulating coating for high pressure high temperature flows.

A picture of the ProME-T prototype, the computer aided design (CAD) model of the test section and its side view are shown in figures 2.8, 2.9 and 2.10. It comprises a single plane 16 electrodes holding ring sandwiched between two cylindrical extensions and taps. A specificity of the sensor is the small axial extent of the ring of electrodes (5 mm). Forward calculations for the homogeneous medium have indicated that the sensitive volume of the sensor is restricted axially. The inner and outer diameters of the cylindrical test section are respectively 100 and 110 mm. An internal overpressure up to 2 bars can be withstood. The height of the cylindrical study volume is 190 mm, *i.e.* approximately two internal diameters. Existing EIT systems consider the internal diameter of the pipe as an appropriate separation distance between two consecutive rings of electrode (Schlaberg et al., 2008). This reference, together with numerical perturbation studies, brings confidence in the selection of the height of extensions in ProME-T.

Alternatively, the user can also approach planar electromagnetic fields simply by removing the extensions. The set-ups with and without the extensions are referred to as *2D configuration* and *3D configuration* respectively. Finally, the test section could be incorporated in a two-phase flow loop without using taps. An in-house developed system has been designed for the positioning of the plastic cylinders mimicking the insulating phase of two-phase gas-liquid flows (see figure 2.11). A breadboard for through hole components arranged in a matrix of

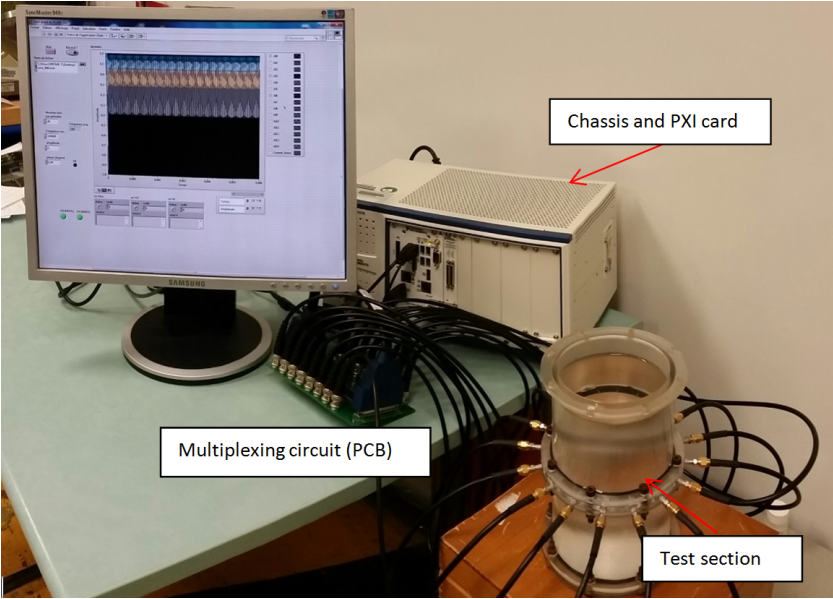


Figure 2.8: Picture of the ProME-T prototype sensor

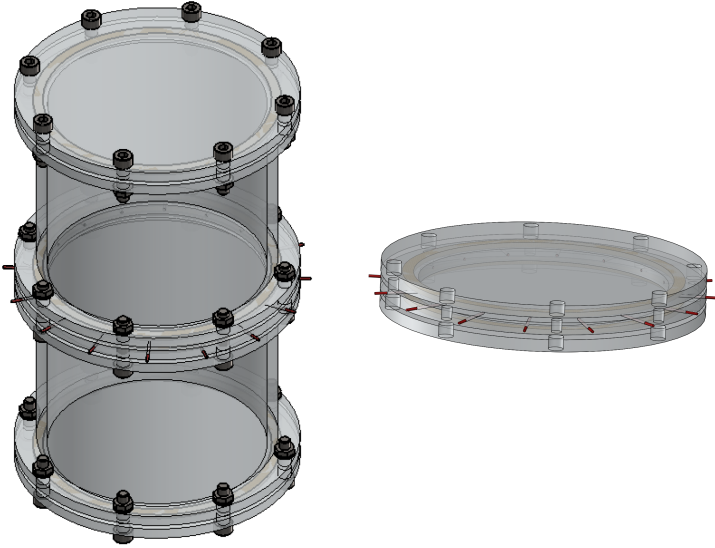


Figure 2.9: CAD models of the test section in 3D configuration (left) and 2D configuration (right)

2.54 mm pitch is fixed at the top of the test section. It is used to support pinheads of the needles inserted through holes, which are pressed into the cylinders. Thereby, the cylinders are hanging, which ensures they are vertical in the test section. The precision is estimated to be roughly in the order of the millimeter, *i.e.* a hundredth of the test section diameter.

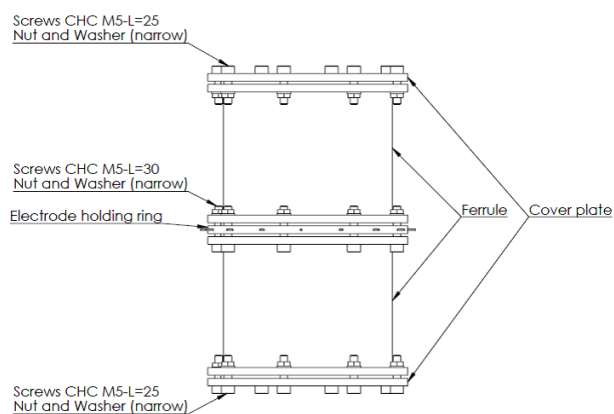


Figure 2.10: Side view of the test section

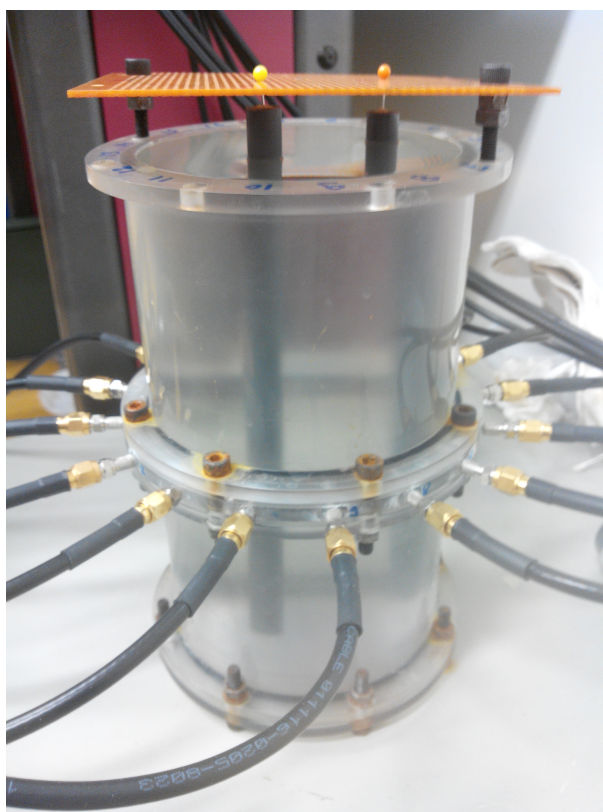


Figure 2.11: System for positioning of rods

2.3.2 Electrodes

Point-like electrodes

Electrodes are platinum rods of diameter 1 mm with angular separation of 22.5° (*i.e.* 20 mm). The electrode-electrolyte contact surface is a circular area measuring only 1 mm in diameter. As a result, the gap model (Cheney et al., 1990) of electrodes can be used reliably in

Chapter 2. Prototype development

the forward problem: one can assume the voltage (hence the current density) is uniform on the electrode-electrolyte contact surface. Given the small extent of the electrode-electrolyte contact surface with respect to the inter-electrode separation, we refer to this design as *point-like* electrodes (not to be confused with mathematical definitions of point). The small dimensions of electrodes has a lot of implications in the project beyond the perspective of fitting more electrodes in the ring. In particular, in the *3D configuration*, the impedance for any selected pair of current injection electrodes is almost constant. Numerical simulations of the forward problem for a homogeneous cylindrical volume with different heights is shown in Figure 2.12. The measurements in the 2D configuration of the test section present a symmetry expected from the uniform repartition of the electrodes around the holding ring (see results indicated in green). Alternatively, the variance of the set of impedances of the measurements in the 3D configuration of the test section gets close to zero with increasing height of the test section (see results indicated in blue). This has been first observed experimentally, and the study will be discussed in subsequent Section 2.6.3 and results shown in Figures 2.33 and 2.34 on page n°51. This finding further supports the choice of point-like electrodes because it provides an optimal setting of the measurement range for the current sense channel (irrespective of the excitation pattern). More importantly, assuming a fixed voltage difference between the pair of current injection electrodes, the resulting current is ensured to stay below a maximum threshold and not exceed the capabilities of the source (5 mA for the hardware of ProME-T).

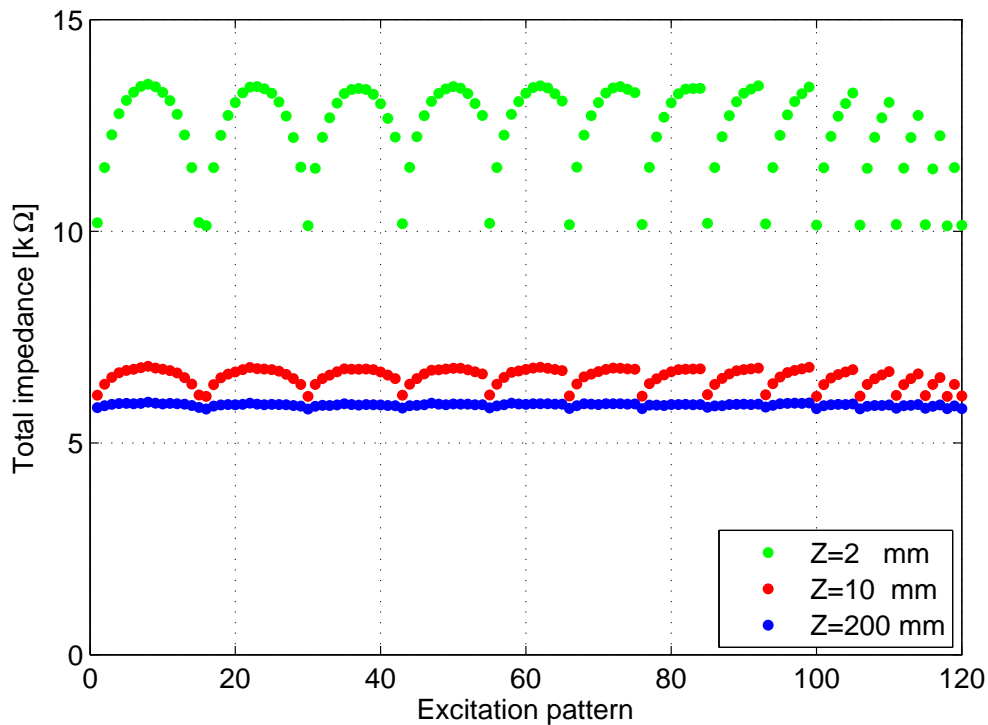


Figure 2.12: Simulation of total impedance for each of 120 excitation patterns, for different heights of the test section: $Z=2, 10, 200$ mm

Chapter 2. Prototype development

absence of significant bias caused by geometric errors, and *electrode-specific* impedances should be included in the boundary condition of the model of EIT in Equation (2.9). This will be discussed in a subsequent Section 2.6.3. A new test section with different design and better tolerances on electrodes alignment is currently being manufactured. It is mentioned in subsequent Section 3.5.4.

In the frame of this thesis, guard electrodes have not been considered because it brings complexity in the design. Solving the forward problem in 3D has been accomplished without difficulty.

2.3.3 Signal generation and data acquisition

In ProME-T, the data acquisition and generation of the excitation signal is managed by the National Instruments PXI card PXIe-6368. A schematic representation of the set-up is shown in Figure 2.14.

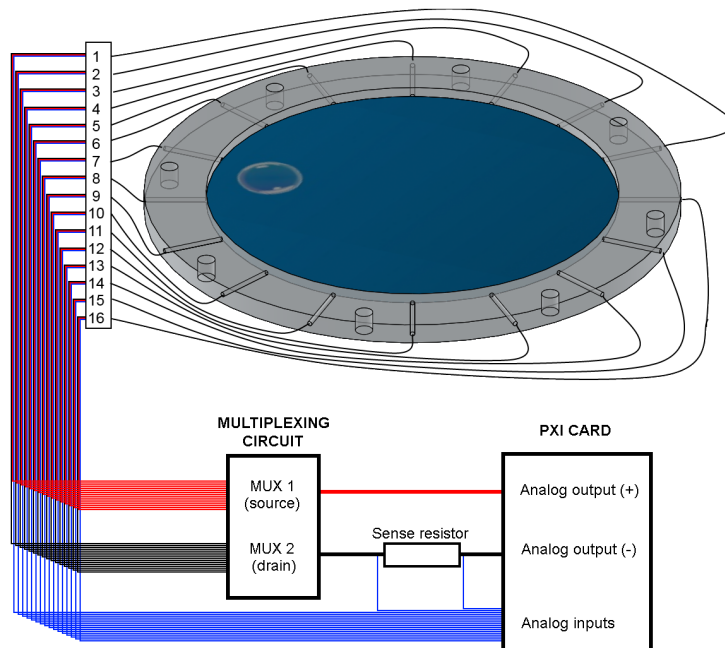


Figure 2.14: Outline schematic of the ProME-T hardware - test section, multiplexing circuit and PXI card with the coupling leads to the test section with electrodes

It has 16 analogue differential input channels that may be simultaneously sampled up to a frequency of 2 MHz, and 4 analogue differential output channels sampled up to 3.33 MHz. The resolution of all digital-to-analogue converters is 16 bits. In other words, the relative error they introduce is in the order of $1.10^{-3}\%$ for full scale signals. Concerning the generation of the

excitation signal, a differential voltage is set on one differential output channel, and the source and drain ports are each connected to a multiplexer responsible of routing the excitation to the target electrodes. Two other channels are employed for powering the multiplexers. The amplitude of the AC voltage is set at 1 Volt (peak-to-peak) in order to stay below the standard potential of the water electrolysis reaction (1.23 V). Frequencies up to 100 kHz have been considered in ProME-T. Concerning the data acquisition, 15 channels are dedicated to the differential voltage measurements at pairs of neighbouring electrodes and the remaining channel is used to measure the electrical potential across a 200 Ω sense resistor. The current flow in the test section and the electrical potentials of each 16 electrodes can be derived from these measurements. The advantage of acquiring differential voltage between neighbouring electrodes instead of the ground referenced measurements relies in the fact that the common mode noise is rejected and there is no risk of bias originating from so-called ground currents.

The data acquisition, the generation of the excitation signal and the control of the multiplexers need to be synchronised. The details are left for the next Section 2.3.4, but the reader can note that the same sampling rates have always been considered for the analogue input and output (for the sake of simplicity in the post-processing of data).

The objective of the ProME-T prototype sensor is to assess the capabilities of EIT for high frame rate measurements. Because of the increase of capacitive and inductive effects at high excitation frequencies of the excitation signal, a maximum 100 kHz frequency is considered. Numerous researchers also considered excitation frequencies in the range [50 – 100 kHz] (Wang et al., 2005; George et al., 2000). An originality of the project lies in a more complete method for data collection, called *full scan strategy*, which consists in setting 120 different patterns of excitation for each frame. The detailed explanation of this method is left for a subsequent Section 2.4.2. As far as the hardware is concerned, the electrical data for a frame can be obtained in 1.2 ms in the fastest acquisition mode of ProME-T (assuming a single period of the excitation signal for each of the 120 patterns). Given the examples of typical flow the research community is interested in, a frame acquisition rate of 833 fps is an appealing target.

The PXIe-6368 card is managed by a National Instruments controller unit PXIe-8840 housed in a PXIe-1078 chassis. This hardware has a maximum system bandwidth of 1.75 Go/s which is sufficient to handle the continuous transfer of the data at a sustained rate of 64 MB/s (corresponding to all 16 channels sampled at maximum acquisition rate of 2 MHz). The chassis has 3 slots for PXIe cards, which allows for future upgrades of ProME-T with multiple arrays of electrodes.

2.3.4 Multiplexing

The drain and source ports of the differential analogue output dedicated to the generation of the excitation signal are each connected to an Analog Device ADG406 multiplexer routing the ports to the target electrodes. Each target among the 16 electrodes is selected via a 4-bit

Chapter 2. Prototype development

binary address sent via digital outputs also available on the same PXI card, at a rate up to 10 MHz. The typical and maximum transition times are respectively 120 ns and 150 ns, which allows switching in between two acquisitions at the maximum acquisition frequency without impacting the measurement. The channel-to-channel crosstalk of the ADG406 is very low (85 dB).

A dedicated printed circuit board (PCB) has been designed and built. A 3D CAD model is shown in Figure 2.15. It integrates the two multiplexers in PDIP packaging, a precision sense resistor, 16 SMA connectors for the connection to the electrodes and two 68-pins D-type connectors for the connection to the PXI system. Selecting a sense resistor of 200 Ω ensures that the maximum current the analogue output can source (5 mA) cannot be exceeded for a 1 V excitation, no matter what the resistance within the test section is. The TE Connectivity H8200RBYA product has been selected because of its excellent resistance tolerance $\pm 0.1\%$ and temperature coefficient $\pm 15\text{ppm}/^\circ\text{C}$. The PCB was designed with the DesignSpark PCB software. Only through-hole components have been selected and have been soldered at the laboratory. Given the complexity of the system, the need to separate digital and analog tracks and the fabrication costs of multi-layered boards, the final version of the board has 4 layers. The detailed schematic and integration views are shown in Figures 2.16 and 2.17. A metallic case for housing and shielding the PCB is currently being designed.

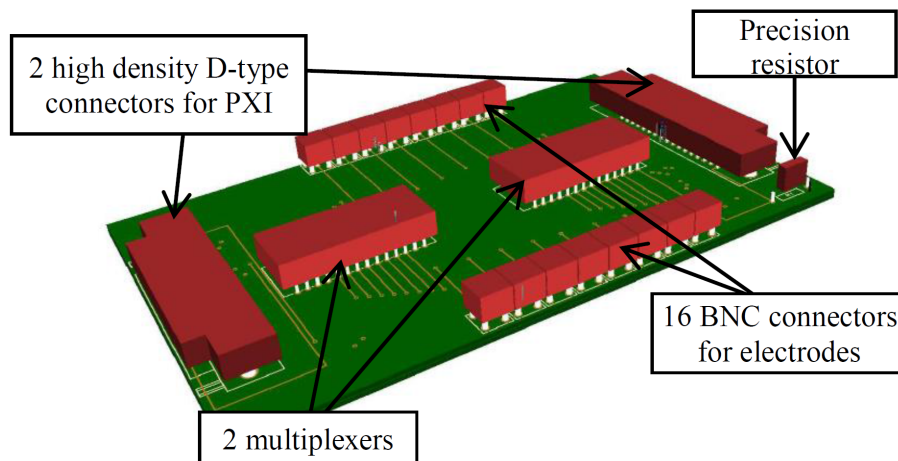


Figure 2.15: 3D CAD model of the PCB board used in multiplexing

The current version of the ProME-T prototype sensor considers a cylindrical test section with an array of 16 point-like electrodes. The hardware architecture of the ProME-T prototype EIT system comprises a module for signal generation and data acquisition and a module for multiplexing.

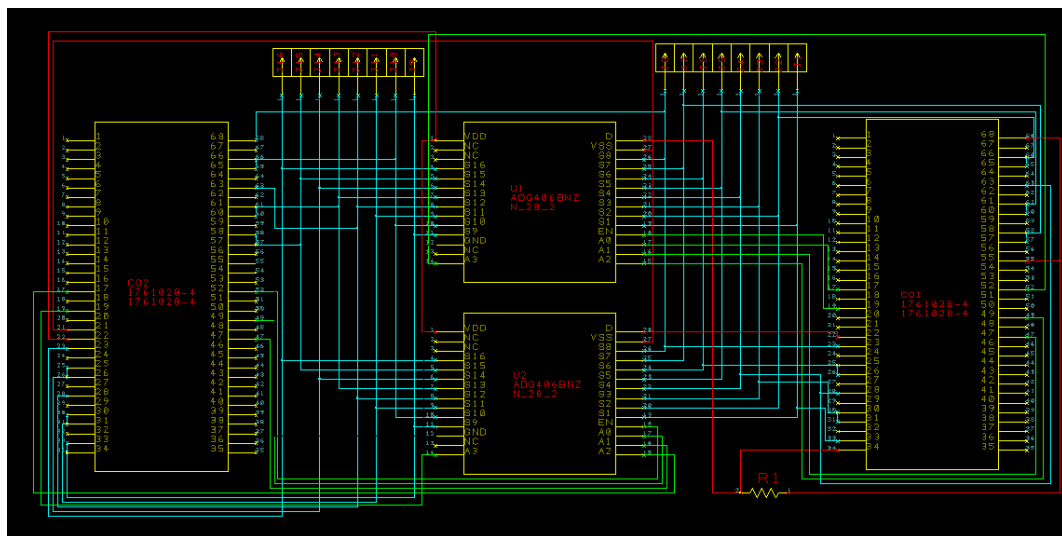


Figure 2.16: Wiring details (schematic) of the PCB board used in multiplexing

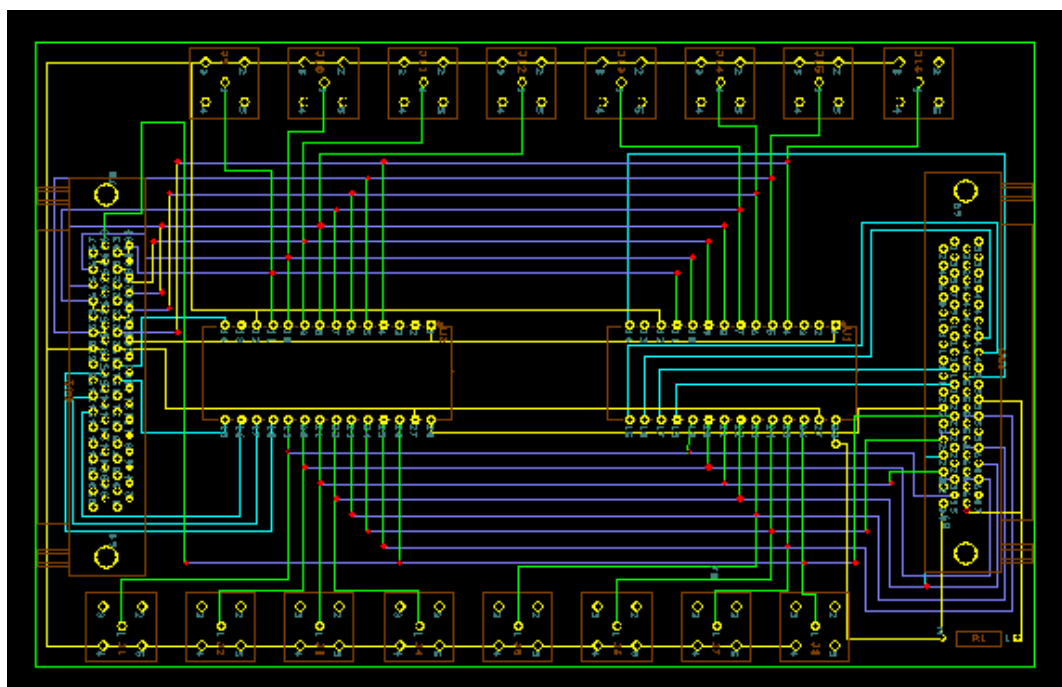


Figure 2.17: Wiring details (integration) of the PCB board used in multiplexing

2.4 Software and procedures

As a consequence of the architecture of the system and the novel data collection strategy, the software and procedures for post-processing the data of ProME-T are original. This section covers the features of the excitation signal, the strategy for data collection, the digital signal processing. A comprehensive and complete description of the procedure for fast EIT is given.

2.4.1 Excitation signal

In many EIT systems, a Voltage Controlled Current Source (VCCS) is employed to control the intensity of the current injected into the test section. Cascade of special operational amplifiers have been used to convert a balanced voltage source into a constant current source (Wang et al., 2005). Typically, the resulting circuit is characterised by an output impedance, *i.e.* a constant current will be sourced only if the load at the output terminal is less than a certain threshold. It means the system will be designed for a limited void fraction. In ProME-T, many reasons have led to the choice of voltage excitation. It is extremely simple to insert a sense resistor in the system in order to measure the current that is injected inside the test section. Regardless of the impedance of the medium within the study volume, the value of the current is known for the obvious reason it is measured. The maximum voltage being set at the current injection electrodes, one can be sure the water electrolysis reaction does not occur. Moreover, the voltage measurement range can be set optimally at the value of the simulation signal. Last but not least, the electronic circuit is simplified and no additional external power supply is needed, which is a simplification regarding the electrical safety procedure also.

Concerning the risk of water electrolysis, gas bubbles forming at the current injection electrodes at DC voltages exceeding 3 Volts have been observed in preliminary experiments. A measure of the pH potentially indicated the formation of NaOH. It is clear that this phenomenon absolutely needs to be prevented by all means. There are doubts whether the reaction can take place unnoticed at lower voltages and/or higher AC frequencies. As a result, it has been decided to carry on with voltage control of the electrical excitation and limit the amplitude to 1 V, *i.e.* below the standard potential of the reaction (1.23 V). Setting the amplitude of the excitation at 1 V also let the gain selection of the measurement channels be adjusted to the [-1 V, 1 V] window. Thereby, there is no need to set up an on-the-fly gain adjustment for adjusting to all signals. The author acknowledge that the research on the influence of AC frequency on water electrolysis has been considered out of the scope of the Ph.D. thesis, and that eventually the electrical potential could be safely increased beyond the prescribed 1 V limit after careful investigation of electrolysis (Senftle et al., 2010).

2.4.2 Data collection strategy

Due to the extremely high sampling rate of the hardware selected in ProME-T, it has been postulated that more measurements than standard data collection strategies could be made

available at a frame rate adequate for two-phase flow studies. The motivation is to get an image without zones suffering of a lack of sensitivity. In frequently used adjacent strategy, the sensitivity is high in the peripheral zone of the study volume but low in the centre. Given the unavoidable measurement and modelling errors, the noise corruption first degrades the centre of the images. Diagonal, opposite and adaptive scanning strategies have different sensitivity profiles (Kauppinen et al., 2006), but inevitably yield non-uniform sensitivity. The idea of the full scan strategy is to apply all possible excitation patterns involving a pair of source and drain electrodes. Considering an array of 16 electrodes, there are 120 different pairs. Let us refer to the set of electrodes as $\{E_1, E_2, \dots, E_{16}\}$ and let $S(E_i, E_j)$ be the excitation pattern where the source and drain of the excitation signals are connected to electrodes E_i and E_j . Note that $S(E_i, E_j)$ and $S(E_j, E_i)$ excitations will provide the same information and have the same sensitivity profile. As a result, only a single of these two symmetric excitations will be required in the full scan strategy. The set of the excitations for a 16 electrodes sensor contains $\frac{1}{2} \cdot 16 \cdot 15 = 120$ patterns:

$$\{S(E_1, E_2), S(E_1, E_3), S(E_1, E_4), \dots, S(E_1, E_{16}), S(E_2, E_3), S(E_2, E_4), \dots, S(E_{15}, E_{16})\} \quad (2.13)$$

Even though there will be redundant measurements in the frames (*i.e.* linearly dependent), the weighting of each measurement can provide a mean to homogenise the sensitivity of the system. For example, the information of a measurement for excitation $S(E_1, E_3)$ will be linearly dependent on the measurements for excitations $S(E_1, E_2)$ and $S(E_2, E_3)$. Yet, the sensitivity for central regions of measurements for the first excitation will be higher than for the last two adjacent excitations. Kauppinen et al. (2006) have presented a numerical study on the sensitivity of adjacent measurements of a 16 electrode sensors for various excitation patterns (in the case of a homogeneous medium). In the full scan strategy, using two single channel multiplexers instead of a single differential channel multiplexer is a requirement.

2.4.3 Digital signal processing

Filtering

In electrical tomography, the frequency of the excitation signal f_{exc} is set by the user and the electromagnetic problem does not predict distortion of the spectrum by the system. In ProME-T, a single frequency AC sinusoidal waveform is considered. As a result, the measurements shall feature the same frequency but different amplitude and phase that are functions of the complex transfer function of the system. In practice, various phenomena occur and induce noise in the measurements that can be partly filtered: (I) non-linearities introduced by the electronic circuit generates higher order harmonics of the signal, (II) channel-to-channel cross-talks create interference, (III) switching simulation pattern induce transient regimes lasting a given settling time, and (IV) measurement system may pick up external source of noise. Filtering the signals is essential in order to reduce measurement errors. In ProME-T, the analogue signals on each of the 16 channels are read simultaneously and continuously by the

PXIe-6368 card (details can be found in the device specifications of the NI PXIe-6368). The filtering is fully digital after sampling and discretisation of the analogue signal. The acquisition is set for the total time duration corresponding to a sequence of N_f frames (or single frame with $N_f = 1$). The sampling frequency f_{acq} is a multiple of the excitation frequency f_{exc} : $f_{acq} = N_{spp} \cdot f_{exc}$ with $N_{spp} \in \mathbb{N}^*$ the number of samples per period. The number of periods $N_p \in \mathbb{N}^*$ for each excitation pattern is selected and the resulting frame rate for the full scan strategy is $f_{fps} = \frac{f_{exc}}{120N_p}$. The processing of the digital data consists in 4 operations: (i) slicing into the 120 excitation patterns, (ii) eventually discarding the first data points, (iii) performing the Discrete Fourier Transform (DFT) of the time series and (iv) recording the amplitude and phase of the component at the excitation frequency.

- (i) The slicing into 120 equal length vectors is motivated by the full scan strategy presented in the previous Section 2.4.2.
- (ii) The first data points corresponding to the signal settling time after a transient may be discarded to reduce measurement errors at the expense of the frame acquisition rate. The signal settling time will be discussed in more details in a subsequent Section 2.6.1. The operational set-up that captures a single period per excitation and does not discard any samples in the post-processing is referred to as the *ultra-fast* acquisition mode in ProME-T. Other acquisition modes have been implemented in ProME-T, for a control of the number of periods per excitation pattern N_p , and the number of periods to be discarded in the post-processing.
- (iii) The resulting time series, associated to one specific excitation pattern, capture N_p periods and contains N_s samples of the signal: $x^{sig} = \{x_0^{sig}, x_1^{sig}, \dots, x_{N_s-1}^{sig}\}$. The DFT of the digital signal also contains N_s samples: $x^{DFT} = \{x_0^{DFT}, x_1^{DFT}, \dots, x_{N_s-1}^{DFT}\}$. The $x_{N_p}^{DFT}$ element corresponding to the excitation frequency and is referred to as the fundamental frequency of the signal. The $x_{N_p \cdot (i+1)}^{DFT}$ elements are the i^{th} order harmonics, with $i = 2, 3, \dots$. Because of the sampling, the x_i^{DFT} element of the DFT corresponds to the $\frac{i \cdot f_{acq}}{N_s}$ analogue frequency, but can also be impacted by signals in the frequency bin: $\left[\frac{(i-1/2) \cdot f_{acq}}{N_s}, \frac{(i+1/2) \cdot f_{acq}}{N_s} \right]$. For non-periodic parasitic signals such as residual potentials caused by multiplexers switches (see subsequent Section 2.6.1), the higher the number of samples in the DFT vector, the higher the filtering effect will be. This spectral decomposition of the signal gives a possibility to assess the quality of the signal in term of Total Harmonic Distortion (THD) and Signal to Noise Ratio (SNR), which is the focus of the subsequent Section 2.5.1.
- (iv) The $x_{N_p}^{DFT}$ element of the DFT of the signal is a complex value characterised by its modulus and phase. In ProME-T, only the moduli have been considered in the post-processing. Yet, the reconstruction can be carried on with complex numbers in order to provide the phase image yielding valuable information of biological samples notably (due to the dielectric nature of cell membranes) (Schlaberg et al., 2008).

Recasting of the data and normalisation

The frame data consists of 120 values for each of the 16 channels. Channel n°0 measures the voltage drop across the sense resistor $R_s = 200 \Omega$ to deduce electrical current I and channels n°1 to n°15 measure the differential voltage across adjacent electrodes in Volt (n°1 for E_1 and E_2 , etc.). For the sake of clarity, let V_i be the complex voltage measurement on channel n°i, for any of the excitation pattern. The electrical current flow I through the test section is given by Ohm's law: $I = \frac{V_0}{R_s}$ (in Ampere). Next, the voltage measurements on channels n°1 to n°15 are normalised for a unit current, *i.e.* as if a constant current was injected with a VCCS:

$$\left\{ \hat{V}_i = \frac{V_i}{I}, i = 1, 2, \dots, 15 \right\}. \quad (2.14)$$

Finally, the electrode potentials $\{V(E_i), i = 1, 2, \dots, 16\}$ are calculated with all the normalised inter-electrode and the reference of the ground potential according to Equation (2.12):

$$\{\hat{V}_i = V(E_{i+1}) - V(E_i), i = 1, 2, \dots, 15\} \quad (2.15)$$

$$\sum_{i=1}^{16} V(E_i) = 0 \quad (2.16)$$

2.4.4 Full procedure for fast EIT

The procedures for frame acquisition have been coded with the LabVIEW graphical language, the recommended software for managing the National Instruments products. The flow diagram is indicated in Figure 2.18. The user sets the following inputs: excitation frequency f_{exc} , amplitude, phase, number of frames N_f , number of periods per pattern N_p and samples per period N_{spp} .

The system is prepared by powering on the MUXs (two analogue output channels set to V_{dd} and V_{ss} for power supply, and setting two digital outputs to True for powering on). In the next stage of the sequence, a sinusoidal waveform is generated with the parameters set by the user, over $N_f \cdot 120 \cdot N_p$ periods with N_{spp} samples per period. Tests are made to check the maximum acquisition frequency for the hardware is not exceeded. The matrix containing 8-bits binary address of the source and drain electrodes for each excitation pattern in the full scan strategy is loaded. The parameters set by the user are used to repeat lines and generate a waveform (because the clocks for the analogue output and the digital outputs are synchronised at the same frequency: f_{acq}). Depending on the state of the operating system, the preparation can take considerable time. Once the system is ready, an optional stage waits for command by the user (to control the effective time of the start of measurements). The digital and analogue waveforms are loaded into the memory to the output channels. Instructions are given to the analogue inputs to collect $N_f \cdot 120 \cdot N_p \cdot N_{spp}$ samples. The analogue output task runs with its internal sample clock (up to 3 MHz). The digital output task clock is set on the rising edge of the analogue output sample clock. The analogue input task is set on the rising edge of the PFI0

Chapter 2. Prototype development

clock that is routed to the digital output sample clock. The timing resolution and accuracy of the analogue I/O clocks are 10 ns and 50 ppm of sample rate respectively.

A sinusoidal 1 Volt with adjustable frequency is used as an excitation signal. The data collection method proposed for ProME-T is the full scan strategy and provides flexible use of the data for different applications. The measurements are acquired without interruption for the entire frame sequence, stored, and post-processed. The data is sliced, filtered with Digital Fourier Transform and finally recast into a format equivalent to a system with current control of the excitation.

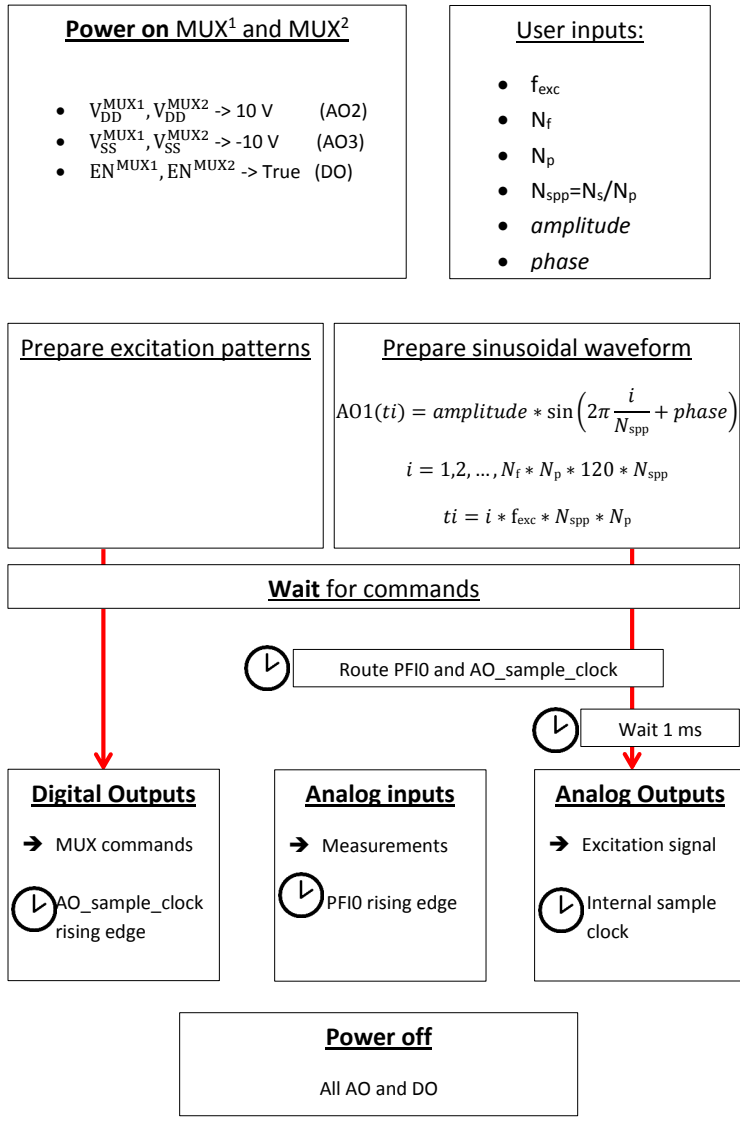


Figure 2.18: Flow diagram of frame acquisition procedure with ProME-T

2.5 Performance assessment of ProME-T

The performance assessment of the electrical measurements can help in future development of a reconstruction algorithm by providing an estimate for experimental errors. It is interesting because it sets the limit on the achievable spatial resolution for the EIT system. This section presents a spectral analysis of measured signals, an assessment of the repeatability of the measurements, a comparison with analytical and numerical solutions and a test of image sequence acquisition in ultra-fast mode.

2.5.1 Noise and uncertainties in signals of ProME-T

The various phenomena that distort the response of the EIT system for a excitation at frequency f_{exc} have been explained in 2.4.3. The protocol for processing of digital signals partly filters some of the noise. Yet, it is interesting to assess the performance of the system excluding the digital filter. It has been explained that the components of the DFT correspond to a bandwidth $\Delta f = \frac{f_{acq}}{N_s}$ in the frequency domain, so the performance of the filter increases with the number of samples. Since available samples are limited in fast EIT, it is crucial to understand how much noise will remain after the filtering operation.

An experiment has been performed using a excitation of 1 V_{AC} at $f_{exc} = 5$ kHz across adjacent source and drain electrodes E_1 and E_2 (no switching operation). 1,000,000 samples were obtained in 2 s, at 500 kHz acquisition frequency. Given the high number of samples, the frequency resolution of the signals' spectra is $\Delta f = 0.5$ Hz. The measurement on channel n°1 across electrodes E_1 and E_2 corresponds to a high amplitude signal (≈ 1 V) while on channel n°9 across electrodes E_9 and E_{10} the signal has an extremely low amplitude (≈ 1 mV). These two representative signals are illustrated in the time domain and in the frequency domain respectively in Figure 2.19 and in Figure 2.20.

Despite the contrast between the fundamental tone of the signal and other frequency components, the log-scale highlights the contribution of the higher-order harmonics (generated by non-linearities in the electronics of the data acquisition system) and of the low frequency noise. The relative importance of higher-order harmonics qualitatively seems to be scaled with the amplitude of the signal at the excitation frequency. The baseline noise level is homogeneously distributed at all frequencies, and can be related to white noise. It is not scaled with the amplitude of the signal. Even without excitation signal, the baseline level of noise is quite similar. The contribution of the 16-bits ADC discretisation error is marginal: for 1,000,000 samples and the gain selected for ± 1 V, the noise in each frequency band would be 3×10^{-11} . The timing accuracy of the sample clock and the shielding of the PCB are two other identified contributors to the baseline noise level and are investigated.

Let us recall the notation $x^{DFT} = \{x_0^{DFT}, x_1^{DFT}, \dots, x_{N_s-1}^{DFT}\}$ for the DFT of a signal x^{sig} . The total harmonic distortion (THD) represents the level of harmonics relative to the power of the

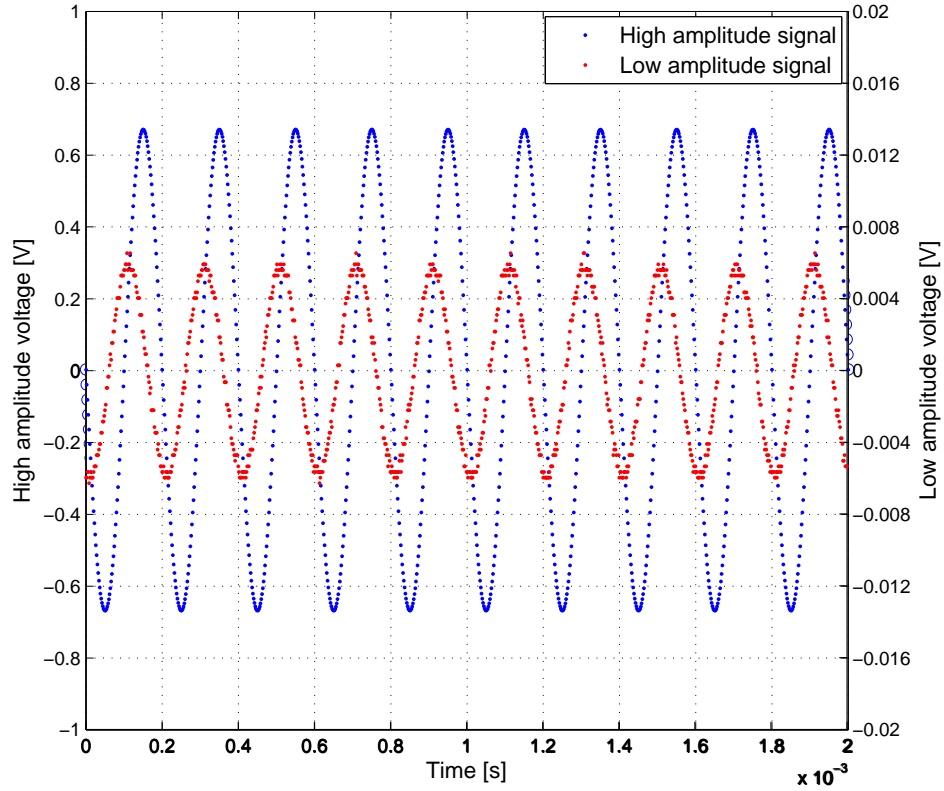


Figure 2.19: 10 periods of low and high amplitude signals

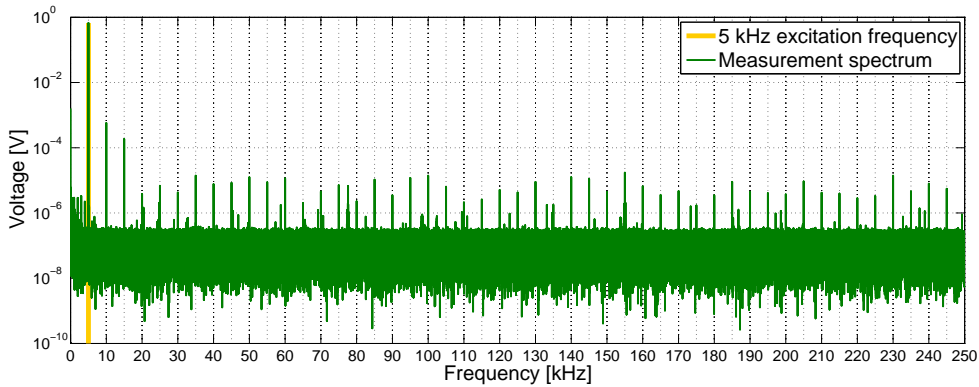
fundamental tone and can be conveniently expressed in decibels (dB):

$$THD = 10 \cdot \log_{10} \left(\frac{(x_{N_p}^{DFT})^2}{\sum_{i=2}^{N_s/N_p} (x_{N_p \cdot i}^{DFT})^2} \right) \quad (2.17)$$

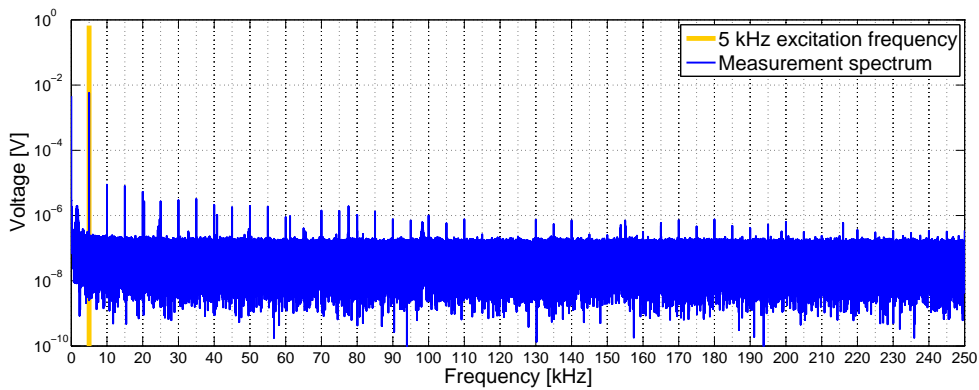
The signal to noise ratio (SNR) represents the level of noise (all frequency components but the fundamental tone) relative to the signal at 5 kHz:

$$SNR = 10 \cdot \log_{10} \left(\frac{(x_{N_p}^{DFT})^2}{\sum_{i \neq N_p} (x_i^{DFT})^2} \right) \quad (2.18)$$

These two indicators are shown in Figure 2.21 for the signals of various amplitudes measured on the 16 channels. The THD and SNR worsen with lower amplitude signals down from 50 mV. In terms of power level, the baseline noise contributes significantly more than higher order harmonics, with approximately 10 dB additional. The data sheet of the PXIe-6368 card specifies the THD for the analogue input channel is 80 dB at full scale (± 10 V). Additional



(A) Spectrum of high amplitude signal



(B) Spectrum of low amplitude signal

Figure 2.20: Spectra of high and low amplitude signals for a 1 Volt 5 kHz excitation

non-linearities can originate from the analogue output channel and from the multiplexers.

2.5.2 Repeatability of the EIT measurements

An appealing approach in EIT consists in considering voltage change between a reference and image frames. Typically, tomographic measurements obtained for a study volume homogeneously filled with the conductive phase are taken as reference, and the data sent to the algorithm will be the voltage difference of the image frame and the reference frame. The principal advantage is to get rid of systematic errors, notably additional impedances specific to a given sensor (unavoidably resulting from geometric errors in the manufacturing of the test section, see Section 2.3.2). However, this approach requires to have a reference measurement available with identical set-up (in particular the same liquid temperature), which might be difficult conditions to meet in practical applications, especially for continuous flow monitoring.

Estimation of the repeatability of tomographic measurements is an essential task in the

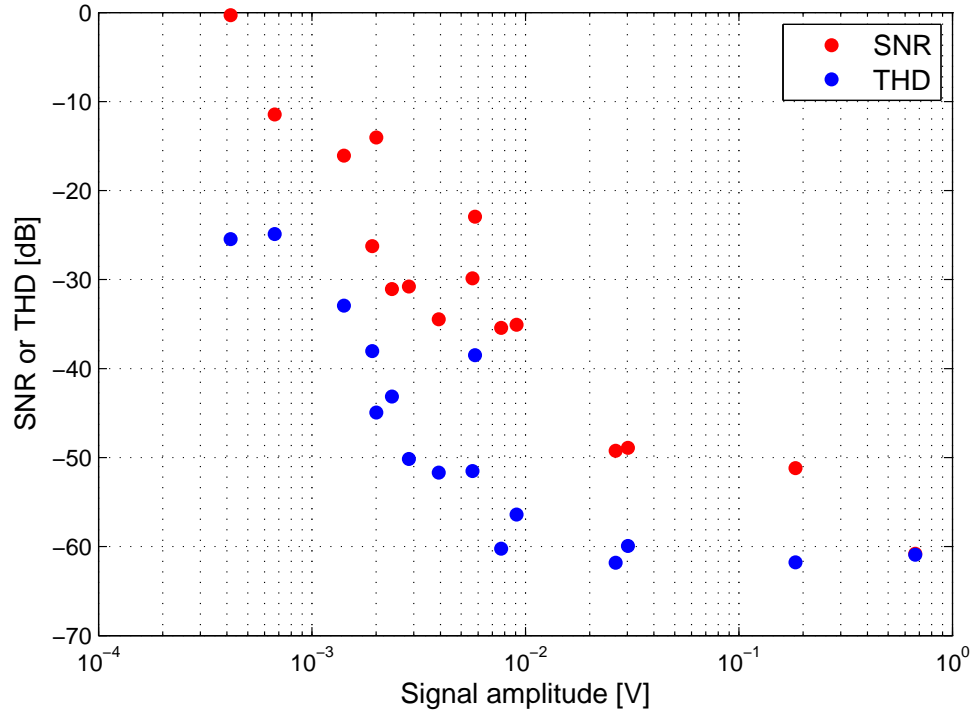


Figure 2.21: THD and SNR of signals on 16 measurement channels for 1 V_{AC} 5 kHz excitation

assessment of the performance of the system. The researchers at Leeds University have demonstrated the repeatability of their measurements with the root-mean square of relative changes RMS_{rc} (Wang et al., 2005):

$$RMS_{rc} = \sqrt{\frac{1}{104} \sum_{i=1}^{104} \left(\frac{V_{mea_i} - V_{ref_i}}{V_{ref_i}} \right)^2}, \quad (2.19)$$

where V_{ref_i} and V_{mea_i} are the i^{th} voltage measurement value in the reference frame and other frames respectively. The authors used the adjacent data collection strategy with a 16 electrodes sensor, yielding 104 measurements per frame. The repeatability is taken as the average of the RMS_{rc} over a sequence of images captured at 1163 fps for an excitation frequency at 80 kHz. A repeatability of 0.4% has been demonstrated by the authors. The researchers at Cape Town University also demonstrated the repeatability of the system (Wilkinson et al., 2005). However the experiment was fundamentally different since *"the electrode system was replaced by a resistor network"*. *"The average standard deviation was 2.5 mV, which is <0.25% of typical maximum values in the measurement sequence"* (182 measurements over a sequence of 100 frames). This expression of the repeatability is less adequate than that in Wang et al. (2005) for measurements with various amplitudes in ProME-T. Moreover, using a resistor network considerably change the result of repeatability. As compared with the test in static liquid ($RMS_{rc}=0.40\%$), this test using a resistor network gives a significantly different figure of merit ($RMS_{rc}=0.25\%$) (Wang et al., 2005).

Chapter 2. Prototype development

In a similar state of mind, an experiment has been set up to assess the repeatability of ProME-T. 200 consecutive frames (1920 measurements each) of a homogeneously filled water medium have been acquired in the ultra-fast acquisition mode. Filtering is performed on the measurements and only amplitude of the DFT component at the excitation frequency is considered in the analysis. The normalisation and computation of electrode absolute potentials are not performed. Three different excitation frequencies, $f_{exc} = 20, 50$ and 80 kHz, have been analysed. The relative standard deviation of the measurements on the 16 channels and 120 configurations against the amplitude of the signals is shown in Figure 2.22. The results tend to cluster into 2 or 3 lines on this log-log plot. This correspond to an inverse relationship $y(x) \propto \frac{1}{x}$ with the signal amplitude, expected from relative standard deviation measurements. Each line being spaced approximately by a factor of two, a possible explanation for this clustering effect could be related to discretisation errors. In order to support this hypothesis, the error propagation in the DFT result has been calculated (Dupré et al., 2015), and the predicted relative discretisation error as a function of the signal amplitude for a 16-bit DAC is also indicated in Figure 2.22. It gives a good lower bound estimate of the repeatability of measurements. In a typical frame, 29% of the measurements correspond to high amplitude signals (>0.1 V) for which the relative error is much less than 0.1%.

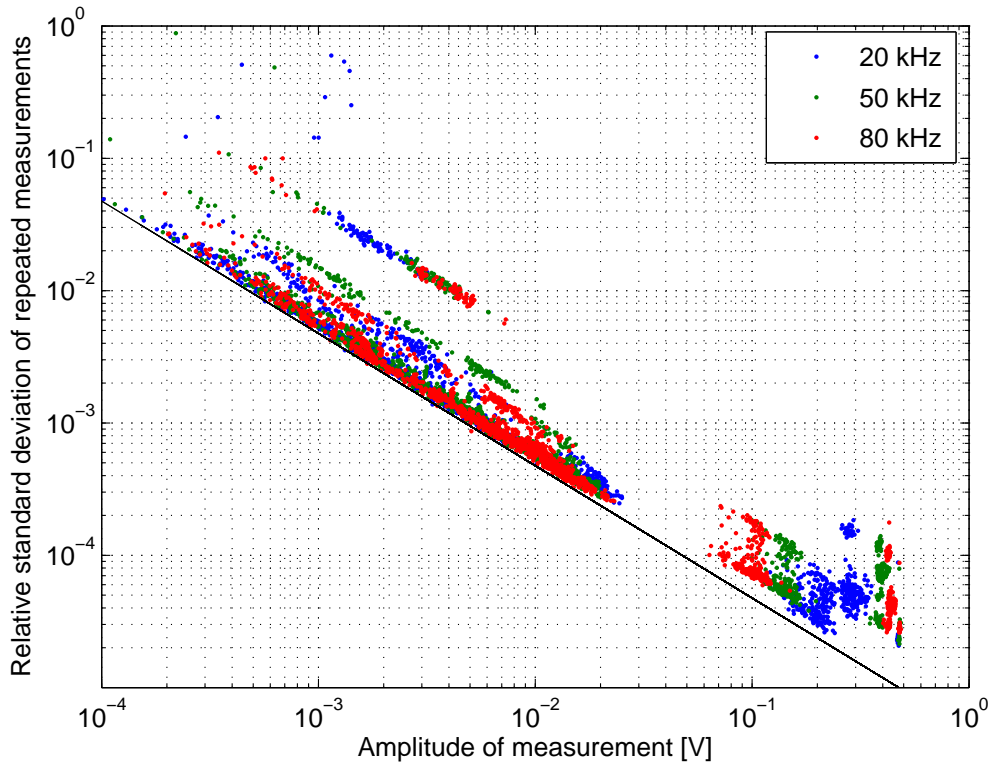


Figure 2.22: Relative standard deviation of repeated identical measurements

The root-mean square of relative changes for this experiment with the ProME-T sensor, at 80 kHz, was 0.87%. The figure of merit is conform to the standard of the other fast EIT systems mentioned previously and gives prospect on the performance of the ProME-T prototype sensor

for relative image reconstruction. The comparison of these systems is shown in Table 2.1, and the frame rate is indicated assuming the adjacent data collection strategy is implemented.

System	Leeds University	Cape Town University	ProME-T
Frame rate (adjacent)	1164 fps	1143 fps	5000 fps
Repeatability	0.40%	0.25%	0.87%
Excitation	sinusoidal current 80 kHz	switched DC current pulse $64\mu s$	sinusoidal potential 80 kHz
Reference	(Wang et al., 2005)	(Wilkinson et al., 2005)	(Dupré et al., 2017)

Table 2.1: Comparison table of 3 fast EIT systems

2.5.3 Comparison with analytical and numerical solutions

Anticipating the complexities of adaptation in harsh flows, an original procedure has been set to prevent the need for obtaining a reference frame. Typically, a measurement of the homogeneous reference medium is taken at the start of each experimental session. If this is not possible to obtain this reference in the case of continuous flow monitoring, because of a temperature drift or the impossibility to reach reference conditions, one needs to consider alternative solutions. The solution proposed consists in calibrating the sensor by assessing the electrode-specific impedances and will be explained in details in subsequent Section 2.6.3. After calibration, the reliability in absolute terms of the electrical measurements can be assessed by a comparison with analytical and numerical simulation results. As a reminder of the forward problem, the reader can refer to Equations (2.8), (2.9), (2.11) and (2.12) for the expression of the Maxwell equations and the boundary conditions.

In this study, a homogeneous medium has been considered. One of a few analytical solutions of the EIT direct problem in the literature is given in George et al. (2000) for a 2D circular domain of constant conductivity σ , considering a current per unit length I injected in (x_0, y_0) and withdrawn in $(x_0, -y_0)$:

$$V(x, y) = \frac{I}{2\pi\sigma} \ln\left(\frac{(y_0 + y)^2 + (x_0 - x)^2}{(y_0 - y)^2 + (x_0 - x)^2}\right) \quad (2.20)$$

Alternatively, the solution can be obtained numerically with finite element methods solvers. The EIDORS software (Polydorides, 2002) has been used in this thesis to provide the solutions to the forward problem. Details on the solver and the models will be given in Section 4.2.1. In this particular study, a 2D disk model with 1 mm arc electrodes has been used. The experiment has been performed in the *2D configuration* of the test section, *i.e.* without using the two cylindrical extensions. Opposite source and drain electrodes have been selected. Due to the small axial extent of the study cylindrical volume (5 mm) in this configuration, the electromagnetic field can be approximated as two-dimensional. Indeed, the current is injected through electrodes having a 1 mm diameter cross-section, and the height of the domain is 5

Chapter 2. Prototype development

mm. Since the analytical solution is valid for point electrodes with infinitesimal cross-section, there is a singularity at the current injection electrodes (infinite voltages). In order to tackle this problem, the analytical solution for the electrical potential at current injection electrodes in Equation (2.20) has been averaged over a 1 mm chord length.

The normalised inter-electrode differential voltage measurements in the 2D configuration are compared with the analytical and numerical solutions. The results are shown in Figure 2.23. In Figure 2.24, the voltage profiles predicted by the analytical and simulation results are presented with the electrode potential derived from experimental measurements.

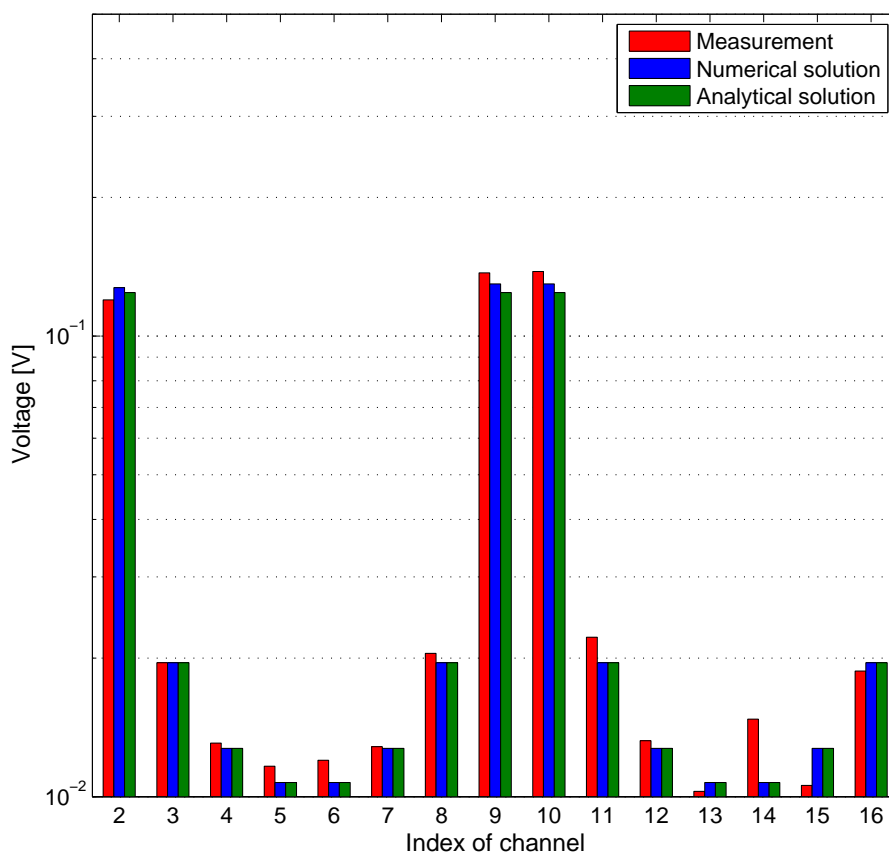


Figure 2.23: Comparison of analytical, numerical solutions and measurements on 16 channels

This study brings confidence on the absolute reading of the measurements obtained with ProME-T and the procedure that transforms differential inter-electrode voltage measurements into normalised absolute voltage measurements. The calibration procedure presented in subsequent Section 2.6.3 is essential to compensate the measurements for the voltage drop at the current injection electrodes.

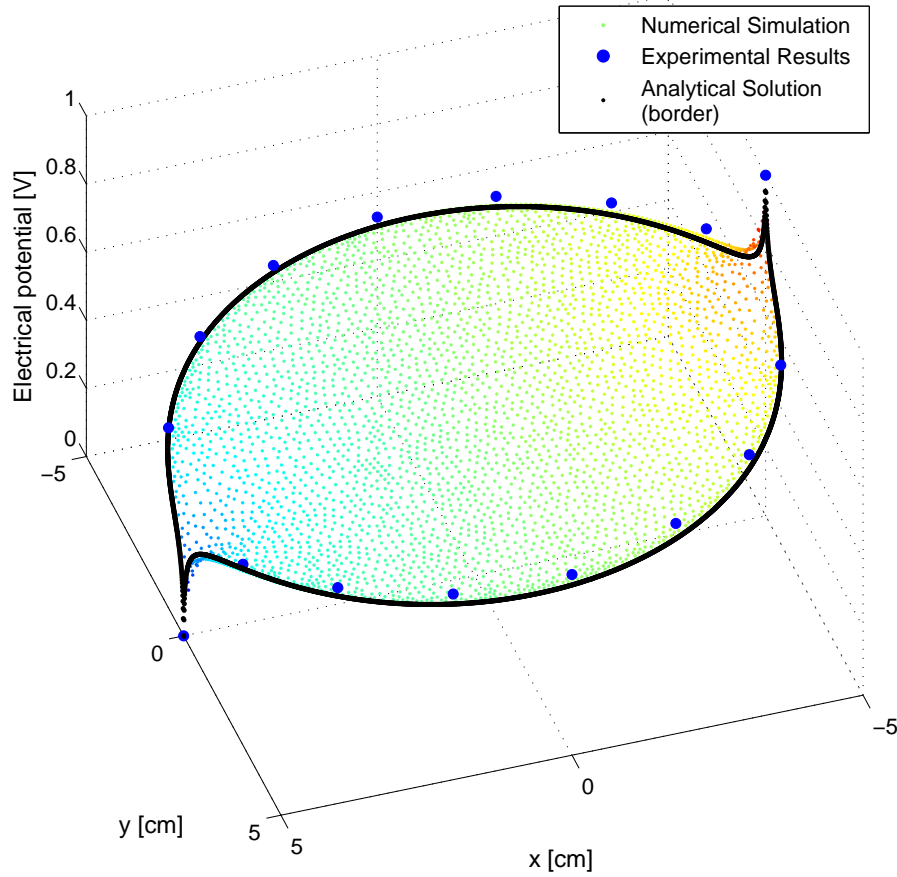


Figure 2.24: Comparison of numerical, analytical voltage profiles and experimental prediction

2.5.4 Acquisition of image sequence in fast mode

In order to illustrate the high frame rate potential of the ProME-T sensor, a sequence of images was taken in the ultra-fast acquisition mode while two spherical objects were dropped in the test section. This simplistic experiment simulates the dynamical response of the sensor for high velocity flows. Two spheres S_1 and S_2 were dropped in the test section filled with a saline solution of NaCl of conductivity $\approx 2000 \mu\text{S} \cdot \text{cm}^{-1}$. Their dimensions are approximately equivalent ($D_1=22.1 \text{ mm}$ and $D_2=25.3 \text{ mm}$) but their densities differ ($\rho_1=5697 \text{ kg} \cdot \text{m}^{-3}$ and $\rho_2=1144 \text{ kg} \cdot \text{m}^{-3}$). According to the equations of motion with gravitational, buoyancy and drag forces, both spheres have reached their terminal velocities v_{term} by the time they cross the plane of electrodes:

$$v_{term} = \sqrt{\frac{(\rho_{sphere} - \rho_{water}) \cdot g \cdot 4/3 D_{sphere}}{\rho_{water} \cdot C_x}}, \quad (2.21)$$

with ρ_{sphere} the density of the sphere, ρ_{water} the density of the water, g the standard acceleration of free fall, D_{sphere} the diameter of the sphere, and C_x the drag coefficient for a sphere in a turbulent flow.

Chapter 2. Prototype development

The frame acquisition rate was 667 fps, with a 80 kHz excitation frequency. The estimated velocity of S_1 and S_2 are $v_{term,1}=1.76 \text{ m} \cdot \text{s}^{-1}$ and $v_{term,2}=0.33 \text{ m} \cdot \text{s}^{-1}$ respectively. The image sequences reconstructed from the data are shown in Figure 2.25. Tomograms are stacked along the z axis. The 16 electrodes are indicated in green for a better visual effect of the cylindrical test section. The image reconstruction technique in this study is very approximative: the EIDORS package is used and a NOSER 3D inversion algorithm is implemented. A slice at the plane of the electrodes is selected and a simple filter is used to remove the noise components for better visualisation of the stacked image sequence. The reconstruction is very preliminary as compared with the algorithm presented in subsequent Chapter 4. The image sequence is quite remarkable qualitatively. S_1 is visible on 28 frames while the slow sphere S_2 is visible on 119 frames. Assuming the trajectory of the two falls were the same, S_2 remained in the sensing volume 4.25 times longer than S_1 , which is in qualitative agreement with the theoretical predictions ($\frac{v_1}{v_2} = 5.3$). If the sensing volume would be restricted to the plane, the signal associated with S_1 would last 12.6 ms (*i.e.* 8 frames), and 77 ms with S_2 (*i.e.* 51 frames). As expected, the tomography is sensitive to the presence of the spheres beyond the cut plane.

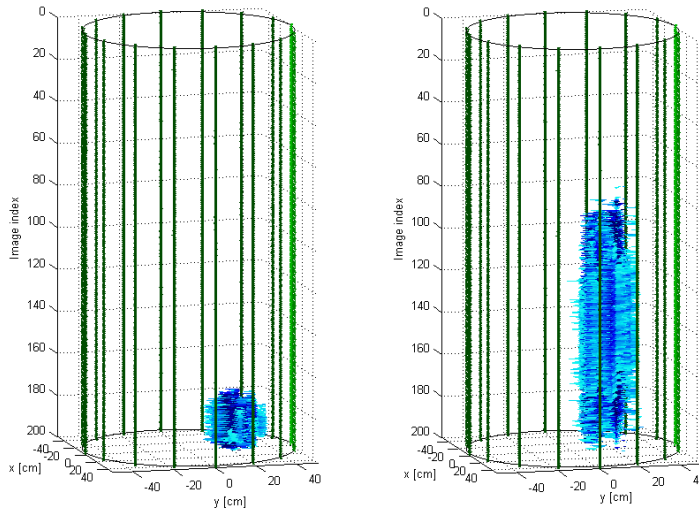


Figure 2.25: Image sequence at 667 fps of two gravitationally falling spheres: on the left, S_1 with $D_1=22 \text{ mm}$, $\rho_1=5697 \text{ kg} \cdot \text{m}^{-3}$; on the right, S_2 with $D_2=25 \text{ mm}$, $\rho_2=1144 \text{ kg} \cdot \text{m}^{-3}$

The performance of the prototype EIT system has been assessed with a set of dedicated studies. Noise and distortion of the signal introduced by external effects or internal parasitic effects have been analysed. The background noise level is the major contributor to the noise. The repeatability of the measurements with the full scan sequence at different frame acquisition rates has been assessed. The results are comparable with other existing fast EIT systems. The reliability of the absolute measurements has also been tested by a comparison with analytical and numerical solutions. The last study is an qualitative illustration of the performance of the ultra-fast acquisition mode.

2.6 Studies for fundamental understanding

The phenomenon of electrode-electrolyte contact impedance is contributing to the mismatch between measurements and predictions of the forward model. The problem caused by such systematic errors can be bypassed by using differential image reconstruction algorithms. These algorithms consider the relative voltage change between a known reference frame and the unknown frame. Alternatively for absolute image reconstruction, it is necessary to understand and model the additional impedances specific to each electrodes.

2.6.1 Signal settling time

The switching operation from one excitation pattern to another is a transient phenomenon. Despite the filtering by the procedure for data acquisition of out-of-frequency components in the signal, significant errors can remain if sufficient data is not discarded. The time the signal takes to settle can be very dependent on the electronic design of the EIT system. In order to analyse this effect, a specific experiment has been designed. A data frame is captured (homogeneous reference medium). The frequency of the excitation signal is $f_{exc}=10$ kHz. For each excitation pattern, measurements last 10 periods of the excitation signal. The measurements are sorted in 4 categories: (1) the measurement on channel n°0 across the current sense resistor, (2) the high amplitude signals at current injection electrodes, (3) the measurements at electrodes used for injection of current in the previous excitation pattern and (4) all other measurements. Representative illustrations of signals of each sort are shown in Figure 2.26.

The signal is sliced in 10 periods, and the DFT is performed. The relative error (taking the result of the 10th period as reference) is computed. The relative errors of the 9 periods for illustrative signals in the 4 categories are shown in Figure 2.27. For signals of type (1) (2) and (4) the relative error for the 1st period seldom exceeds 1%. However, the bias in the measurement of the first period for signals of type (3) is serious, from 10 to 100%. This study highlights the need to better understand the cause of this differences in decay time depending on electrodes.

It is attributed mainly to the electrode-electrolyte contact impedance described in subsequent Section 2.6.2. In Wang and Ma (2006), the authors have proposed a procedure to "*eliminate the charged residual potential of measurements*". It is called the over-zero switching scheme (OZS) and consists in operating the switch at the peak value of the AC current. With an electronic model of the fast EIT sensor, the authors show this method effectively cancels out the main contribution to the charged residual at current injection electrodes. The OZS scheme has been also implemented in ProME-T. Yet, the analysis of signal settling time suggests the charged residual potentials are less than in the set-up of Wang et al. (2005). Eventually, the absence of VCCS and difference in electrode geometries could explain the different behaviour of the EIT systems. As a result of using the OZS scheme, the number of periods is always an integer. Therefore, the number of periods to be discarded in the post-processing also is an integer. An important improvement is obtained by discarding the first period only.

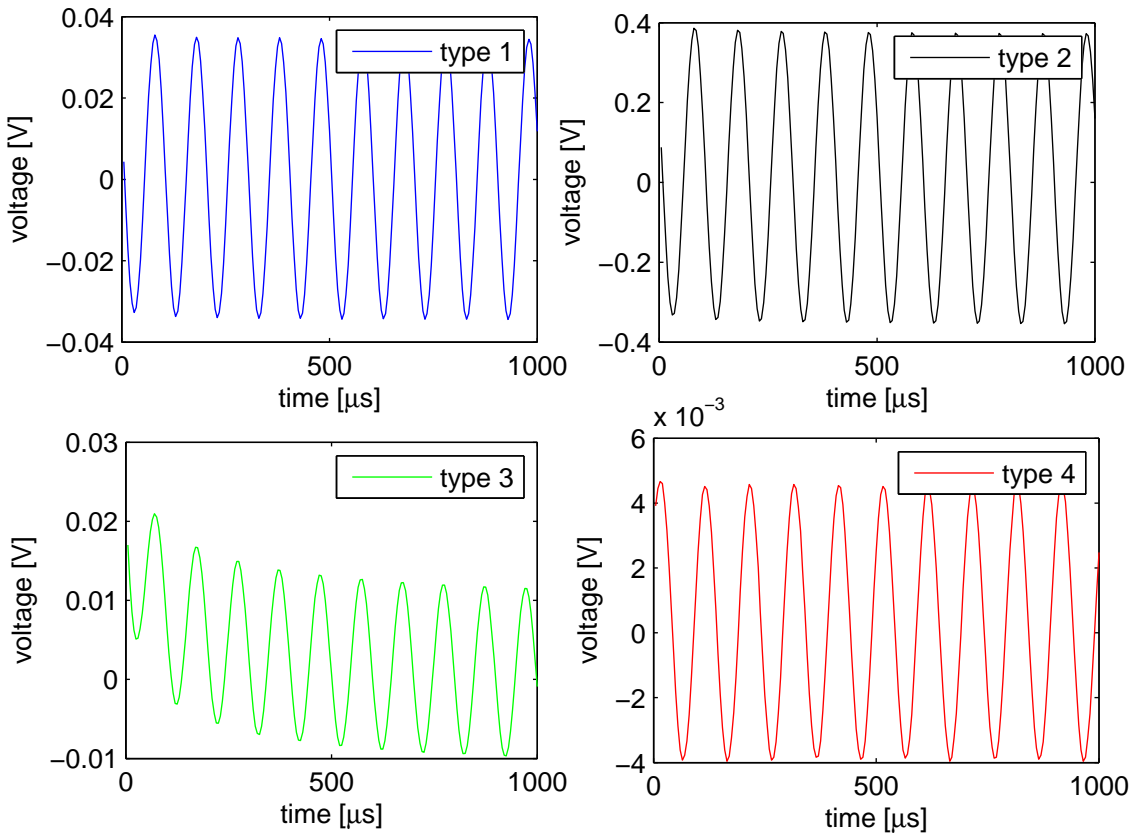


Figure 2.26: Illustration of settling signals in the four categories

An ongoing investigation consists in trying to discard only a fraction of a period. The idea would be to replace the discarded measurements based on the last samples. Observing that the signal settling often resemble an exponential decay, another idea would be to subtract an estimate, based on the DFT vector, of the contribution of this exponential at the signal frequency.

2.6.2 Electrode-electrolyte contact impedance

At the electrode-electrolyte interface, a double ion layer forms when a static electrical potential is set. Ions of the first layer are adsorbed onto the metal electrode. Ions on the second diffuse layer are attracted to the surface via the Coulomb force. The two layers essentially act as a dielectric. The phenomenon fades with increasing excitation frequency. Clearly, the phenomenon needs to be avoided or modelled, otherwise the additional impedances will bias the absolute values of the voltage measurements at the current injection electrodes.

The total impedance of the EIT system can be modelled as a serie of the source and drain electrode-specific impedances and the bulk impedance of the medium, as is sketched in Figure 2.28. The frequency-dependent electrode-electrolyte contact impedance at source

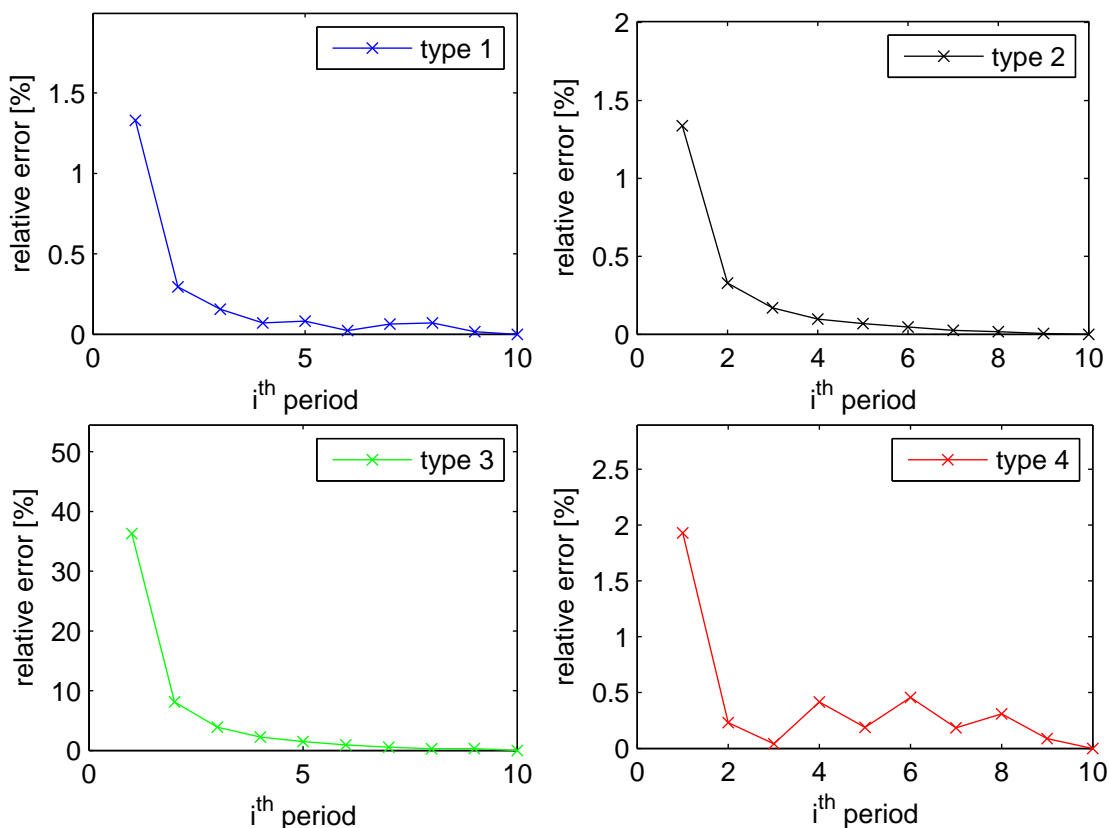


Figure 2.27: Analysis of the settling of signals in the four categories in terms of relative error

and drain electrodes contributes to the electrode-specific impedance. In ProME-T, with the control of the voltage ($1 V_{AC}$) of the simulation signal and the measurement of the current I through the test section, the total impedance of the EIT system, Z , is simply the inverse of the current measurement according to Ohm's law:

$$Z = \frac{V}{I} = Z^{source} + Z^{drain} + Z^{bulk} \text{ with } V=1 \text{ Volt} \quad (2.22)$$

In this experiment, the test section is filled with a NaCl solution at various conductivities, and opposite source and drain electrodes are selected (n°1 and n°9). A sweep of excitation frequencies in the range $[1 - 10^5]$ Hz is performed. The total impedance of the EIT system Z is obtained from the measurements on channel n°0 of the voltage drop V_0 across the current sense resistor $R_s = 200 \Omega$: $Z = \frac{R_s}{V_0}$. Figures 2.29 and 2.30 show respectively the modulus and the phase of the complex total impedance for different conductivities of the liquid phase.

At low frequency (typically up to 1 kHz), the contact impedance at the electrode-electrolyte interface contributes significantly to the global impedance. For highly conductive solutions, the

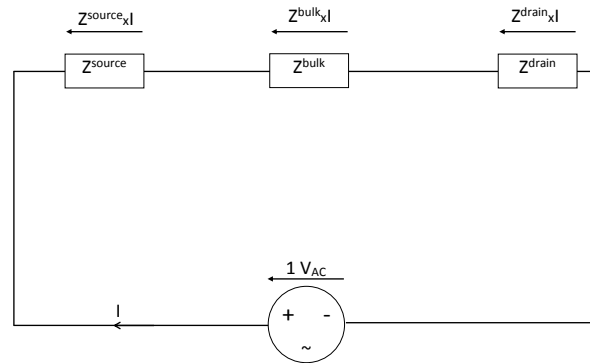


Figure 2.28: Electrical circuit model of the EIT system

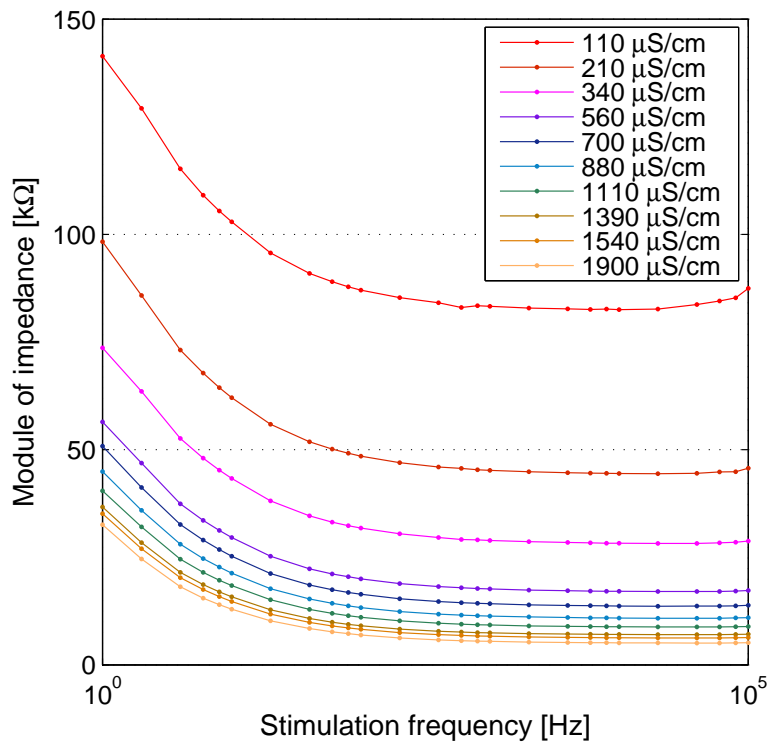


Figure 2.29: Modulus of impedance response of global impedance for various liquid conductivities

effect relative to the resistive regime is more important, as is seen on the phase of the complex impedance in Figure 2.30. At medium frequencies (typically from 1 kHz up to 100 kHz), the total impedance is mainly real: the bulk impedance of the medium (eventually resistance of electronic circuit) dominates the global impedance. Electrical Resistance Tomography (ERT)

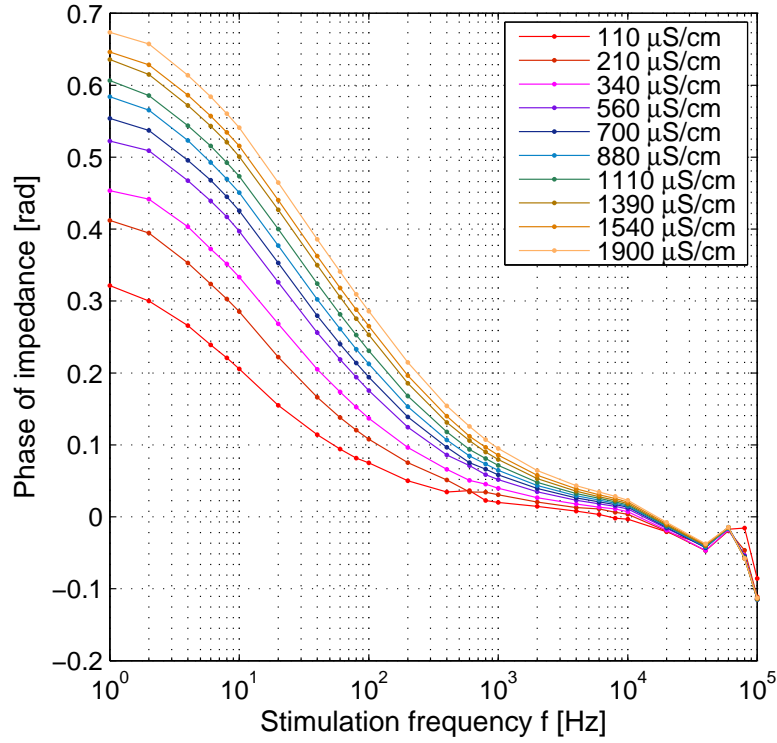


Figure 2.30: Phase of impedance response of global impedance for various liquid conductivities

techniques operate in the interesting frequency range that prevents complex analysis because bulk resistive effects prevail and the electrode contact impedance is not significant. At high frequencies (typically from 100 kHz in highly pure water), dielectric effects need to be taken into account. The electrical complex conductivity of the liquid phase $\gamma = \sigma + i\omega\epsilon$ in Equation (2.8) cannot be approximated as a real number (George et al., 2000). The tangent of γ expresses the relative importance of capacitive effects in the bulk impedance:

$$\tan(\gamma) = \frac{2\pi f_{exc}\epsilon_0\epsilon_R}{\sigma}, \quad (2.23)$$

with ϵ_0 the vacuum permittivity and ϵ_R the relative permittivity of the medium (about 80 for water). For an excitation frequency of 100 kHz, it exceeds one percent when liquid conductivities are less than $447 \mu\text{S} \cdot \text{cm}^{-1}$. In experimental tests with ProME-T, liquid conductivities around $2000 \mu\text{S} \cdot \text{cm}^{-1}$ have been used. Additionally, emergence of parasitic effects originating from the electronic circuit might appear at high frequencies. In early versions of the electronic circuit of ProME-T with breadboard, significant contribution to the total impedance was observed in the range [10 – 100] kHz, which was extremely well fitted by an additional RCL element in the modelling of the total impedance.

In order to better understand the decay of the contribution of contact impedance with increasing excitation frequency, let us define two indicators: the *resistive component* R_t (arbitrarily

Chapter 2. Prototype development

selected at 10 kHz), and the *reactive component* $X_t(f_{exc})$ imputable to contact impedance, defined as:

$$R_t = \|Z\| (10kHz), \quad (2.24)$$

$$X_t(f_{exc}) = \|Z\| (f_{exc}) - R_t. \quad (2.25)$$

The *resistive component* R_t and *reactive component* $X_t(f_{exc})$ (arbitrarily selected at 1 Hz) of the total impedance are shown in Figure 2.31 for liquid conductivities ranging from 100 to 2000 $\mu\text{S} \cdot \text{cm}^{-1}$. As expected, the resistive effects closely follow the inverse proportionality with the liquid conductivity. The capacitive effects (imputable to contact impedance) decay more slowly with increasing liquid conductivity.

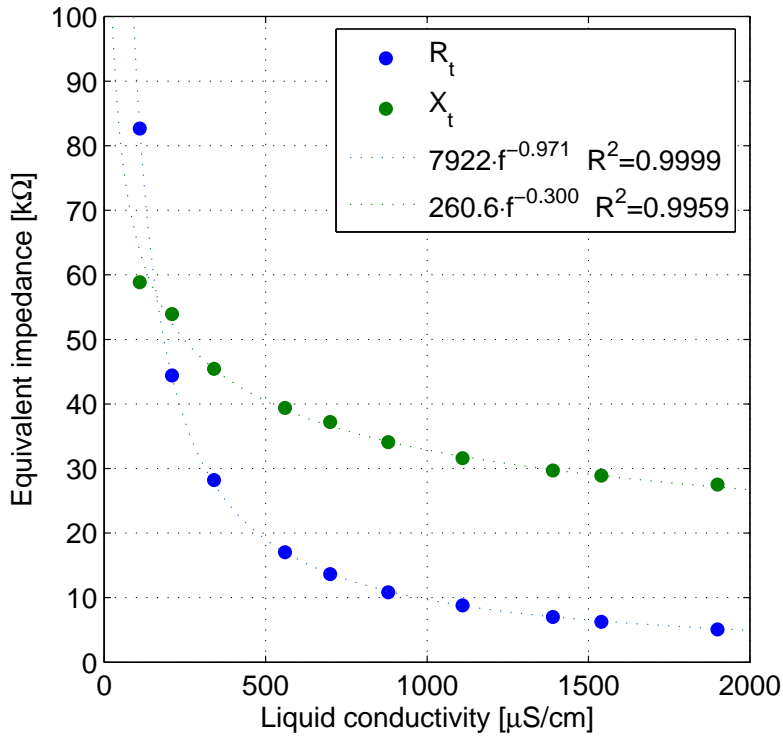


Figure 2.31: Conductivity dependence of the indicators R_t and $X_t(1\text{Hz})$

The results shown in Figure 2.31 indicate that highly conductive solutions present higher capacitive effects at low frequencies. Yet, regardless of the liquid conductivity, the additional impedance imputable to contact impedance decreases quickly with increasing excitation frequencies. In Figure 2.32, the *reactive component* as a function of the excitation frequency is shown. The decay is well described with a power law, with a coefficient -0.5 for low frequencies and -1 for higher frequencies. Surprisingly, the usually accepted parallel RC model of the contact impedance (Wang et al., 2005) would predict a coefficient -1 for low frequencies and -2 for higher frequencies. The model mismatch could not be satisfactorily explained by the

author.

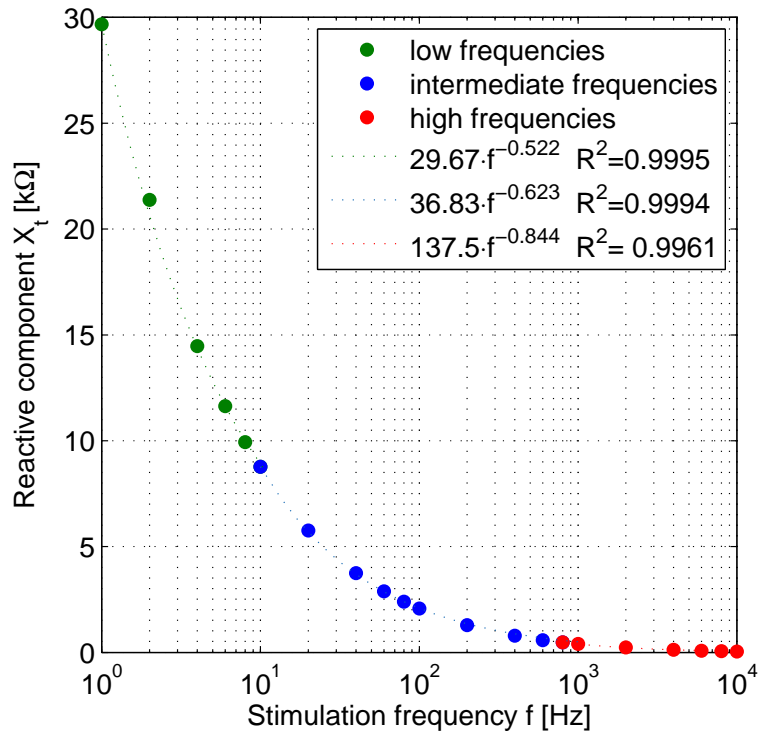


Figure 2.32: Attenuation of capacitive effects with increasing excitation frequency

Platinum electrodes are used in ProME-T because this metal yield a low contact impedance (Wang et al., 2005). Contact impedance is very complex to model because it depends on the liquid conductivity, the excitation frequency and electrode properties (material, surface state, etc.). It adds a bias in the voltage measurements at the current injection electrodes. However, it is a systematic error, which means it can be ignored when relative change in measurements are considered, or with calibration. The study highlight the contact impedance does not decrease as fast as the bulk resistance with increased liquid conductivity. It shows also that the intensity of the phenomenon decays with increased excitation frequency, and confirm the consensus in the literature about optimal frequency range in the order of [10 – 100] kHz (George et al., 2000).

2.6.3 Calibration procedure for impedance mismatch

Systematic errors are unavoidable because of the extreme sensitivity of the point-like electrode design to misalignment and because of the impossibility to let the signals settle after a change in the excitation pattern. In order to get reliable absolute readings of the measurements involving current injection electrodes, it is crucial to correct the measurements for the electrode-specific impedances. A procedure has been designed to find the set of the 16

Chapter 2. Prototype development

electrode-specific impedances. This information can be considered as a calibration of the sensor, and shall be assessed once for all for a given sensor. Measurements of a homogeneously filled test section and the calibration data is extracted from the set of total impedance obtained from channel n°0 for each of the 120 excitation patterns: $\{Z_{S_1}, Z_{S_2}, \dots, Z_{S_{120}}\}$. The total impedance measured for the excitation pattern $ptn \in \{S_1, S_2, \dots, S_{120}\}$ is modelled as the sum of electrode-specific impedance at current injection electrodes and the bulk impedance of the homogeneous medium:

$$Z_{ptn} = Z_{ptn}^{source} + Z_{ptn}^{drain} + Z_{ptn}^{bulk} \quad (2.26)$$

, with electrode-specific impedances $Z_{ptn}^{source}, Z_{ptn}^{drain} \in \{Z_{E_1}, Z_{E_2}, \dots, Z_{E_{16}}\}$ and bulk impedance $Z_{ptn}^{bulk} \in \{Z_{b_1}, Z_{b_2}, \dots, Z_{b_8}\}$.

The set of bulk impedance for the homogeneous medium has 8 possible configurations, according to angular separation between source and drain electrodes, due to the symmetry of the model of the sensor. This operation yields a sparse linear system of 120 equations (for each excitation pattern) with 24 unknowns (16 electrode-specific impedances and 8 bulk impedances). Though the system is overdetermined, in theory it should reduce to a consistent system. In practice, after the calibration, slight deviations about $\pm 0.3\%$ were observed between the equivalent calibrated measurements, *i.e.* after subtraction of electrode-specific impedances, and the bulk impedance obtained by solving the linear system of 120 equations.

The procedure for calibration has been tested for the 2D and 3D configurations of the sensor (with or without extensions, see Figure 2.10). Figure 2.33 compares the measurements of total impedance and the calibrated values for the 3D configuration. All 120 calibrated measurements are almost identical, irrespectively of the angular separation of current injection electrodes. This special case for point-like electrodes and long cylindrical test section has been observed as the result of this experiment first, then verified by numerical simulations (see Figure 2.12). This finding highlights the superiority of reliable absolute readings of EIT measurements by calibration over the strategy of preventing systematic errors by considering measurements change between two frames. Figure 2.34 compares the measurements of total impedance and the calibrated values for the 2D configuration. The bulk impedance of the homogeneous medium increases with increasing angular separation of current injection electrodes, a more intuitive result. Again, the symmetric calibrated measurements presents only slight deviations.

The switch operated by the multiplexers is a transient phenomenon. An idle time before processing to the data acquisition is often set. However, this is limiting the frame acquisition rate of fast EIT systems. The measurements at electrodes used in the previous excitation pattern for current injection are the most sensitive. In ProME-T, the settling time observed is relatively short and the Digital Fourier Transform provides a partial filtering of the residual potentials. The frequency-dependent electrode-electrolyte contact impedance is a contributor

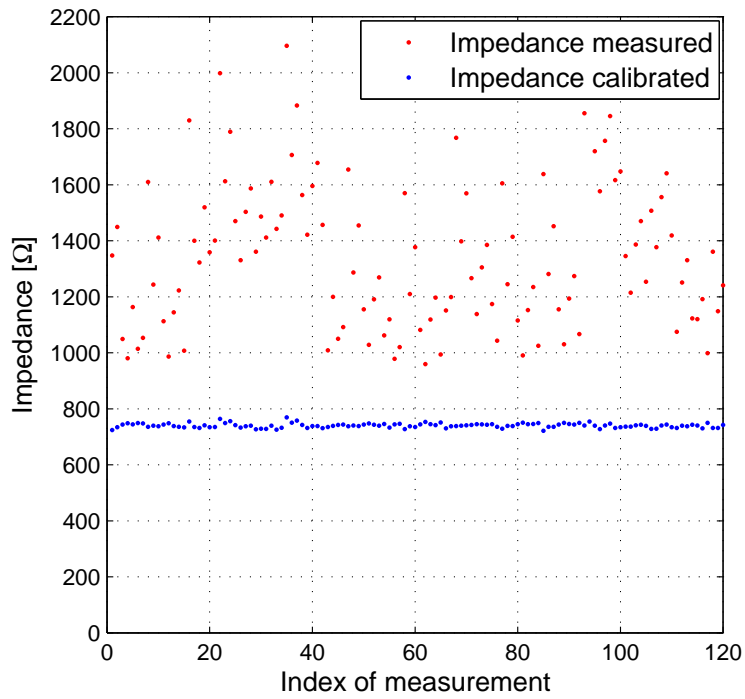


Figure 2.33: Measured and calibrated impedance (3D)

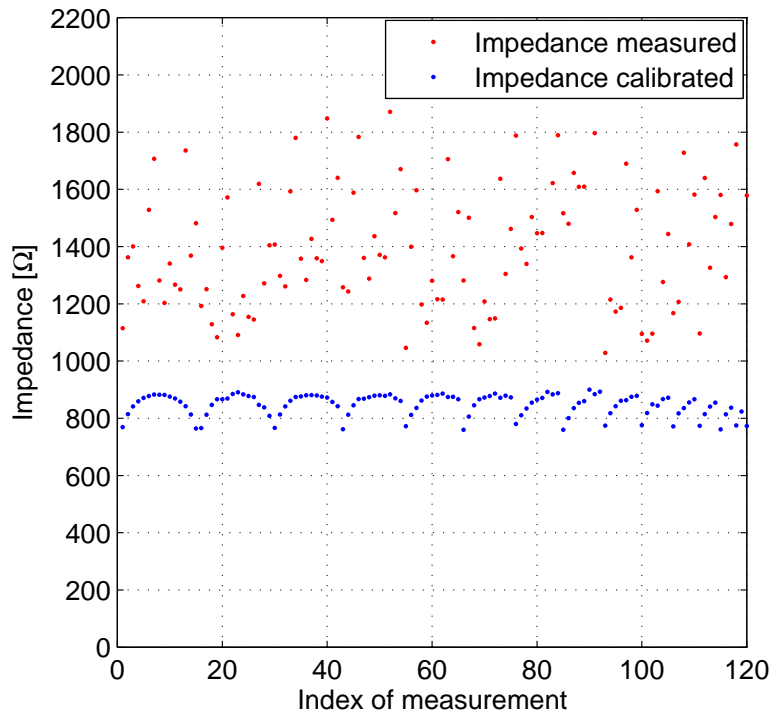


Figure 2.34: Measured and calibrated impedance (2D)

Chapter 2. Prototype development

to the residual potential and is investigated. Another investigation show that the errors in the geometry of the sensor are another contributor to the mismatch in total impedance for different excitation patterns. Using the novel full scan strategy, a calibration procedure has been proposed for correcting the total impedance measurements using a set of electrode-specific impedances.

3 Flow regime identification

Multiphase flows are typically sorted into categories referred to as *flow regimes* depending on the prevailing rheological conditions. The flow regimes identification (FRI) methods are a straightforward strategy to extract important parameters and provide the user the essential information one will need for the basic understanding. The plan is to use the results of flow regime identification methods from raw EIT measurements in order to provide an approximate *a priori* image for the image reconstruction algorithm. An experimental campaign to obtain ECT measurements associated to each of the regimes of air-water horizontal flows was launched in February 2016 within the framework of a collaboration with Professor Saba Mylvaganam of University College of Southeast Norway. A well instrumented multiphase flow rig with a functioning ECT module has been made available for the studies. The analysis of the experiments provided the basis for the development of an original method for flow regime identification. Though the proposed criteria for regime identification were developed and tested for a particular set-up and an ECT sensor, the methodology is based on mechanistic models of flow regimes that should be valid for other set-ups and for EIT sensors.

3.1 Overview of flow regime identification

Flow regime identification (FRI) methods are appealing because the information provided helps to select the right model for assessing global parameters such as cross-sectional average void fraction for instance. Its application with the raw signal of an electrical tomography system enable to extract essential information, bypassing the image reconstruction process and the associated difficulties.

3.1.1 Multiphase flow regimes

The short introduction to fluid dynamics in Section 1 highlights the complexity of numerical simulations of multiphase flow because of the numerous and complex rheological mechanisms that drive their dynamics. Yet, many approximations can be made depending on the

Chapter 3. Flow regime identification

peculiarity of each application. The mass, momentum and energy transfers of multiphase flows are very sensitive to the topology of the distribution of phases (Brennen, 2005). Very good results can be obtained in practice with models adapted to broad categories of flow topologies, referred to as *multiphase flow regimes* in the scientific literature. Typically, each steady-state flow is analysed according to the prevailing rheological mechanism: *e.g.* gravity, surface tension, gas momentum, etc. As an example, stratified, annular, and bubble flow regimes are encountered in horizontal gas-liquid flows. The prevailing mechanisms for these three regimes are respectively gravity, gas momentum, and surface tension.

Developed flows can be parametrised with a limited set of parameters (typically the input mass flow rates of each phase) in a given experimental set-up (pipe geometry, inclination, nature of phases). Assessing the flow regime experimentally (Mandhane et al., 1974) or theoretically (Taitel and Dukler, 1976) within this framework leads to the concept of multiphase flow regime maps. It is a very active field of research. With the help of flow regime maps, the flows can be analysed in a very simplified manner with a limited set of parameters specific to each flow regimes (Hernandez, 2008; Pradeep and Mylvaganam, 2015). Notably, the cross-sectional average void fraction is the most important parameter for gas-liquid continuous flows.

Gas-liquid horizontal flow regimes

The typology of gas-liquid developed flows in horizontal pipes is classically described with a set of seven flow regimes, sketched in Figure 3.1. An example of flow regime map is shown in Figure 3.2.

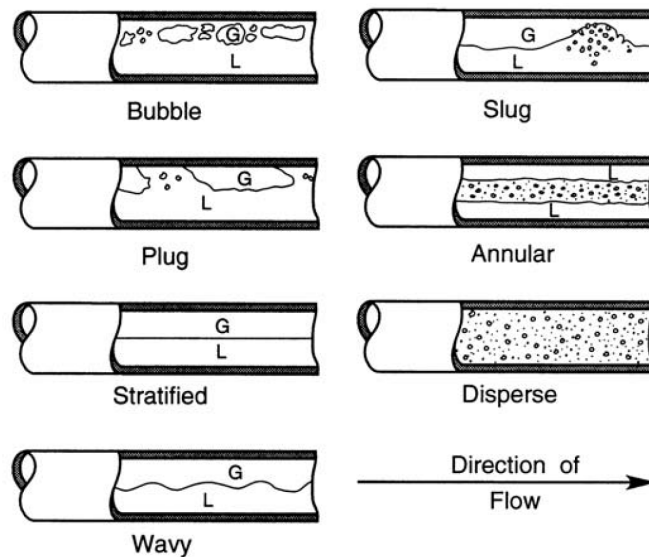


Figure 3.1: Sketches of flow regimes for flow of air/water mixtures in a horizontal, 5.1cm diameter pipe. Adapted from Brennen (2005)

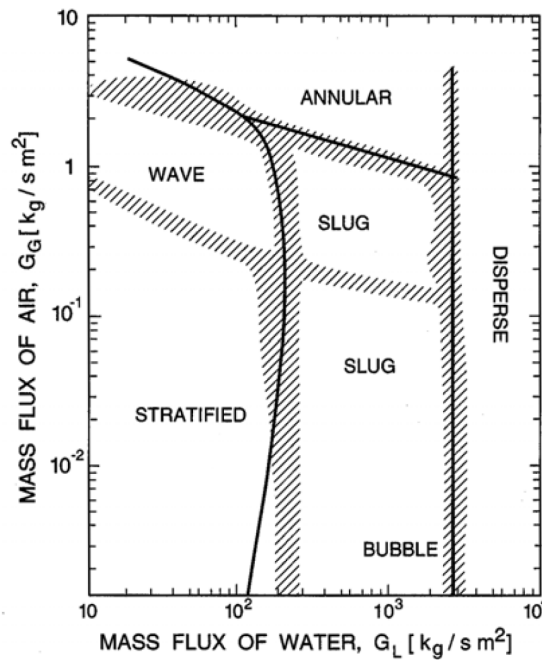


Figure 3.2: Flow regime map for the horizontal flow of an air/water mixture in a 5.1 cm diameter pipe. Hatched regions are observed regime boundaries, lines are theoretical predictions. Adapted from Brennen (2005)

Gas-liquid vertical flow regimes

The typology of gas-liquid developed flows in vertical pipes is classically described with a set of five flow regimes, sketched in Figure 3.3. An example of flow regime map is shown in Figure 3.4.

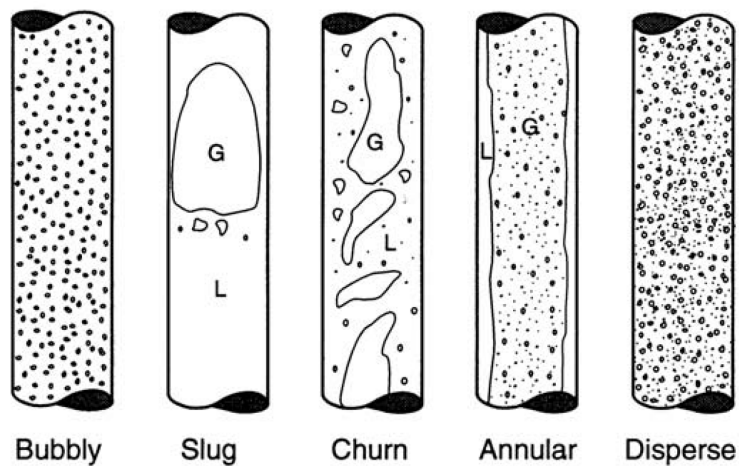


Figure 3.3: Sketches of flow regimes for two-phase flow in a vertical pipe. Adapted from Brennen (2005)

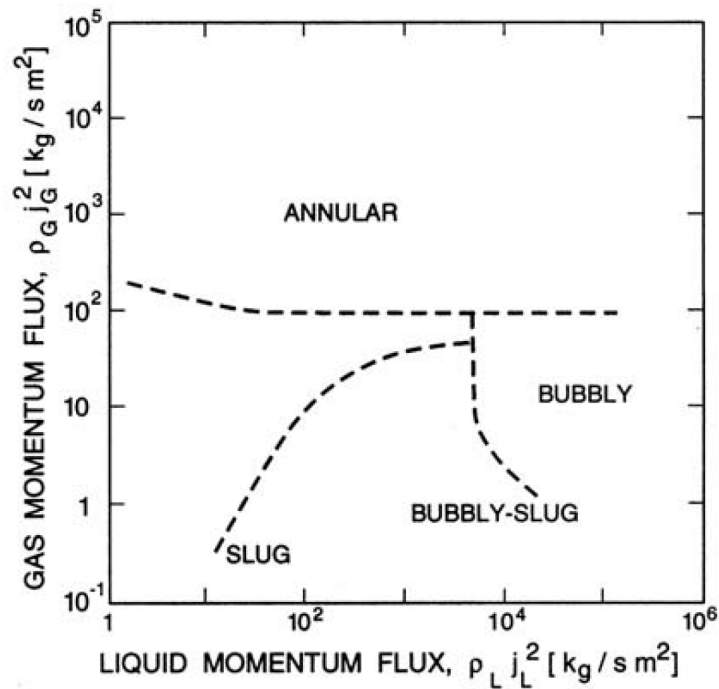


Figure 3.4: The vertical flow regime map of Hewitt and Roberts (1969) for flow in a 3.2 cm diameter tube, validated for both air/water flow at atmospheric pressure and steam/water flow at high pressure. Adapted from Brennen (2005)

3.1.2 Flow regime identification

There is an important diversity of sensors that have been used for flow regime identification. Many of the methods have been successfully applied to various modalities, and multi-modality sensing is a hot topic in this research field (Pradeep and Mylvaganam, 2015; Pradeep, 2012; Ru and Mylvaganam, 2013).

Single time series

FRI studies have frequently used analysis of single time series using statistical tools such as power spectral density (PSD), probability density function (PDF) (Ahmed and Ismail, 2008; Lowe, 1997; Lowe and Rezkallah, 1999; Paranjape et al., 2012; Rocha and Simões-Moreira, 2008). In Hervieu and Selegim jr. (1998), Gabor's transform time-frequency covariance advanced statistical tool is used to assess the "unstationarity degree" of a transitional flow, which highlights the potential of statistical tools for the analysis of flow regimes. Often the signal of a single sensor is used, e.g. impedance or capacitance probes (Ahmed and Ismail, 2008), radiation-based densitometers. Alternatively, signals from multiple sensors are merged into one, e.g. multi-electrode impedance sensors (Mi et al., 2001; Selegim and Hervieu, 1998), wire-mesh (Schleicher et al., 2016). In all cases, the signal needs to be representative of the cross-sectional average void fraction, which can be challenging with regard to the design of

the sensor (Ahmed and Ismail, 2008; Libert et al., 2016).

Multi-signal analysis

With the emergence of advanced method to analyse the patterns (notably machine learning algorithms), researchers have started to consider multiple signals in the regime identification. Yet, there are too many independent measurements in electrical tomography: 66 for a 12-electrode ECT system or 104 for 16-electrode EIT system. Principal component analysis (PCA) is an appealing tool for data reduction. Wang and Zhang (2009) have reduced 66 measurements into 14 principal components (based on a representative set of experimental data), that are later processed with machine learning algorithm. Tan et al. (2007) used multi-dimensional wavelet transform to extract features in the "*wavelet-scale domain*". Tan et al. (2015) have used multivariate analysis to extract information out of the tomographic data.

Machine learning

In most of past research, the flow regime identification consists in the comparison with "*fingerprints*" in a database (Xie et al., 1989b; Ahmed and Ismail, 2008). The recent trend in flow regime identification is to use machine learning algorithms (Haykin, 2009).

Artificial neural network algorithms are somewhat inspired of the biological structure of the brain, and are declined in three main types according to their structure: feed-forward, recurrent and self-organising networks (Alme, 2007; Alme and Mylvaganam, 2006). Some authors suggests their use in flow regime identification is less arbitrary than other methods (Mi et al., 2001; Lee et al., 2008). Yet, major interrogations remain about the generalisation of the results beyond the trained data mapping (*e.g.* for different temperature, geometry, *etc.*).

Support vector machines (SVM) are efficient algorithms for classification into high-dimensional feature spaces. Wang and Zhang (2009) used data from 100 numerical simulations to train the algorithm and 30 others to test it. The representativity of the training data set is a recurrent question with machine learning.

3.1.3 Research with electrical tomography

The research on flow regime identification has applications beyond the specificity of a single modularity. Indeed, video recordings, pressure differential sensors, radiation-based densitometers, electrical and optical probes can be used amongst many other example. However, electrical tomography techniques are interesting sensing modalities due to the fast response and tomometric data. Furthermore, as compared to hard-field tomography techniques such as advanced X-ray tomography, the image reconstruction problem for soft field is considerably more challenging and flow regime identification is an appealing alternative to extract important information without resorting to imaging (Dupré et al., 2016b).

Chapter 3. Flow regime identification

In electrical tomography, the flow regime identification techniques can be sorted into two categories depending if they are based on (i) tomographic images or (ii) raw tomometric measurements. In the first category (i), the motivation is often the *"extraction of synthetic information, which is essential to understand and model the specific phenomena"* (Polansky et al., 2015). This information enables *"the selection of the optimal method for metering"* (Ram-skill and Wang, 2011; Ru and Mylvaganam, 2013). In the second category (ii), an alternative *"simpler signal-processing system"* is preferred to image reconstruction (Xie et al., 1989b). While the analysis of single time series is an option to identify intermittent flow regimes, many researchers have focused on data reduction to preserve the spatial information of tomometric data. In Fang and Cumberbatch (2005), the analysis of the eigenvalues of the capacitance matrix of an ECT system provides condensed information adapted to distinguishing annular, core and stratified flows.

In principle, images of multiphase flows are limited to the physically occurring distribution of phases. According to the prevailing mechanism, flows can be sorted into flow regimes with different topologies. Flow regimes identification techniques are appealing for analysis of electrical tomography data without solving the complex reconstruction problem of imaging.

3.2 Experimental setup and campaign

The details on the experimental setup of the multiphase flow rig of University College of Southeast Norway (UCSN) are presented in this section. Details on the instrumentation and the ECT module in particular are presented. The experimental campaign aimed at measurements of characteristic horizontal gas-liquid flows (stratified, annular, intermittent) and transitional flows is described.

3.2.1 Multiphase flow rig

The multiphase flow rig at UCSN enables the injection of mineral oil, water and air in a horizontal or near-horizontal pipe made of PMMA (see P&ID and photograph of the rig in Figures 3.5 and 3.6). Each medium flowing into the pipe section is monitored independently using dedicated meters. The electrical properties of the three phases are monitored to facilitate the use of ECT. The relative permittivity ϵ_r (dimensionless) and the conductivity σ in $\text{mS} \cdot \text{cm}^{-1}$ of mineral oil, water and air are respectively: $\epsilon_r^{oil}=2.7$, $\epsilon_r^{water}=80$, $\epsilon_r^{air}=1$ and $\sigma^{oil}=0 \text{ mS} \cdot \text{cm}^{-1}$, $\sigma^{water}=2 \text{ mS} \cdot \text{cm}^{-1}$, $\sigma^{air}=0 \text{ mS} \cdot \text{cm}^{-1}$. The conductivity of water is essentially similar to the studies with ProME-T. The input mass flow rates are accurately controlled and monitored by Coriolis flow meters. One can select water mass flow rates up to 150 kg/min and air mass flow rates up to 5 kg/min.

The inner diameter of the pipe is 56 mm and the length is 15 m long, so the flow is developed in the measurement section at its end (see Figure 3.7). In the horizontal configuration, stratified smooth, stratified wavy, annular, plug and slug flows can be generated by selecting the water and air mass flow rates according to a flow regime map for ambient air-water flow in horizontal pipes (Mandhane et al., 1974). Only the dispersed bubble flow cannot be generated because of the limitations of water mass flow rates. Besides, it is possible to position the test section with tilt angles up to $\pm 10^\circ$ to the horizontal. The transparent PMMA test section, meant for optical measurements or high speed videotaping is in the flow loop before a dual-plane 12-electrodes ECT sensor, and a gamma-ray meter. Other sensors commonly used in process measurements, such as differential pressures and flow rates, are used in different sections of the pipe constituting of about 50 tags. The most important signals from differential pressure sensors n°120, n°121 and n°131 (see Figure 3.7) are recorded at 20 Hz acquisition rate, while the various other signals (temperatures, pressures, mass and volume flow rates, etc.) are recorded every second. An extended description of the multiphase flow rig at UCSN can be found in Pradeep (2012). Details on a similar ECT sensor, but for a larger diameter pipe can be found in Alme (2007).

Chapter 3. Flow regime identification

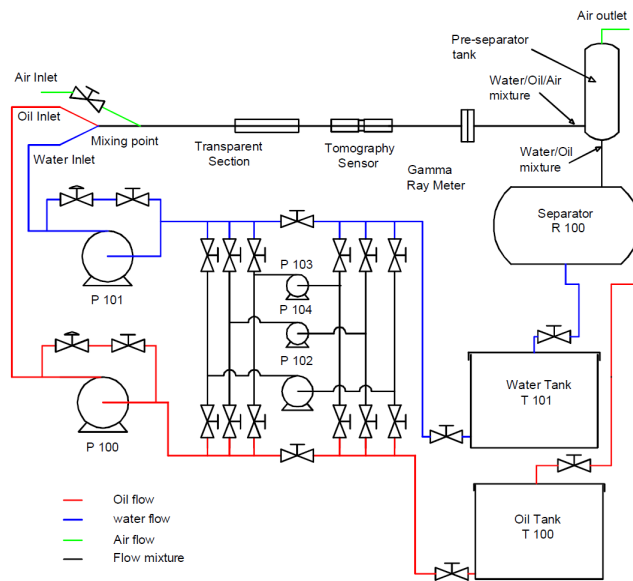


Figure 3.5: P&ID of the multiphase flow loop with ECT and GRM

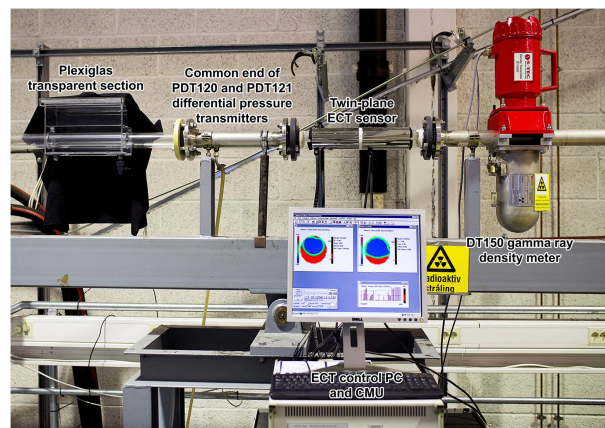


Figure 3.6: Photograph of the multiphase flow loop with ECT and GRM

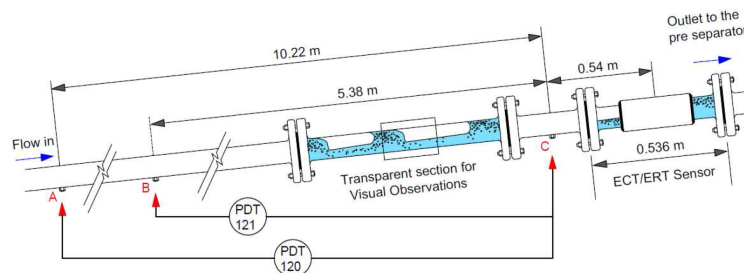


Figure 3.7: Test section with sensor placements, transparent section for high-speed camera based studies, multi-modal tomographic systems and differential pressure transmitters

3.2.2 Instrumentation and ECT sensor

Instrumentation

Gamma-ray meter (GRM) and high-speed camera recordings can provide additional information on the flows and complement the visual observations for the assessment of the flow regimes. The GRM was positioned downstream of the ECT module. It provides a signal at 20 Hz that is correlated with the cross-sectional average phase fraction. The physical principle consists in measuring the attenuation of the radiation originating from a radioactive source, due to the presence of materials with specific stopping power within the sensing volume. Not to be confused with radiation-based tomography, with this instrument, only one projection is made (the source and detectors are kept fixed) and the signal at the receptors is acquired at 20 Hz. The calibration is performed with two measurements for the empty and full pipe, corresponding to maximum and minimum signal amplitudes respectively. The signal has not been used to estimate the cross-sectional average void fraction because extended calibration would be required since it is unclear whether the sensitivity through the sensing volume is uniform or not. However, its variation gives a clear indication of intermittent flows. An example of the GRM signal of an intermittent flow is shown in Figure 3.18 on page 75. High-speed camera has been available in some of the measurement sessions. A compromise had to be found between image resolution and frame rate. In experiments, 130 fps videos were captured because it was sufficient for the visualisation of the fastest liquid slugs.

ECT sensor

A schematic of the dual plane ECT sensor system is given in Figure 3.8, in which a stratified flow scenario is presented. The sensor array used in the ECT module consists of two sets of 12 electrodes placed symmetrically around the periphery of the pipe at a distance making it feasible to perform correlation studies on different flow phenomena. These correlation studies can be either performed on the raw data continuously logged in from the 24 electrodes or on the pixel information from the tomograms generated by the ECT module and the associated software package. One set of capacitance electrodes ($n_C=12$ electrodes, length $l_C = 85$ mm and width $w_C = 11.7$ mm) is symmetrically distributed around the periphery of the pipe of diameter $D_{in} = 56$ mm, on its outer diameter $D_{out} = 60$ mm. An exactly similar set of capacitance electrodes is placed at a distance $L_C = 190$ mm. The sensitivities of these two sets of electrodes are determined by the ratio $\eta_C = n_C \cdot \frac{w_C}{\pi \cdot D_{in}} = 0.80$. The width w_C of the electrodes, corresponding to a 22.3° aperture angle, is typical for ECT sensors for increased sensitivity, but large as compared to the point-like electrode design for EIT. The selection of these parameters will depend on the availability of space for locating the electrodes and the ease of coupling them to each other and to the external hardware needed for measuring the capacitance values. The number of measurements per frame is determined by the multiplexing arrangement and is only half of the combinations possible between all the electrodes assuming negligible change in the constituents of the media in the sensing volume. The ECT module operates

Chapter 3. Flow regime identification

at a frequency of 1 MHz and acquires 100 frames per second. The sensing area $n_C \cdot w_C \cdot l_C$ and the sensing volume $\pi l_C \frac{D_{in}^2}{4}$ will determine the size and number of pixels and voxels in cross-sectional and 3D tomographic studies respectively.

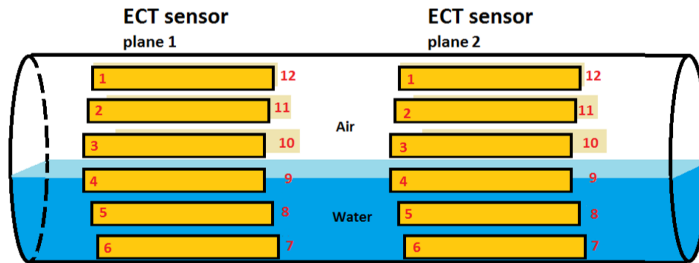


Figure 3.8: Twin plane ECT tomographic system – Arrays of 12 electrodes on the periphery of the pipe section with stratified flow in this schematic, $C_{a,b}$ is the capacitance between electrodes a and b, with $a, b = 1, 2, \dots, 12$

3.2.3 Experiments

A total of 137 experiments for various flow regimes have been performed for this study (115 in the horizontal configuration of the test section, and 22 in the inclined test section). A database has been constructed with approximately 40% of intermittent flows, 40% of stratified flows and 20% of annular flows. Because of limitations in input mass flow rate, measurements of bubbly flows could not be obtained, and as a result this flow regime has not been considered in the methodology that has been developed for horizontal gas-liquid flow regime identification. The selected flow conditions (input mass flow rates of air and water) are shown in the flow regime map given in Figure 3.9 for the horizontal configuration of the test section. A special attention was given at transition flows because their analysis gives extremely valuable insight onto the characteristics of each specific flow regime. For coherence throughout this chapter, the same colour code will be used in figures: green for intermittent flows (light green for plug and dark green for slug), red for annular flows, and blue for stratified flows (light blue for smooth flows and dark blue for wavy flows). The flow regimes indicated in Figure 3.9 have been assessed experimentally by fusing information from all sensors available: visual inspection during experiments, high-speed camera, GRM and ECT tomograms.

The validation of the identification algorithms presented in the following sections relies on our categorisation based on the data from multiple sensors recorded during the series of dedicated experiments performed for this study. Since it is difficult to find objective and consistent definitions of the flow regimes in the literature (Costigan and Whalley, 1997), we will now give a detailed explanation of the manner the flow regimes have been labelled in the context of this study. The author acknowledge the complexity of categorising transitional flows and highlight the need for the research community to tackle this problem. In Figure 3.10,

3.2. Experimental setup and campaign

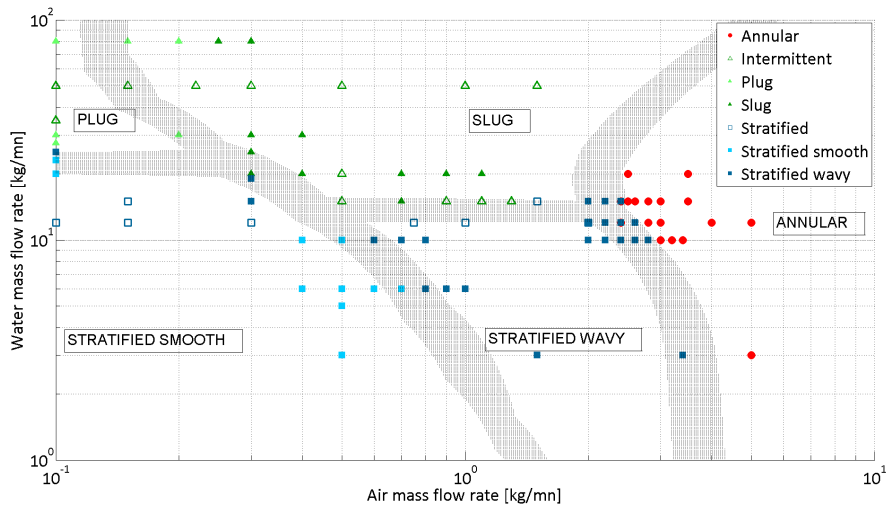


Figure 3.9: Set of 115 experiments in the horizontal configuration, and the flow regimes as identified by experimental means (visual observation, GRM and high-speed camera recordings)

images extracted from high-speed camera recordings of the main flow regimes are shown. Intermittent flows have been best sorted by visual inspection or using the GRM signals. The same technique is used for flow conditions involving transitions of annular and mist slugs. The individual slug or plug are referred to as the *liquid body*. In cases of extreme transition involving intermittent flows with extremely low frequency of liquid bodies, the time window was adjusted to include at least one liquid body. Slugs could be differentiated from plugs using the high-speed video recordings, when bubbles trapped at the front of the unit move on without coalescing at the top from the front to the rear (Figures 3.10e and 3.10f). Unfortunately, high-speed videos were not available at some experimental sessions; therefore the distinction between plug and slug could not be made clearly, thus leaving the label intermittent in Figure 3.9. Transition from stratified to annular flows is very gradual, and the ‘sharp’ categorisation would be made for a complete wetting of the pipe wall. This could be checked on videos as a glare originating from the top of the pipe revealing the presence of a permanent liquid film (Figures 3.10c and 3.10d). The onset of wavy flows was considered when the low frequency coherent waves would show ripples at the surface (Figure 3.10b). At increasing air flow rates, higher frequency waves would form, the flow would still be labelled as stratified wavy (Figure 3.10c). Finally, the specific case of the pipe being filled by water is referred to as *homogeneous flow*.

The flow regime identification algorithm presented in the following section relies solely on the data from an ECT module with an array of 12 electrodes. Capacitance measurements were acquired at 100 frames per second over 60 seconds, giving a data set of 6000 frames, and providing many sets of time series for analysis for each experimental run. The duration of each experiment has been selected to 60 seconds because it is sufficient to capture the rarest events of intermittent flows encountered in the experimental campaign. Yet, the time

Chapter 3. Flow regime identification

window may be adjusted by the user of the algorithm according to the specific applications, thereby increasing or decreasing the amount of samples processed in the algorithms described subsequently. High-speed videos were captured at 130 frames per second over 10 seconds, an image acquisition rate suitable for distinguishing plug from slug and stratified smooth from stratified wavy flows. The GRM was operated at 20 Hz so that intermittent flows could be identified and the frequency of appearance of liquid bodies could be obtained.

The multiphase flow rig at UCSN can generate stratified, annular and intermittent air-water flows in a horizontal pipe. Input water and air mass flow rates are controlled accurately. The ECT sensor has been tried and tested in other researches and provides 100 fps. A set of benchmark experiments has been performed and analysed for the development of a methodology for flow regime identification. Focus has been paid to the transitional flows.

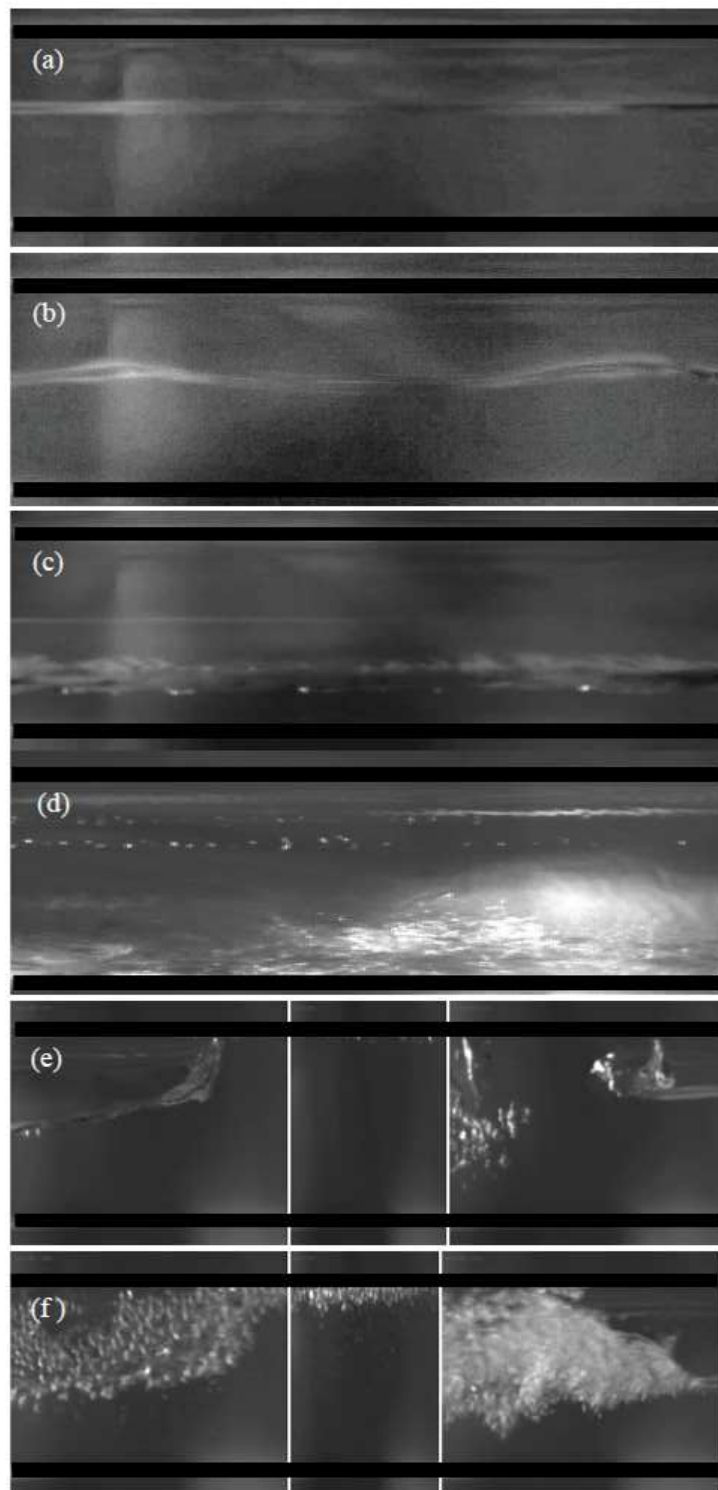


Figure 3.10: Images of typical flow regimes (a) stratified smooth (b) low frequency waves (c) high frequency waves (d) annular (e) rear, bulk, and front of a plug (f) rear, bulk, and front of a slug

3.3 Methodology for identification

The structure of the signal of the ECT sensor is explained and the principles of our methodology for analysing the geometrical and dynamical features of a flow are proposed. Data reduction strategies are detailed.

3.3.1 Data collection strategy of raw ECT signal

In this study, the data of a single array of electrodes of the ECT module was used. The standard data collection strategy in ECT consists in sequentially setting high voltage excitation on the excitation electrode while all other electrodes are connected to ground. For each of the 12 electrodes used in turn as excitation electrode for a frame, the charges resulting on all grounded electrodes are measured sequentially with a sample and hold circuitry. The measurements equivalent by symmetry can be skipped. A capacitance measurement between electrode a and b , $C_{a,b}$, consists in measuring the electrical charge Q on the grounded electrode E_b ($V(E_b) = 0$) resulting from an electrical potential V applied on E_a :

$$C_{a,b} = \frac{Q(E_b)}{V(E_a)}, b \neq a. \quad (3.1)$$

The Farad is the SI derived unit of electrical capacitance. The charge $Q(E_b)$ on an electrode E_b is given by the integral form of Gauss law (see Equation (2.1)) on its surface σ_b :

$$Q(E_b) = \int_{\sigma_b} \epsilon(\vec{E} \cdot \vec{n}) d\sigma_b, \quad (3.2)$$

where \vec{n} is the unit tangent to the infinitesimal surface $d\sigma_b$.

Since the capacitance measurements are symmetric ($C_{a,b} = C_{b,a}$), there are 66 independent measurements in a frame from a sensor with 12 electrodes. The self-capacitance is defined as $C_{a,a} = -\sum_{b \neq a} C_{a,b}$ (Fang and Cumberbatch, 2005). A frame can be conveniently expressed as a 12×12 capacitance matrix \mathbf{C} :

$$\begin{pmatrix} C_{1,1} & C_{1,2} & \dots & \dots & C_{1,12} \\ C_{2,1} & C_{2,2} & \dots & \dots & C_{2,12} \\ C_{3,1} & C_{3,2} & \dots & \dots & C_{3,12} \\ \dots & \dots & \dots & \dots & \dots \\ \dots & \dots & \dots & \dots & \dots \\ C_{12,1} & C_{12,2} & \dots & \dots & C_{12,12} \end{pmatrix} \quad (3.3)$$

The capacitance measurements can be normalised $\hat{C}_{a,b}$ using the parallel model, *i.e.* interpolated between the corresponding measurements for the pipe full of air $C_{a,b}^{air}$, and the pipe full

of water $C_{a,b}^{water}$:

$$\hat{C}_{a,b} = \frac{C_{a,b} - C_{a,b}^{air}}{C_{a,b}^{water} - C_{a,b}^{air}}. \quad (3.4)$$

Normalised capacitance measurements are dimensionless and very convenient for the interpretation of the capacitance matrix: an all-zeros matrix corresponds to a pipe full of air and an all-ones matrix corresponds to pipe full of water.

In order to capture dynamics of the flows, frame sequences have been recorded at an acquisition rate of 100 fps over 60 seconds, yielding $N_f=6000$ frames per experiments. The time series of normalised capacitance matrices conveniently describe the raw measurements of an ECT sensor:

$$\hat{C}_{(t)} = \{C_{(t_0)}, C_{(t_1)}, \dots, C_{(t_{N_f-1})}\}. \quad (3.5)$$

The data flow is consequent (almost a million data points per minute) and data reduction and fusion techniques are essential regardless of the method for analysis (data clustering, neural networks, etc.).

3.3.2 Time series analysis for extracting dynamical features

Each time series corresponds to $N_f=6000$ data points acquired at the acquisition frequency of the ECT system $f_{ECT}=100$ Hz for 60 s. For convenience, indices start from 0. The first step of the strategy for data reduction consists in the application of 6 statistical tools operating on each individual time series $x_{(t)} = C_{i,j(t)}$:

1. the mean operator, **mean**:

$$\mathbf{mean}(x_{(t)}) = \frac{1}{N_f} \sum_{n=0}^{N_f-1} x_{t_n} \quad (3.6)$$

2. the standard deviation operator, **SD**:

$$\mathbf{SD}(x_{(t)}) = \sqrt{\frac{1}{N_f} \sum_{n=0}^{N_f-1} \left(x_{t_n} - \frac{1}{N_f} \sum_{m=0}^{N_f-1} x_{t_m} \right)^2} \quad (3.7)$$

3. the low-pass filter with cut-off frequency $f_{c1}=5$ Hz, **LP_{5Hz}**:

$$\mathbf{LP}_{5Hz}(x_{(t)}) = \sum_{n=1}^{N_f \frac{f_{c1}}{f_{ECT}}} x_n^{DFT} \quad (3.8)$$

4. the high-pass filter with cut-off frequency $f_{c1}=5$ Hz, **HP**_{5Hz}:

$$\mathbf{HP}_{5Hz}(x(t)) = \sum_{n=1+N_f \frac{f_{c1}}{f_{ECT}}}^{N_f-1} x_n^{DFT} \quad (3.9)$$

5. the low-pass filter with cut-off frequency $f_{c2}=10$ Hz, **LP**_{10Hz}:

$$\mathbf{LP}_{10Hz}(x(t)) = \sum_{n=1}^{N_f \frac{f_{c2}}{f_{ECT}}} x_n^{DFT} \quad (3.10)$$

6. the high-pass filter with cut-off frequency $f_{c2}=10$ Hz, **HP**_{10Hz}:

$$\mathbf{HP}_{10Hz}(x(t)) = \sum_{n=1+N_f \frac{f_{c2}}{f_{ECT}}}^{N_f-1} x_n^{DFT} \quad (3.11)$$

The cut-off frequencies of the filters, f_{c1} and f_{c2} for the analysis of intermittent flows and stratified flows have been selected by empirical means based on experimental data. As a result, their values could further be tuned and generalised to other experimental set-up (different pipe diameters, phases, etc.). In this study, the emergence of waves in stratified flows and liquid bodies in intermittent flows has been associated empirically with frequency components higher than 5 Hz and 10 Hz respectively.

The analysis of the mean values is pertinent for the distinction of continuous flow, according to their geometrical features. The standard deviation yields valuable information for the recognition of intermittent flows. High-pass and low-pass filters are helpful to distinguish further flow characteristics such as bubbles or waves based on the analysis of spectral content of the varying signals. They are implemented digitally with the discrete Fourier transform of the signals. The low-pass filters discard the first element x_0^{DFT} because it corresponds to the average value of the signal and not to oscillations. As a result of these operations, we are left with 6 matrices: \mathbf{C}_{mean} , \mathbf{C}_{SD} , $\mathbf{C}_{\text{LP}_{5Hz}}$, $\mathbf{C}_{\text{HP}_{5Hz}}$, $\mathbf{C}_{\text{LP}_{10Hz}}$, $\mathbf{C}_{\text{HP}_{10Hz}}$.

3.3.3 Eigenvalues analysis for extracting geometrical features

The second step of the strategy for data reduction consists in analysing a set of eigenvalues of the matrices resulting from the data reduction procedure previously explained. A square symmetric matrix \mathbf{A} of size $N \times N$ has a set of N pairs of eigenvectors $\vec{v}_A^{(i)}$ and eigenvalues $\lambda_A^{(i)}$ satisfying:

$$\mathbf{A} \cdot \vec{v}_A^{(i)} = \lambda_A^{(i)} \vec{v}_A^{(i)}, i \in \{1, 2, \dots, N\}. \quad (3.12)$$

Let us sort the 12 eigenvalues of the matrix, from the smallest to the largest, *i.e.* in the steadily increasing order, and consider the resulting array of eigenvalues λ_A :

$$\lambda_A = \left[\lambda_A^{(1)}, \lambda_A^{(2)}, \dots, \lambda_A^{(12)} \right], \text{ with } \lambda_A^{(1)} < \lambda_A^{(2)} < \dots < \lambda_A^{(12)} \quad (3.13)$$

This original focus in our methodology has been strongly motivated by the study of Fang and Cumberbatch (2005). The authors have proposed eigenvalues as a tool in the identification of core¹, annular and stratified flows. The research was purely based on data from numerical simulations in 2D of the response of an ECT sensor with 12 electrodes. They highlight that the analysis of eigenvalues of the normalised capacitance matrix is invariant to rotation, *i.e.* the permutation of the electrodes when the capacitance matrix is formed does not influence the set of eigenvalues. The authors also explain that the multiplicity of the set of eigenvalues is correlated to the degree of symmetry. In other words, the set of eigenvalues for core and annular flows has more spread values than for stratified flows.

Even if the algorithm in our methodology differs, the analysis of the experimental measurements has confirmed the findings of Fang and Cumberbatch (2005). In Figure 3.11, the eigenvalues of \mathbf{C}_{mean} for all experiments have been compiled into a representative average for annular, stratified, intermittent and homogeneous flows, and errors bar represent the standard deviation for each set of measurement. Effectively, the set of eigenvalues with the highest multiplicity correspond to annular flows. The analysis of eigenvalues has been extended to the \mathbf{C}_{SD} matrix, which had not been done in Fang and Cumberbatch (2005). Again, a compilation of representative set of eigenvalues for each major flow regimes is shown in Figure 3.12.

The methodology proposed consists in techniques for data reduction of the time series and of the tomometric frame. Average, standard deviation and filters operate on time series to extract the essential information on the dynamical evolution of the signals. Spatial features are extracted from the tomometric frame data with eigenvalues technique proposed by Fang and Cumberbatch (2005).

¹A core flow is the reciprocal case of an annular flow: liquid flows in the centre and gas in the periphery

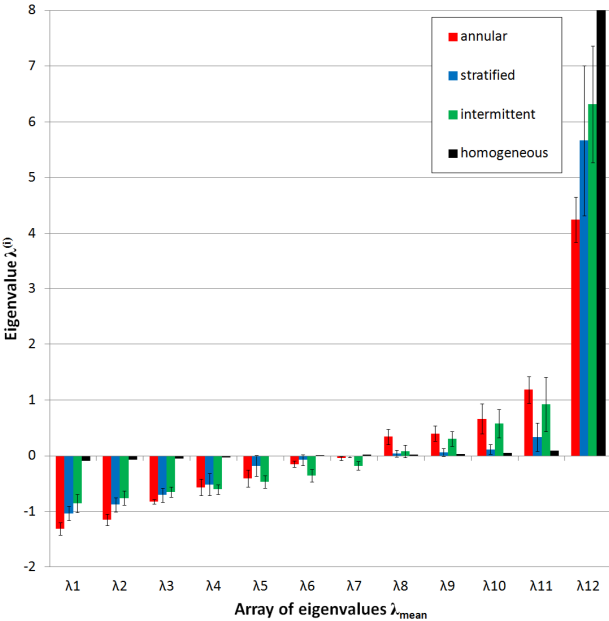


Figure 3.11: Representative arrays of 12 eigenvalues of the C_{mean} matrix for annular (in red), stratified (in blue), intermittent flows (in green) and homogeneous flow (in black), obtained by averaging over the 115 measurements in the database. Error bars indicate standard deviation in the data set

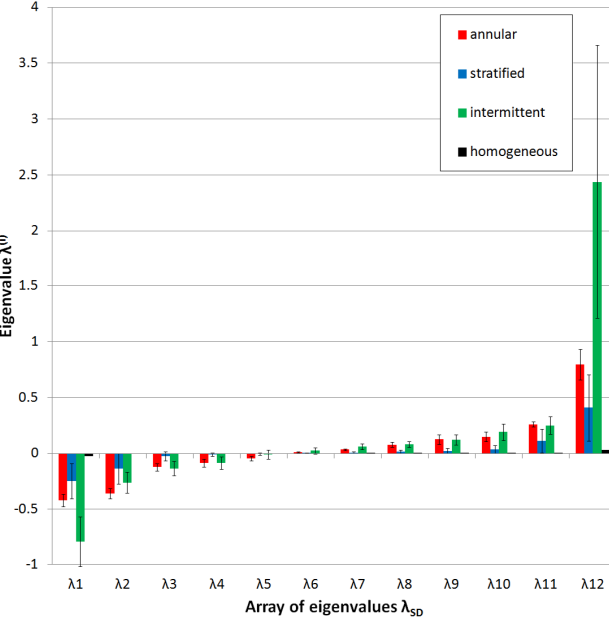


Figure 3.12: Representative arrays of 12 eigenvalues of the C_{SD} matrix for annular (in red), stratified (in blue), intermittent flows (in green) and homogeneous flow (in black), obtained by averaging over the 115 measurements in the database. Error bars indicate standard deviation in the data set

3.4 Results

Based on the principles set in the methodology, four criteria (*Criterion I*, *Criterion II*, *Criterion III* and *Criterion IV*) have been set to identify air-water horizontal flows from the raw ECT measurements. The proposed flow regime identification method consists in Boolean tests derived from the set of parameters (P_I , P_{II} , P_{III} and P_{IV}) and thresholds (T_I , T_{II} , T_{III} and T_{IV}) to select the corresponding flow regime amongst stratified smooth, stratified wavy, annular, plug and slug. The summary table of the four criteria is given in Table 3.1 and the flow diagram of identification method is shown in Figure 3.13. The performance of the method is assessed using the database of the experimental campaign at UCSN.

Criteria	Transition	Parameter P	Threshold T
<i>Criterion I</i>	Continuous/Intermittent	$P_I = \sum_{i=1}^{12} \lambda_{SD}^{(i)}$	$T_I = 0.6$
<i>Criterion II</i>	Stratified/Annular	$P_{II} = \left \frac{\lambda_{mean}^{(1)}}{\lambda_{mean}^{(1)}} \right $	$T_{II} = 0.75$
<i>Criterion III</i>	Smooth/Wavy	$P_{III} = HP_{5Hz}(\hat{C}_{a,b}(t))$	$T_{III} = 0.5$
<i>Criterion IV</i>	Plug/Slug	$P_{IV} = \frac{HP_{10Hz}(\hat{C}_{3,5}(t))}{LP_{10Hz}(\hat{C}_{3,5}(t))}$	$T_{IV} = 0.16$

Table 3.1: Summary table of the four criteria for eigenvalue based flow regime detection

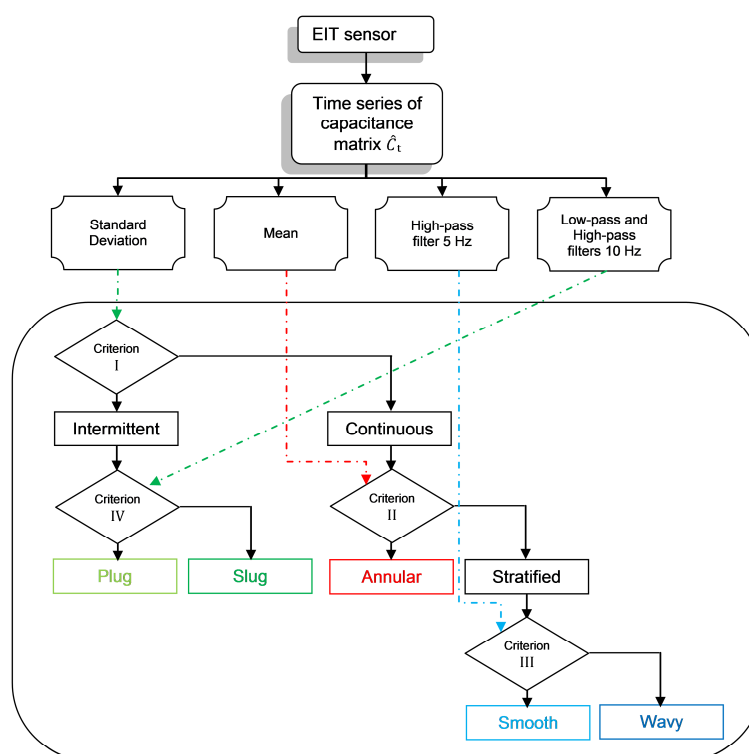


Figure 3.13: Flow diagram for regime identification method

3.4.1 Intermittent against continuous flows

The first criterion *Criterion I* aims at distinguishing intermittent flows from continuous flows based on the standard deviation of a signal associated to cross-sectional average void fraction. Given the high number of signals in tomography (66 per frame), it is less evident to select or merge all signals. The first option considered was an average over all entries. The typical arrays of eigenvalues of C_{SD} have been shown for all major categories of flow regimes in Figure 3.12. After an analysis of the database, it has been found that the parameter P_I defined as the sum of all eigenvalues $\sum_{i=1}^{12} \lambda_{SD}^{(i)}$ is a better indicator because it presents a better contrast (*i.e.* a sharp gradient at the transition zone) and the threshold is consistent for both stratified to intermittent and annular to intermittent flows. The threshold determined empirically is $T_I = 0.6$. The indicator for *Criterion I* satisfies the Boolean condition: 'is $P_I > T_I$ '?

The results (parameter and indicator) are displayed in Figure 3.14, and the colour mapping makes it intelligible that the shapes of the transition regions are preserved as compared to the map by Mandhane et al. (1974).

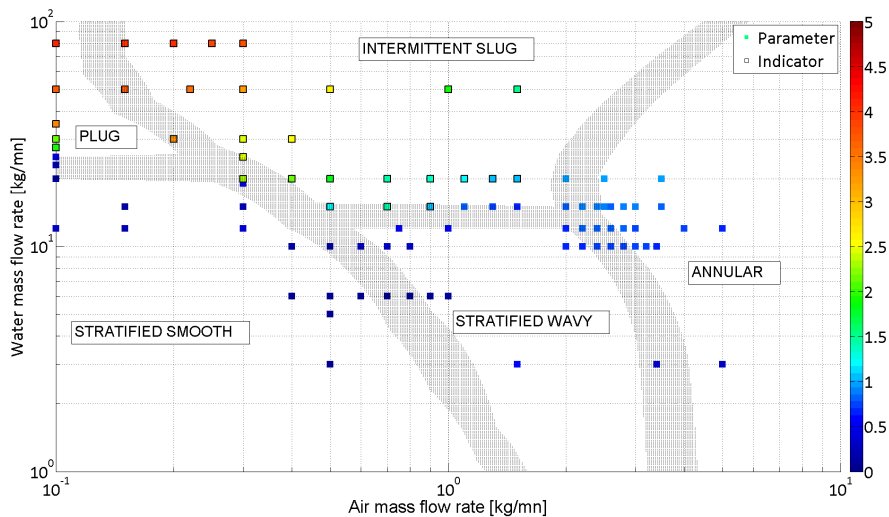


Figure 3.14: Parameter and indicator for *Criterion I*, on flow regime map

3.4.2 Annular against stratified flows

Criterion II distinguishes an annular flow from a stratified flow, based on the λ_{mean} array. The analysis of the mean value of time series is pertinent for consideration of continuous flows. The typical arrays of eigenvalues λ_{mean} have been shown for all major categories of flow regimes in Figure 3.12. The parameter selected P_{II} is the absolute value of the ratio of the second largest with the smallest $\frac{\lambda_{mean}^{(11)}}{\lambda_{mean}^{(1)}}$. This is slightly different than the criterion retained by Fang and Cumberbatch (2005): $\frac{\lambda_{mean}^{(11)}}{\lambda_{mean}^{(10)}}$. Even if the parameter P_{II} has been slightly changed, this study brings experimental evidence of the claim by Fang and Cumberbatch (2005) that the

deviation from stratified flows toward annular flows is correlated with the loss of multiplicity of the eigenvalues. Despite the gradualness of this transition, the boundary was defined as the complete wetting of the pipe walls. As a result, the threshold T_{II} was set at 0.75. The indicator for *Criterion II* satisfies the Boolean condition: 'is $P_{II} > T_{II}$ '?

The results (parameter and indicator) are displayed in Figure 3.15, and the colour mapping makes it intelligible that the shapes of the transition regions are preserved as compared to the map by Mandhane et al. (1974). With a regular coverage of the map, contour lines of parameters could be displayed and compared more rigorously. The results also show that intermittent flows tend to be assimilated to annular flows with *Criterion II* alone. This is expected because the time-average void fraction profile of intermittent flows present the features of annular flows: there is a permanent liquid bulk at the bottom of the pipe, an alternating presence of liquid bodies at the upper part, and a liquid film on the pipe that decays in the time between two liquid bodies.

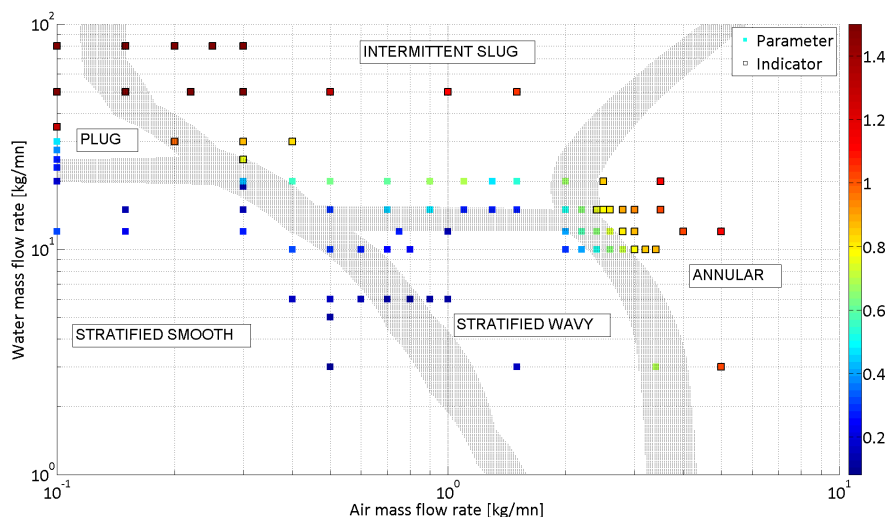


Figure 3.15: Parameter and indicator for *Criterion II*, on flow regime map

3.4.3 Stratified smooth against wavy flows

Criterion III distinguishes stratified smooth and stratified wavy flows. The oscillations of the gas-liquid interface of stratified flows created by waves have low amplitude but the spectral signatures of the signals differ noticeably. Increasing the air flow rate results firstly in the appearance of coherent waves (Figure 3.10b) having a wavelength of the order of the pipe diameter and a low frequency (4-10 Hz), and then higher frequency waves (Figure 3.10c). The capacitance measurements most sensitive to changes in the interface level are selected as the maximum entry (a_{max}, b_{max}) of the \mathbf{C}_{SD} matrix. The parameter P_{III} is obtained by applying the high pass filter with cut-off frequency of 5 Hz on the time series $\hat{C}_{a_{max}, b_{max}, (t)}$:

$$P_{III} = \mathbf{HP}_{5\text{Hz}}(\hat{C}_{a_{max}, b_{max}, (t)}) \quad (3.14)$$

The cut-off frequency has been set empirically at 5 Hz based on analysis of experimental data. The measurements involving an electrode close to the interface between air and water are the most sensitive to variations caused by emergence of waves in stratified flows. In Figure 3.16, the spectra of one particular normalised capacitance measurement $\hat{C}_{12,12}$ is shown for 3 different experiments. The magnitude of the DFT is plotted in log scale. The emergence of waves in stratified flows is associated with an increase of the high frequency components in the signal.

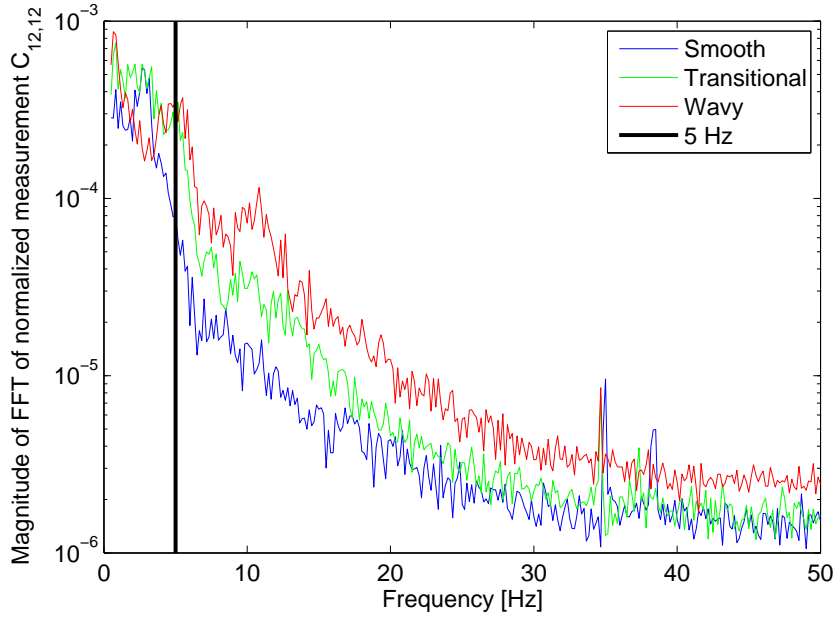


Figure 3.16: Spectra of normalised capacitance measurement $\hat{C}_{12,12}$ in 3 experiments: stratified smooth (blue), transitional (green) and stratified wavy (red) flows. The 5 Hz cut-off frequency empirically set is indicated in black

It is important to understand why filtering out low frequency components of the signal improves the recognition. Instabilities caused by the water pumps or air supply may generate slow variations in the water fill level. This low frequency signal can potentially have a high amplitude scrambling the information of signal oscillations. The adjacent measurements $\hat{C}_{i,i+1}$ have a relatively small sensing zone near the boundary. If the water level varies sufficiently in a measurement session to cover another electrode, the variation of some measurements can be dominantly caused by instabilities of the flow rig, as is illustrated in Figure 3.17. In experiments, measurements of low frequency intermittent flows were specifically subject to these instabilities because after the occurrence of a slug or plug, the pipe would slowly fill to the equilibrium level. The signal of the γ -ray densitometer for such a flow is shown in Figure 3.18.

The current version of this criterion does not requires to compute all elements of the $\mathbf{C}_{HP_{5Hz}}$ matrix, just the one selected from the \mathbf{C}_{SD} matrix. The parameter P_{III} reflects the level of waviness of the flow. The threshold T_{III} has been set at 0.5. The indicator for *Criterion III*

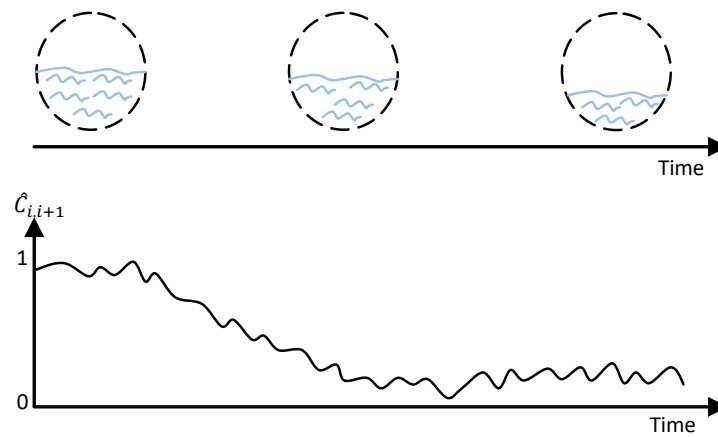
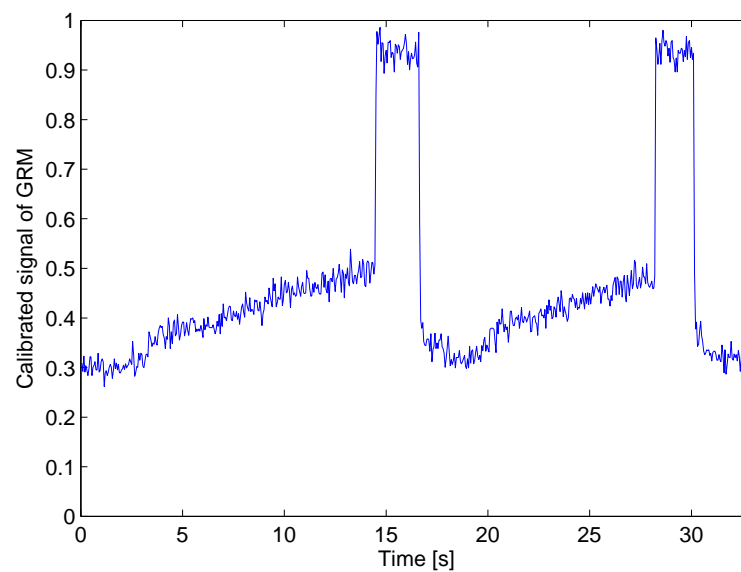


Figure 3.17: Illustrative example of slow instabilities

Figure 3.18: Signal of the γ -ray densitometer for low frequency intermittent flow

satisfies the Boolean condition: 'is $P_{III} > T_{III}$?. The results (parameter and indicator) are displayed in Figure 3.19.

3.4.4 Plug against slug flows

Criterion IV distinguishes plug from slug flows. The liquid bodies of these two flow regimes differ mainly by the aerodynamic shape of the interface and the massive presence of entrained air bubbles in the liquid slug body (see Figures 3.10e and 3.10f). Researchers have suggested

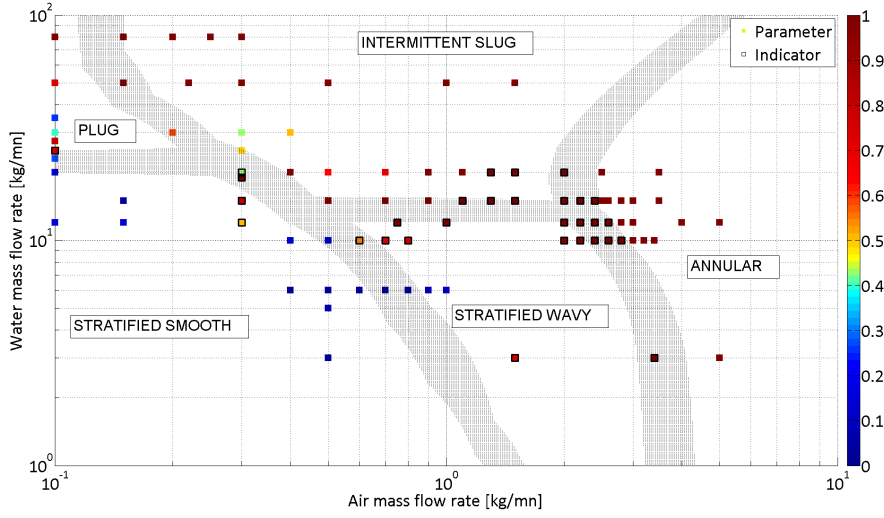


Figure 3.19: Parameter and indicator for *Criterion III*, on flow regime map

they differ by the slug (or plug) frequency, *i.e.* the frequency of occurrence of liquid bodies (Karki, 2016). However, our experiments have shown some exceptions at the boundary zone between layered and intermittent flows. Moreover, such criterion is restrictive in its application domain, requiring a sufficiently large number of liquid bodies to be captured, and likely requiring a threshold that will depend on the pipe configuration. In this paper, we have opted for the consideration of a mechanistic model of slug and plug flows, and aimed at extracting the information of the entrained bubbles. For a slug flow, additional to the signal of an intermittent flow, the swarm of small bubbles at the top of the pipe will generate extra high frequency components in the spectrum of signals sensitive to this sensing zone. In our set-up, the capacitance measurement between electrodes n°3 and n°5, $\hat{C}_{3,5}(t)$, experience an increase in the relative importance of high frequencies for slug flows.

For *Criterion IV*, the cut-off frequency of the high and low pass filters is set at 10 Hz and the resulting parameter is:

$$P_{IV} = \frac{\text{HP}_{10\text{Hz}}(\hat{C}_{3,5}(t))}{\text{LP}_{10\text{Hz}}(\hat{C}_{3,5}(t))} \quad (3.15)$$

The 10 Hz cut-off frequency has been set empirically based on analysis of experimental data. It largely exceeds the maximum occurrence frequency of intermittent flows (3 Hz) observed in our database. The measurements involving electrodes near the top of the wall are particularly sensitive to the presence of air bubble at the top of the pipe. In Figure 3.20, the spectra of one particular normalised capacitance measurement $\hat{C}_{3,5}$ is shown for 3 different experiments. The magnitude of the DFT is plotted in log scale. The importance of high frequencies in slug flows (relative to the total standard deviation) is associated to the swarm of small bubbles at the top of the pipe.

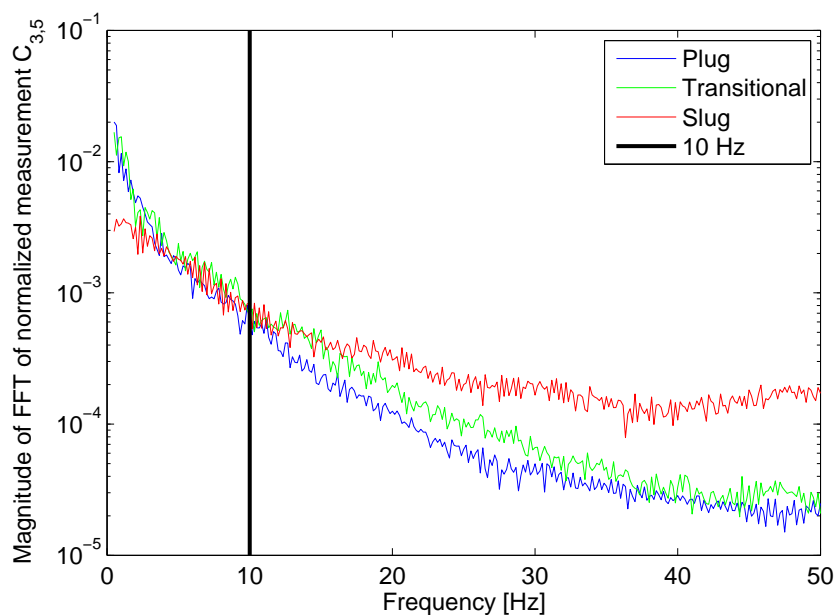


Figure 3.20: Spectra of normalised capacitance measurement $\hat{C}_{3,5}$ in 3 experiments: plug (blue), transitional (green) and slug (red) flows. The 10 Hz cut-off frequency empirically set is indicated in black

The threshold T_{IV} has been set at 0.30. Note that the value of this ratio for static and continuous flows is expected to be exceeding 1.0 because this capacitance measurement is essentially not varying so the spectrum is dominated by noise: it would be 4.0 for white noise (since the bandwidth of the high-pass filtered signal is 4 times that of the low-pass filtered signal). The indicator for *Criterion IV* satisfies the Boolean condition: 'is $P_{IV} > T_{IV}$?'. The results (parameter and indicator) are displayed in Figure 3.21. It is remarkable that the identification is still reliable for measurements of transition flows capturing only one liquid body. Note that when a collection of liquid bodies is captured, the frequency of the intermittent flow may be reliably determined as corresponding to the maximum of the Fourier spectrum of capacitance measurements with large standard deviation, or alternatively by fitting typical functions (e.g. Gaussian) on the spectrum. Since the orientation of the pipe was known in our experiments, and since the bubble swarm in a slug flow is expected at the top of the pipe, the adequate measurement was selected. For a general formulation of the *Criterion IV*, the preliminary task will be to detect the orientation of the pipe looking for a symmetry axis.

Based on the condensed information after data reduction, four criteria have been found to discriminate flow regimes. The performance test with the benchmark data suggests a good performance of the methodology.

Chapter 3. Flow regime identification

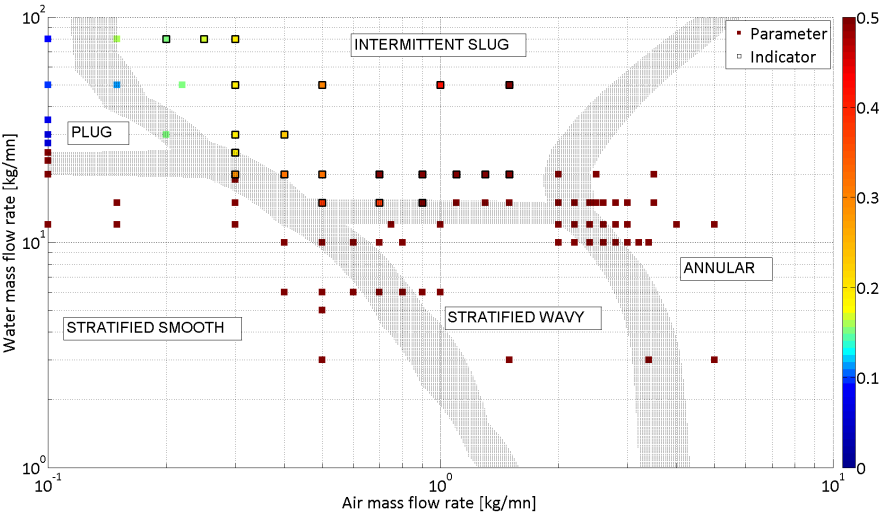


Figure 3.21: Parameter and indicator for *Criterion IV*, on flow regime map

3.5 Extended methodology with simulations

A numerical model of the ECT sensor and the study volume has been set with *Finite Element Method Magnetics* (FEMM) solver for Maxwell's equations for two-dimensional electromagnetic problems. Simulations of continuous flows have supported the validation of *Criterion II* derived in previous Section 3.4.2. Curves for the estimation of the cross-sectional phase fraction have been generated numerically for idealised stratified and annular flows. The plans for ongoing project to implement similar methodology for the ProME-T EIT sensor will be unveiled.

3.5.1 Numerical model and simulations

In order to increase the confidence in the proposed methodology and for extending it to different case scenarios, a numerical model of the sensor and the test section has been developed. It has been considered out of the scope of the research to extend the simulations to intermittent flows since it would require fluid dynamics solvers. The FEMM software (Meeker, 2015) has been used to run the numerical simulations. Its graphical user interface, automatic mesh generation module and interface with Matlab provides a very convenient framework for fast excitation of the signal response of the ECT sensor to a phase distribution sketched by the user. A screenshot of the user interface in the case of the study of a stratified flow is shown in Figure 3.22.

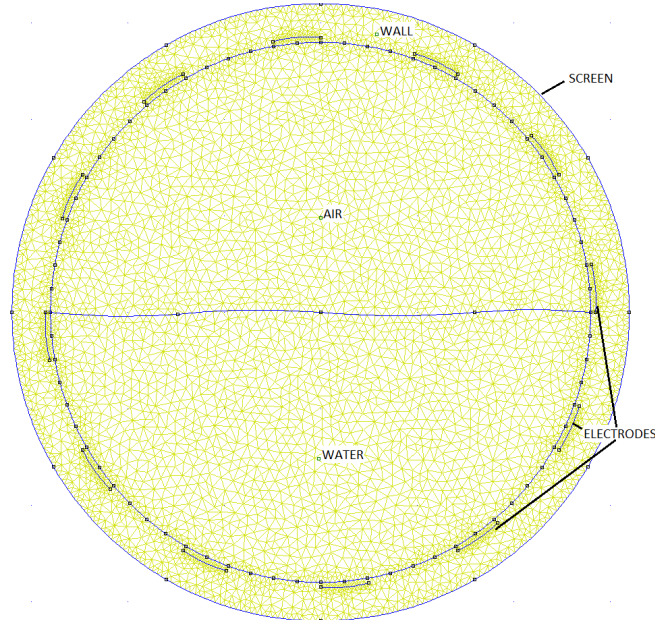


Figure 3.22: 2D FEMM model of the ECT sensor, and mesh, illustrated for example of wavy flow

FEMM solves the forward problem (see Equation (2.8)) in 2D with the finite elements methods. The finite element problem is expressed using the variational formulation, with first-order

triangle elements. The solver of the current flow (harmonic) problem is based on the complex symmetric Bi-Conjugate Gradient method. The automatic mesh generator implemented in the software is non-adaptive and provides Delaunay triangulation. More details can be found in the reference manual of the software (Meeker, 2015). The ECT sensor (described previously in Section 3.2.2) has been modelled in FEMM as a disk of diameter 56 mm containing water ($\sigma^{water} = 0.2 \text{ S} \cdot \text{m}^{-1}, \epsilon_r^{water} = 80$) and air ($\sigma^{water} = 0 \text{ S} \cdot \text{m}^{-1}, \epsilon_r^{water} = 1$) materials, a pipe wall made of dielectric material ($\sigma^{water} = 0 \text{ S} \cdot \text{m}^{-1}, \epsilon_r^{water} = 2.5$), a set of 12 electrodes and a screen. A zero potential boundary condition is set at the electrodes and at the screen, which are modelled as conductors in the shape of arc segments. For each simulation of the sensor response, the interfaces between water and air phase are sketched via the graphical user interface and the material properties are set in each zone (as water or air) within the test section. The automatic mesh generator is ran, a check is made of the number of elements (over 5000 elements in all simulations), and the file is saved. A Matlab script has been developed, that selects an excitation electrode, sets its electrical potential to 1 by changing the boundary condition, runs the simulation and records the electrical charges on each conductor (*i.e.* each electrode). All electrodes are sequentially activated, and the normalised capacitance matrix is computed. The reference matrices used for the normalisation (*i.e.* corresponding to empty and full pipes) are stored in the simulation folder.

3.5.2 Numerical validation of the criteria

Five test cases have been analysed in the numerical study aiming at comparing the arrays of eigenvalues obtained from experimental measurements to the ECT sensor response numerically simulated:

- (a) homogeneous water flow
- (b) stratified smooth flow
- (c) combination of stratified and annular flow (simplified representation of horizontal flow)
- (d) another vertical annular flow, with thicker film
- (e) centred annular flow (representative of vertical flow)

The numerical FEMM models, the normalised capacitance matrix and the array of eigenvalues for these 5 test cases are shown in Figure 3.2. The Criterion II applied to the eigenvalues array from numerical simulations successfully identifies (b) as stratified and (c), (d) and (e) as annular flows. Note that for the homogeneous water flow (b), P_{II} cannot be computed because there is a singularity.

3.5. Extended methodology with simulations

Numerical 2D model	Capacitance matrix	Array of eigenvalues

Table 3.2: Numerical FEMM models, normalised capacitance matrices and arrays of eigenvalues, for each simulation of case study

3.5.3 Estimation of phase fractions

Stratified flows

The determination of the flow regime with the FRI methodology brings perspectives to assess parameters of interest specific to a given flow regime (*e.g.* water level for stratified flows, slug frequency for slug flows, etc.). For all flow regimes, the cross-sectional averaged fraction of each phase is an essential information to obtain. The problem faced with the measurements from the experimental database is that no reliable measurement of the cross-sectional averaged water fraction (WF) was available. Numerical simulations have been used instead to constitute a set of array of eigenvalues for stratified flows at different water fill levels, which is shown in Figure 3.23.

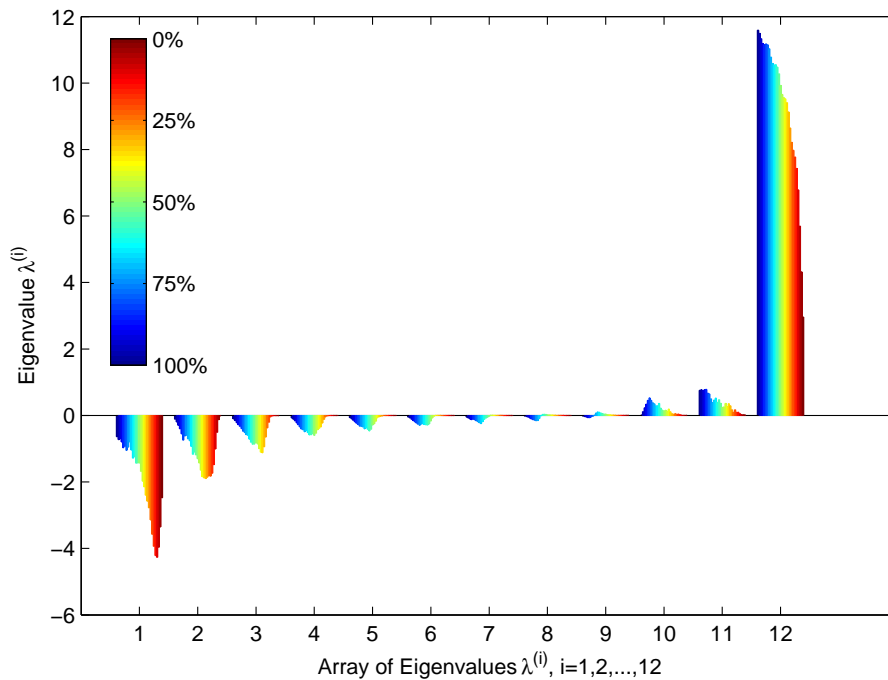


Figure 3.23: Array of 12 eigenvalues λ_{mean} for stratified flows with various water fill levels

Though the first interpretation being tested was that the leading eigenvalue $\lambda^{(12)}$ is strongly related to the water fraction (*i.e.* there is a monotonic relationship), a finer analysis has shown that the function of the sum of all 12 eigenvalues, $\sum_{i=1}^{12} \lambda^{(i)}$, is more reliable. In other words, because the relationship is closer to a linear function, it gives a better sensitivity over the full range of water fractions. In order to get a better insight in the sensor response, we have compared two models of sensor: *Sensor I* with large aperture electrodes (the aperture angle being 22.3° and separation angle being 30°) and *Sensor II* considering electrodes with smaller aperture angle 10° . The dimensions of *Sensor I* correspond to the dimensions of the real ECT system used in experiments. For each sensor model, the relationship between the sum of the 12 eigenvalues, $\sum_{i=1}^{12} \lambda^{(i)}$, and the water fraction WF is shown in Figure 3.24. The curve for *Sensor II* is not as regular as for *Sensor I* because essential information is missing for the

estimation of the water level between the electrodes. A very good fit of the relationship is obtained with a 3rd order polynomial and is also shown in the figure.

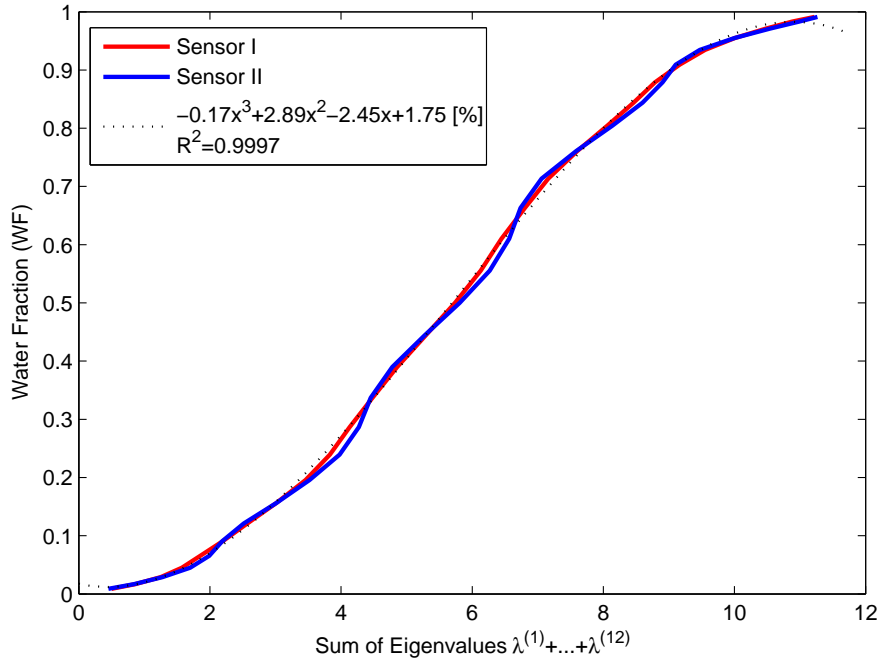


Figure 3.24: Relationship between the cross-sectional averaged water fraction (WF) and the sum of eigenvalues $\sum_{i=1}^{12} \lambda^{(i)}$, for stratified flows

The derivative of the 3rd order polynomial fit function is shown in Figure 3.25 for *Sensor I*. It represents the sensitivity of the water fraction estimate to errors in the determination of the sum of all 12 eigenvalues, which are unavoidable with experimental measurements. As expected, it is larger when the pipe is approximately half-filled because the measurements (especially capacitance values between adjacent electrodes) are sensitive to water level rather than water fraction.

Annular flows

A similar study has been performed with a set of simulations of centred annular flows with varying film thickness. Interestingly, it was found that the leading eigenvalue $\lambda^{(12)}$ is a better estimator of the water fraction. The relationship is shown in Figure 3.26 for *Sensor I* and *Sensor II*, with a good 2nd order polynomial fit. The results indicate significantly different response depending on the electrode aperture angle.

3.5.4 Adaptation to ProME-T EIT sensor

The methodology developed for the ECT sensor at UCSN is under test and adaptation for the ProME-T EIT sensor and vertical flows. At this stage, the sensor has never been connected to a

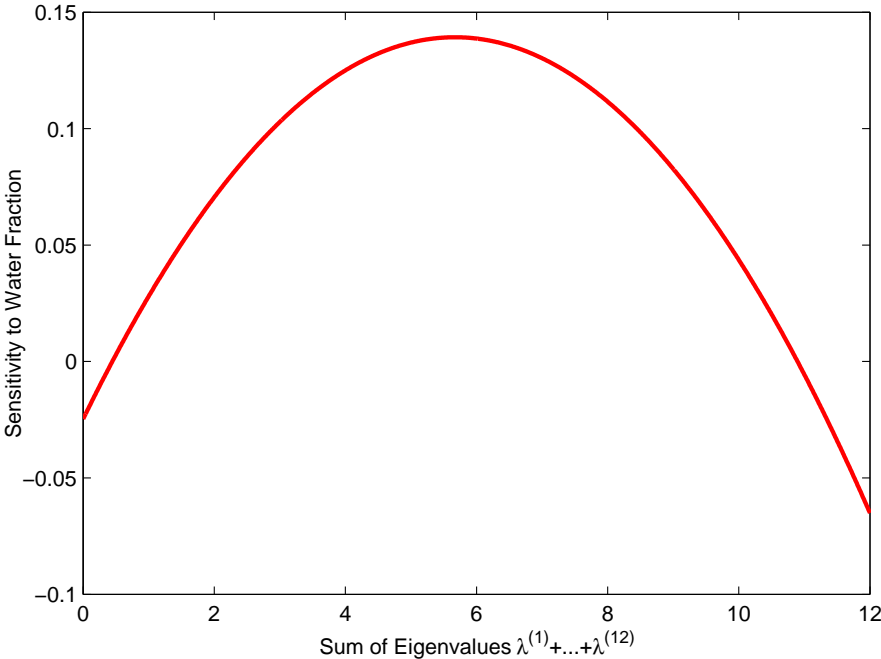


Figure 3.25: Sensitivity of the estimate for cross-sectional averaged water fraction (WF) to the sum of eigenvalues $\sum_{i=1}^{12} \lambda^{(i)}$

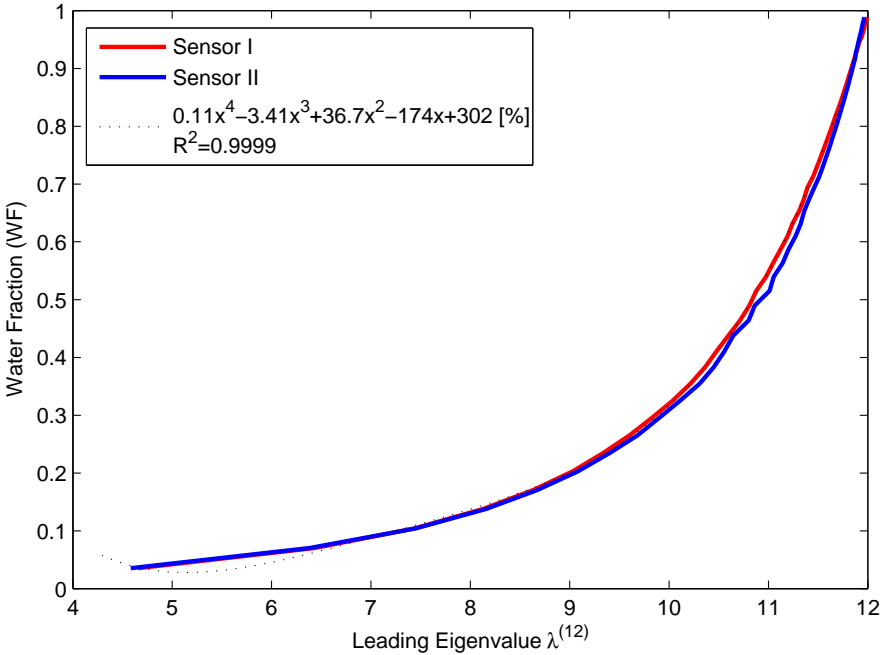


Figure 3.26: Relationship between the cross-sectional averaged water fraction (WF) and the leading eigenvalue $\lambda^{(12)}$, for annular centred flows

3.5. Extended methodology with simulations

multiphase flow rig for dynamical tests. However, the methodology of the eigenvalue analysis has been adapted to EIT measurement data. The parameter analogue to the capacitance measurements in ECT is the inverse of the bulk impedance given by Equation (2.22), *i.e.* the conductance: $G = \frac{1}{Z_{bulk}}$. The measurements are normalised with the reference data for the homogeneous water medium: $\hat{G} = \frac{G}{G_{wat}}$. The 120 measurements in a frame are arranged into the normalised conductance matrix \mathbf{G} . The diagonal terms are computed as follows:

$$G_{i,i} = - \sum_{j \neq i} G_{i,j}. \quad (3.16)$$

The 16 eigenvalues of the conductance matrix \mathbf{G} are sorted from the minimum to the maximum into the array of eigenvalue λ .

Eleven experiments representative of annular flow conditions have been performed with water fraction ranging from 48% up to 97%. The two extreme experiments in terms of water fraction are shown in Figure 3.27. The resulting array of eigenvalues are shown in Figure 3.28. The leading eigenvalue $\lambda^{(16)}$ is very close to 16 in all the measurements of high water fraction. This eigenvalue is not shown in Figure 3.28 for the sake of clarity. The results clearly show a monotonic relationship between the eigenvalues and the cross-sectional average water fraction.

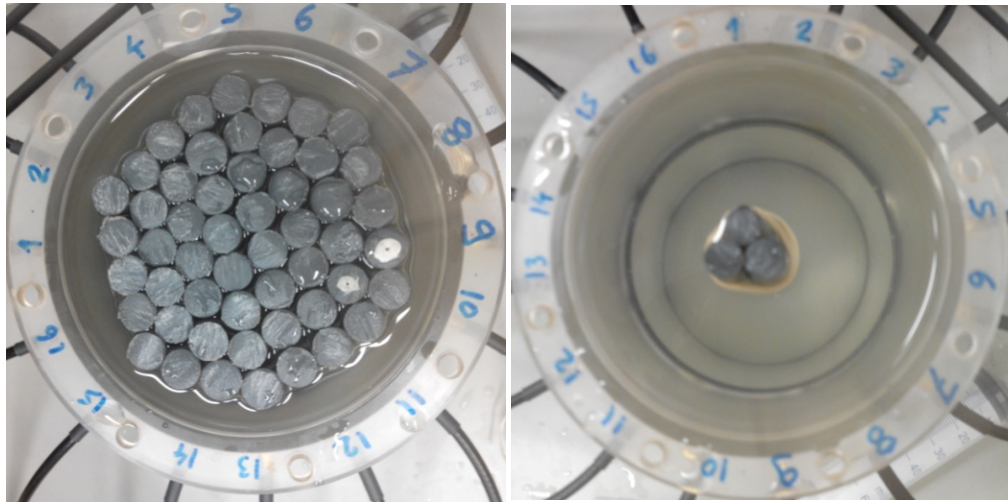


Figure 3.27: Pictures of the two extreme experiments in terms of WF: 48% (left) and 97% (right)

In consequence of the higher importance of the leading eigenvalue in the case of EIT measurements, we have chosen to select another parameter for estimation of water fraction: $\sum_{i=1}^{15} |\lambda^{(i)}|$. This parameter is plotted against the water fraction in Figure 3.29. As expected, the sensitivity is higher for high water fractions, and the estimation will be less reliable. However, typical annular flows have thin liquid films and present the most favourable scenario for estimation of water fraction with EIT.

An ongoing project consists in adapting the method developed in this study to the ProME-T

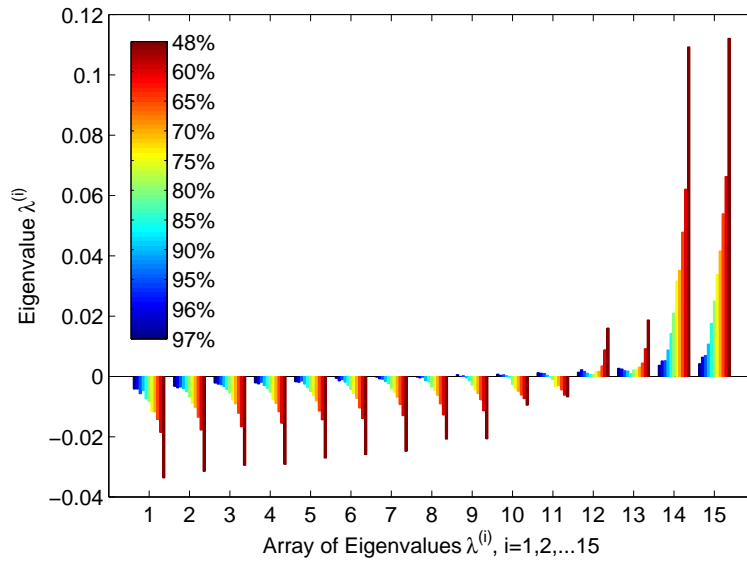


Figure 3.28: 15 first elements of the array of eigenvalues λ for annular flows with different water fraction

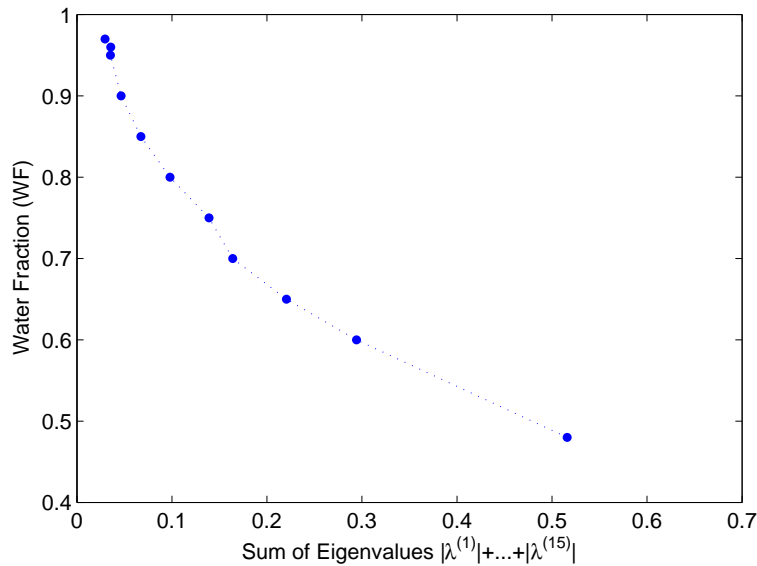


Figure 3.29: Relationship between the cross-sectional averaged water fraction (WF) and the sum of the 15 eigenvalues $\sum_{i=1}^{15} |\lambda^{(i)}|$, for annular centred flows

EIT sensor and a different flow rig at the Laboratory of Hydromechanics of Core and Circuits at CEA Cadarache. A two-phase flow rig with a long vertical test section is being upgraded. The pipe inner diameter will be 51 mm, similar to McQuillan and Whalley (1985) and Zhou (2013). As a result, flow regime maps from independent studies will be available for comparison. In vertical air-water flows, there are 4 main regimes: slug, churn, annular and bubbles. Given the characteristics of the pumps and air supply, it is expected that all four will be available.

3.5. Extended methodology with simulations

Another test section has been designed and is being commissioned. A CAD schematic is shown in Figure 3.30. It has two configurations, with square electrodes ($5 \times 5 \text{ mm}^2$) or with long electrodes ($5 \times 150 \text{ mm}^2$) as in the ECT design. This flexibility will allow to analyse and compare the performance of the point-like electrode concept for dynamical studies of flows. It is expected that high frequency content that can be associated to presence of bubbles swarm will have a higher relative importance. The frame acquisition rate in ProME-T can be available at up to 830 fps, which will bring new perspectives for the measurements of fast-evolving flows. Also, a better resolution typical of EIT sensors is expected in the new set-up, in particular due to the increased number of electrodes (from 12 to 16). The design of the new test section will be less sensitive to errors in electrode positioning. The electrodes in the new test section will be adjusted with a better tolerance.

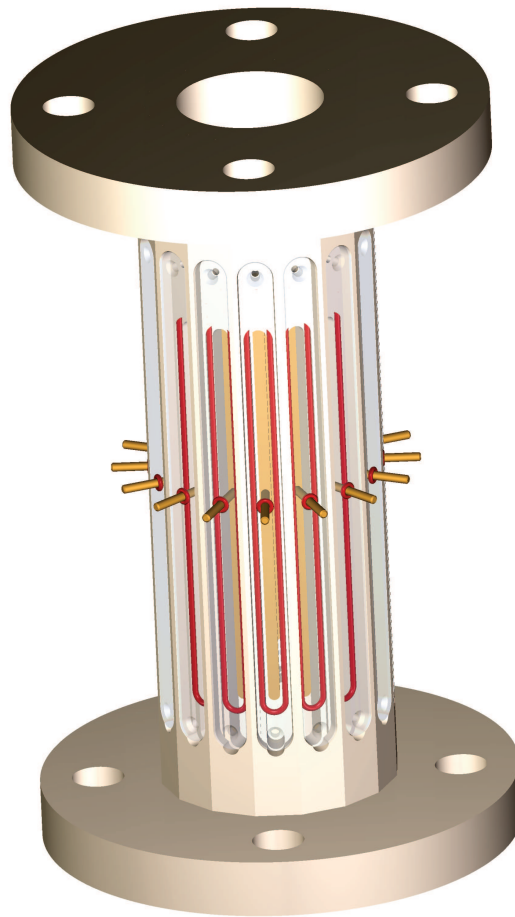


Figure 3.30: CAD schematic of the new EIT sensor array and test section: 16 electrodes in yellow/orange, seals in red, test section made of PMMA in gray. Connections to the EIT modules are not shown.

Chapter 3. Flow regime identification

The criteria of the methodology for flow regime identification have been derived based on analysis of experimental data. Numerical simulations confirm the results for the response of the sensor numerical model. A set of simulations of stratified and centred annular flows illustrates a procedure to estimate the cross-sectional average phase fraction out of the array of eigenvalues. Ongoing project aims at adapting the methodology to the EIT sensor and vertical flows.

4 Imaging

The ProME-T prototype sensor developed in the frame of the Ph.D. thesis can provide the user data frames at a high acquisition rate. The image reconstruction problem in electrical tomography consists in inverting the forward problem relating electrical properties within the study volume to the resulting measurement data for a given excitation. Acknowledging the diversity of techniques proposed for image reconstruction electrical tomography, an effort has been made to implement an algorithm adapted for the target of the Ph.D. thesis. An overview of the variety of image reconstruction techniques in the scientific literature is given. The image reconstruction methodology developed within the framework of the thesis will be explained and motivated. Reconstruction images from real experimental data will be shown and their quality will be assessed using objective parameters.

4.1 Overview of EIT image reconstruction

The mathematical formulation of the forward problem, that describes the system response to any excitation for a known distribution of electrical properties, $\sigma = \sigma(x)$ and $\epsilon = \epsilon(x)$ within the study volume $x \in \Omega$, has been given in Section 2.2.1. The profiles of the excitation current and voltage response on the boundary of the study volume, $J|_{\partial\Omega}$ and $V|_{\partial\Omega}$, are respectively called the Neumann and Dirichlet boundary condition. A *projection* is a set of excitation and response for a particular medium configuration: $(V|_{\partial\Omega}, J|_{\partial\Omega})$. The mathematical operator relating $V|_{\partial\Omega}$ to $J|_{\partial\Omega}$ is called the Neumann-to-Dirichlet map. In its continuous form, the inverse problem for imaging consists in finding a distribution of electrical properties fitting a Neumann-to-Dirichlet map. It has been mathematically defined by Calderón (2006), and the author has shown a unique solution exists. Because the inverse problem for electrical tomography is non-linear and ill-posed, a plethora of numerical algorithms have been proposed to propose reliable solutions in practice. Indeed, it is unavoidable that measurement input data is noisy and that additional noise will be introduced by the numerical algorithm. The scientific literature in this domain is abundant, because there is no consensus on which method is best, depending on specificity of each application and on the trade-off between computational burden and image quality. Researchers early recognised this challenge to be the most serious

lock-in effect in the development of EIT (Peytraud, 1995; Lemonnier and Peytraud, 1998; Kotre, 1993; Yorkey et al., 1987). A comprehensive topical review can be found in Borcea (2002).

Low-frequency electrical currents are soft-fields (Bates, 1984), therefore the EIT inverse problem is non-linear. In other words, the sensitivity profile for a given projection depends on the conductivity of the study volume to be imaged. This paradoxical property brings considerable challenge in imaging. An *a priori* solution needs to be postulated to compute an approximation of the sensitivity profile and propose a solution to the linearised problem. Iterative algorithms will use the solution as the next candidate for *a priori* solution. If a correct *a priori* solution is not available by another mean, high contrast images (typically the case of high resolution imaging of gas-liquid flows) are particularly challenging. Furthermore, the EIT inverse problem is ill-posed: the matrices to be inverted are typically very badly conditioned. In other words, a small error in the input voltage measurements fed to the algorithm will result in a large error in the reconstructed image. In order to decrease the ill-conditioning and provide an immunity to measurement noise, the EIT inverse problem can be modified via regularisation techniques. The problem to be inverted is modified with a so-called prior function.

4.1.1 Inverse problem

Let V_{mea} be the vector containing the set of voltages measured and $V_{sim}(\rho)$ be the vector containing the set of voltages simulated for a given electrical resistivity distribution $\rho = \frac{1}{\sigma}$ within the domain. Reconstructing resistivity is preferable to reconstructing conductivity because the relation with the voltage measurements is linear (Yorkey et al., 1987). When the domain has been subdivided into N_{mesh} mesh cells for the numerical simulation, we consider ρ as a vector of length N_{mesh} .

Linear back projection

Linear back projection (LBP) methods are non-iterative techniques that project the voltage variations ΔV onto the maps of resistivity change $\Delta\rho$ with a set of sensitivity coefficients S calculated with a linearised version of the inverse problem (about input data V^0 and *a priori* solution ρ^0) (Kotre, 1993):

$$\Delta\rho = S \cdot \Delta V \tag{4.1}$$

The sensitivity matrix may be computed using the perturbation method, *i.e.* from a reference simulation, and N_{mesh} perturbed simulation with resistivity changed in each pixel. This method is very slow, but once the sensitivity matrix has been stored, the image reconstruction can be implemented online. The sensitivity coefficients are computed as the pixel-average of the "dot product of lead fields of current injection \bar{J}_m and voltage measurements \bar{J}_n " (Kauppinen et al., 2006; Kotre, 1993). With this method, a single forward calculation is required (but lead

fields need to be computed):

$$S_{m,n,p} = \int_{x \in p} \frac{1}{\sigma(x)} \bar{J}_m(x) \cdot \bar{J}_n(x) \quad (4.2)$$

with m the index of the current injection lead field, n the index of the voltage measurement lead field, and p the index of the pixel.

As a consequence of the linearisation, the LBP images are approximation and suitable to imaging media with small conductivity gradients. Filtered LBP algorithms reduce the blurring of resulting images by deconvolution with a point spread function (Kotre, 1994). It is also possible to segment it to recover the phase distribution using the estimation of the cross-sectional average phase fraction (Xie et al., 1989a).

Least-square iterative methods

This overview of the non-linear inversion methods is greatly inspired by intelligible introductory sections in Yorkey et al. (1987) and in Kim et al. (2001). Least-square iterative methods consider an objective function $\phi(\rho)$ to be minimised:

$$\phi(\rho) = \frac{1}{2} [V_{mea} - V_{sim}(\rho)]^T [V_{mea} - V_{sim}(\rho)] \quad (4.3)$$

with $V_{sim}(\rho)$ the boundary voltage simulated for the candidate solution ρ . In order to minimise it, Newton-Raphson methods set the derivative of the objective function to zero:

$$\phi'(\rho) = -[V'_{sim}]^T [V_{mea} - V_{sim}] = 0 \quad (4.4)$$

The first order derivative of V_{sim} with respect to ρ , V'_{sim} , is frequently called the Jacobian matrix *Jac*:

$$Jac = [V'_{sim}]_{i,j} = \frac{\partial V_{sim,i}}{\partial \rho_j} \quad (4.5)$$

At each iteration, starting from a suggested image ρ^k , the value of the objective function for the next image ρ^{k+1} according to the Newton-Raphson method will be:

$$\phi'(\rho^{k+1}) = \phi'(\rho^k) + \phi''(\rho^k)(\rho^{k+1} - \rho^k) = 0 \quad (4.6)$$

The second order derivative of the objective function, the so-called Hessian matrix, can be calculated from Equation (4.3):

$$\phi'' = [V'_{sim}]^T V'_{sim} - [V''_{sim}]^T \{I \otimes [V_{mea} - V_{sim}]\} \quad (4.7)$$

Neglecting the second term of the Hessian matrix in Equation (4.7) prevents the computationally expensive calculation of the second order derivative of $V_{sim}(\rho)$, resulting in the

Gauss-Newton method (also referred to as *modified Newton-Raphson*):

$$\phi'' = [V'_{sim}]^T V'_{sim} = Jac^T Jac \quad (4.8)$$

Finally, one gets at each iteration an update of the resistivity vector ρ^{k+1} :

$$\rho^{k+1} = \rho^k + (Jac^T Jac)^{-1} \left[Jac^T \{V_{mea} - V_{sim}(\rho^k)\} \right] \quad (4.9)$$

4.1.2 Regularisation

The Hessian matrix $Jac^T Jac$ that is inverted in Newton's methods are ill-conditioned, which degrades the performance of the image reconstruction algorithm. The regularisation consists in adding a penalty term to the objective function:

$$\phi(\rho) = \frac{1}{2} [V_{mea} - V_{sim}(\rho)]^T [V_{mea} - V_{sim}(\rho)] + \frac{1}{2} \lambda_{reg} P_{reg}(\rho) \quad (4.10)$$

This additional arbitrary function of the internal conductivity distribution $P_{reg}(\rho)$ is chosen so to mitigate the ill-posedness of the reconstruction. A regularisation parameter λ_{reg} is set to adjust the importance of the regularisation. A highly regularised problem would result in loss of fidelity to the original problem. There are numerous regularisation techniques in the literature, developed for medical imaging or other research applications (Cohen-Bacrie et al., 1997; Kim et al., 2001; Tanushev and Vese, 2007; Yang et al., 1999; Borcea et al., 2003). The challenge of imaging two-phase flows consists of dealing with high gradients of conductivity. Kim et al. (2001) have examined the Levenberg-Marquardt, implicitly scale Levenberg-Marquardt and first-order difference regularisation methods, respectively corresponding to penalty terms in the form of Equations (4.11), (4.12), (4.13):

$$P_{reg}(\rho) = \|\rho\|, \quad (4.11)$$

$$P_{reg}(\rho) = \rho^T \cdot \text{diag}(Jac^T Jac) \cdot \rho, \quad (4.12)$$

$$P_{reg}(\rho) = \|\nabla \rho\|. \quad (4.13)$$

As a result, the authors have concluded that implicitly scaled Levenberg-Marquardt and first order difference techniques perform considerably better than Levenberg method when the image presents high resistivity contrast. There are many classic regularisation techniques summarised in Table 4.1: Tikhonov, NOSER (Cheney et al., 1990), Laplace, Landweber (Yang et al., 1999).

In most cases, the regularisation term can be interpreted as a smoothing of the regularised image. For example, an interesting regularisation is proposed in Tanushev and Vese (2007) for a segmented binary image, and the length of the interface is used as penalty term (*i.e.* it gets

4.1. Overview of EIT image reconstruction

Inverse algorithms	Formula
Linear back projection	$\partial\sigma = Jac^T \partial V$, where Jac is the Jacobian matrix, $\partial\sigma$ is the conductivity/permittivity change and ∂V is the voltage measurement.
Tikhonov	$\partial\sigma = (Jac^T Jac + \alpha_I I)^{-1} Jac^T \partial V$, where α_I is the Tikhonov regularisation parameter and I is an identity matrix
NOSER	$\partial\sigma = (Jac^T Jac + \alpha_N N)^{-1} Jac^T \partial V$, where α_N is the NOSER regularisation parameter and N is the NOSER diagonal matrix
Laplace	$\partial\sigma = (Jac^T Jac + \alpha_L L)^{-1} Jac^T \partial V$, where α_L is the Laplace regularisation parameter and L is Laplacian filter matrix
Landweber	$\partial\sigma_{k+1} = \partial\sigma_k + \alpha Jac^T (\partial V - Jac \cdot \partial\sigma_k)$, where α is the Landweber relaxation factor and k indicates the number of iterations

Table 4.1: Linear back projection and other inverse reconstruction algorithms. Adapted from Wei et al. (2015).

minimised under constraint).

4.1.3 Image segmentation techniques

An interesting approach for imaging of multiphase flows is image segmentation. The resistivity (and permittivity) can only take values in a discrete set:

$$\rho(x) \in \{\rho_1, \rho_2, \dots, \rho_N\}, \quad (4.14)$$

with N the number of phases and ρ_i the resistivity of the i^{th} phase.

A very clear description of an image segmentation technique applied to the EIT inverse problem is given in Tanushev and Vese (2007). A binary model of the conductivity profile of a two-phase flow is generated. A Lipschitz-continuous functional function ϕ is introduced. The zero level-line of ϕ will define the phase interface. The Heavyside step function evaluated for ϕ represent the phase indicator function:

$$H(\phi) = \begin{cases} 1 & \text{if } \phi(x) > 0 \\ 0 & \text{if } \phi(x) \leq 0 \end{cases} \quad (4.15)$$

Tanushev and Vese (2007) considered an adjoint formulation of the inverse problem and used the length of the interface as a penalty term for regularisation. The regularisation is smart for two-phase flows because the minimisation of the interfacial area reflects the physics. The functional ϕ is to be optimised for minimising the least-square formulation of the inverse problem. To the best of the author's knowledge, these methods have been essentially studied in 2D reconstruction from numerical solutions eventually corrupted by artificial noise (Tanushev and Vese, 2007; Brühl and Hanke, 2000; Chan and Vese, 2001; Chung et al., 2005). Using segmentation techniques is correct only if the resolution and the mesh are adequate given the characteristic length of inclusion in the image. The problem of image segmentation

is that a sufficiently fine mesh need to be used in order that the assumptions yielded by the segmentation are valid (Dupré et al., 2015). The gain in stability of the reconstruction algorithm could be worth the extra computational efforts with a refined mesh.

The inverse problem of electrical tomography consists in estimating the distribution of electrical properties within the study volume that best fits the set of voltage and current measurements at the boundary electrodes for all excitation patterns in the data collection strategy. The Newton-Raphson methods aim at minimising an objective function. The non-linear contribution to the Hessian method is frequently neglected or replaced by a regularisation term. Image segmentation techniques can be used to inject information on the phase properties and recover shape of interface.

4.2 Two-phase flow imaging method

This section concerns the inversion method for image reconstruction developed within the framework of this Ph.D. research. The method has been named *AT3NA*, standing for "*Algorithme de Tomographie en 3D NOSER et Aplaniissement*" in French. It is based on measurement data obtained experimentally with the full scan strategy. The forward problem solver is based on finite element methods in 3D. Firstly, the reconstruction is performed in 3D considering the NOSER algorithm. Secondly, the distribution of the conductivity is assumed invariant along the axis of the cylindrical study volume and the inversion matrix is recast in a pseudo-2D formulation. This assumption is adequate for the 16-electrodes ring sensor in ProME-T. In the current version of the algorithm, the matrix is pre-computed for a *a priori* reference frame that is a homogeneous water-filled medium. In future developments, a set of matrices will be pre-computed for *a priori* reference images selected for representative flow regimes in a given experimental set-up. The adequate matrix will be selected based on the result of the flow regime identification methodology described in Chapter 3.

4.2.1 Forward problem with EIDORS solver

The preliminary step for image reconstruction is to set a model and solver for the forward problem. The EIDORS open-source project is a compilation of Matlab scripts available online developed for solving the forward and inverse problem in soft-field tomography and generating images. EIDORS stands for "*Electrical Impedance Tomography and Diffuse Optical Tomography Reconstruction Software*". The project started with the contribution of Polydorides (2002) and has been developed since then, with the latest release in May 2015. The simulation results for the forward problem in Chapter 2 have been obtained with the EIDORS forward solver.

Forward model and solver

In EIDORS, the forward problem is solved using the finite elements method (FEM). First, the sensor (test section and electrodes) needs to be modelled. A EIDORS model variable is created with the built-in EIDORS function: `ng_mk_cyl_models`. The first argument contains characteristics of the cylindrical study volume: radius (50 mm) and height (190 mm, for the 3D configuration). The second argument specifies the arrangement of the electrode array: number of rings (1), their elevations (95 mm) and the number of electrodes per ring (16). This function allows electrodes to be specified individually if they are not arranged uniformly around the test section. The third argument describes the geometry of electrodes: for circular shape, the radius (0.5 mm). Extra arguments can be included for options or additional geometrical shapes (*e.g.* for declaring the insulating phase). EIDORS includes a built-in mesh generator (using NetGen mesher) or supports user-defined mesh. In the simulations, the built-in mesh has been used. Parameters for mesh generation can be specified in the model to control the refinement of the mesh. There is a maximum size for elements

adjacent to electrodes and a maximum size for elements within each geometrical shape of the model (in particular for the cylindrical study volume). The data collection strategy also needs to be included in the forward model (adjacent being the default for EIDORS). A separate Matlab function has been written to implement the full scan strategy. This script generates each excitation pattern by calling the EIDORS function *mk_stim_patterns*, with arguments specifying a unit current, the source and drain electrodes, and an adjacent measurement strategy. Next, the electrical properties are set for each mesh element of the model. In our simulations, they are specified globally for each shape: the background conductivity is set for the cylindrical study volume and is modified for all additional geometrical shapes modelling inclusions. Yet, the conductivity of individual mesh element can be specified (which can be used for Jacobian computation with perturbation methods). By default, the electrode gap model is used in EIDORS. Indices of the electrode nodes are stored in the electrode class object and set to the same electrical potential.

The EIDORS model is compiled into an EIDORS image variable with the *mk_image* function. The mesh is automatically generated, and iteratively refine to satisfy the maximum element size set by the user. The results of the forward problem (voltage at each electrode for each excitation pattern) are obtained with the EIDORS function *fwd_solve*. In this thesis, the default option has been considered (first order computation of the finite element method).

Analysis of mesh convergence

An analysis of the convergence of results with finer mesh has been performed in order to find input parameters that provide a right balance between accuracy and computational power. The problem with soft fields (*e.g.* low frequency electrical currents) is that the accuracy is not only dependent on the mesh elements, but also on the distribution of electrical properties. In other words, the optimal mesh structure is not the same for two-different images. The focus has been given to the homogeneous reference medium. Two parameters are set: the maximum size of the mesh elements within the cylindrical study volume *maxsz_{cyl}* and the maximum size of the elements near the electrodes *maxsz_{elec}*. Simulations have been performed with varying *maxsz_{cyl}* and *maxsz_{elec}* parameters. In the absence of analytical solution for our model, the reference solution was selected for the simulation with the maximum number of elements possible (*maxsz_{cyl}*=2 and *maxsz_{elec}*=0.008) with the memory installed on the computer (24 GB with usage of Swap space). The accuracy of each simulation is computed as the square norm of the relative difference of the results with the reference solution. The relationships between the accuracy and the number of elements in the finite element model are displayed in Figures 4.1 and 4.2, for varying *maxsz_{cyl}* and *maxsz_{elec}* parameters respectively.

The detailed analysis of the mesh convergence provides us adequate values of the *maxsz_{cyl}* and *maxsz_{elec}* parameters: 5 and 0.05 respectively. As mentioned previously, there is no insurance that simulating an image with high gradients of conductivity will yield accurate results. In practice, the structure of the mesh generated is totally different when additional shapes are included in the EIDORS model. The boundary of the shape is covered with a fine

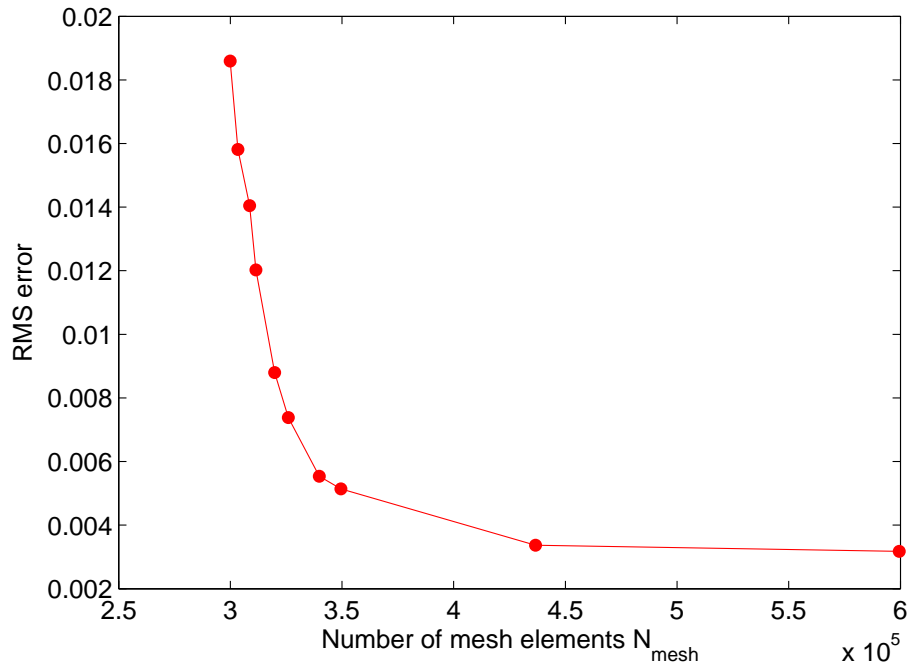


Figure 4.1: Accuracy of simulations for meshes with various levels of refinement (varying $maxsz_{cyl}$)

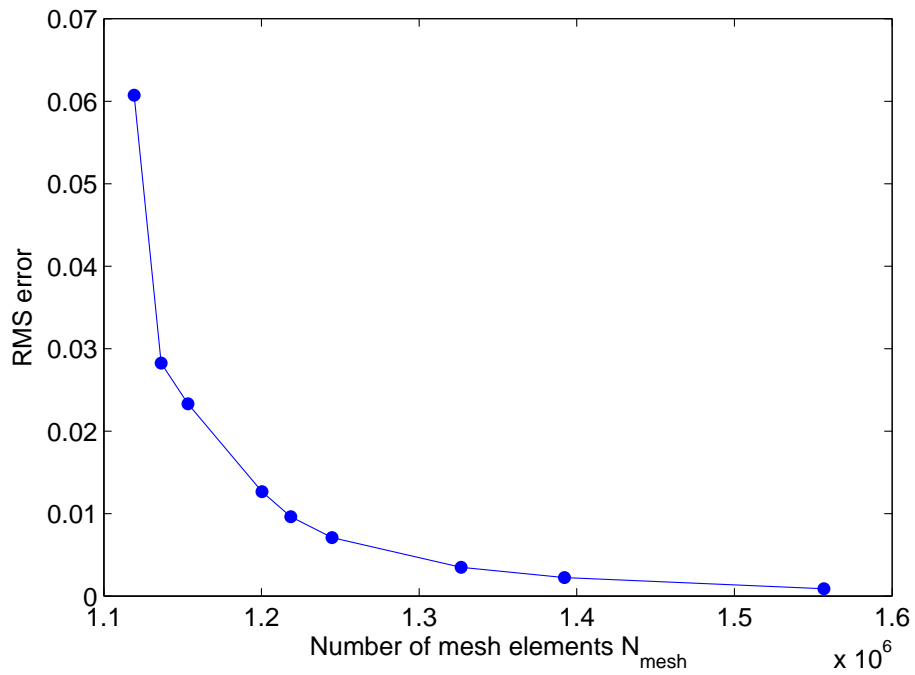


Figure 4.2: Accuracy of simulations for meshes with various levels of refinement (varying $maxsz_{elec}$)

2D mesh and the elements near the interface have smaller volume, which is adequate to increase the sensitivity of the numerical model in the zones with higher contrast. Because of the vast number of parameters, the advanced analysis of mesh structures for simulations of non-homogeneous media has been considered out of the scope of the present study.

4.2.2 3D inversion with NOSER algorithm

At this step of the development of AT3NA, the *a priori* image guess is the homogeneous medium, but the long-term strategy is to pre-compute inversion matrices for a set of model of two-phase flows for various flow regimes and phase fractions. The NOSER method is being used in AT3NA. It consists in the least-square method with a reorganised mesh numbering and the Levenberg-Marquardt regularisation (Cheney et al., 1990).

The NOSER algorithm has been proposed by Cheney et al. (1990) (NOSER stands for Newton's One Step Error Reconstruction). Originally, the *a priori* guess is a constant conductivity distribution, and the conductivity is selected to minimise the error functional. The forward computations use the finite element methods in 2D. The mesh for the inverse problem needs to be selected not too fine because that worsen the conditioning of the problem. Following the Newton approach to solving the least-square formulation of the inverse problem, the derivative of the Jacobian matrix is the sum of two matrices: \mathbf{A}_{lin} (linear problem) and \mathbf{A}_{nl} (non-linear contribution). In order to decrease the ill-conditioning of \mathbf{A}_{lin} , the "*mesh is numbered so that nearby elements have close indices*". Thereby, the largest elements of the matrix \mathbf{A} will be on and near the diagonal. The non-linear contribution to the Jacobian matrix, \mathbf{A}_{nl} , is replaced by a multiple of the diagonal of \mathbf{A}_{lin} . This step is the Levenberg-Marcquardt approximation for regularisation of the problem. It is equivalent to an additional constraint that is the minimisation of the norm of the resistivity distribution. In the original algorithm, the regularisation parameter "*was selected empirically to produce a suitable balance between stability on the one hand and image contrast and definition on the other*".

The Jacobian matrix Jac in Equation (4.5) is calculated with the EIDORS function `calc_jacob`. It is derived based on "*the formulation of an adjoint problem*" as the "*dot product of the current and measurement fields multiplied with the integrals of the gradients of the shape function over each of the tetrahedral elements*" (Polydorides, 2002). Next, the "*mesh is numbered so that nearby elements have close indices*". A sparse permutation matrix $iRtR$ obtained with the EIDORS function `prior_noser` translate the original mesh into the newly ordered mesh. With this indexing strategy, the Jacobian matrix has its "*largest elements on and near the diagonal*", and the condition number of the matrix is increased. The problem is regularised with the Levenberg-Marquardt technique, *i.e.* the non-linear contribution to the derivative of the Jacobian matrix is replaced with an identity matrix iRN (see Equation (4.11)) multiplied by a scaling factor λ_{reg} . It can be interpreted as the minimisation of the norm of the resistivity

vector ρ under constraint (Kim et al., 2001). The 3D inversion matrix is given by:

$$RM = (iRtR \cdot Jac^T) \left(Jac \cdot iRtR \cdot Jac^T + \lambda_{reg}^2 \cdot iRN \right)^{-1}. \quad (4.16)$$

3D image is obtained multiplying the inversion matrix RM by the vector of the relative voltage changes between the reference data and the image data.

The computational cost of the calculation of the inversion matrix is dominated by the re-ordering of the mesh. The control parameter λ_{reg} for the regularisation matrix in Equation (4.10) needs to be specified by the user, and its selection greatly influences the quality of reconstructed images (Wei et al., 2015). Some authors refer to this parameter as the *fidelity term*. As the ill-posedness decreases, the norm of the resistivity image ρ first decreases. As the regularisation further increase, it takes over the information of the measurement and there is a mismatch between the solution and the measurements. The optimal regularisation parameter λ_{reg} can be found with the L-curve method, as illustrated in Figure 4.3 (Wei et al., 2015). At this stage of the development of AT3NA, the computational time is high because a fine mesh is being used to ensure accurate simulation results. With a set of 5 inversion matrix for $\lambda_{reg}=0.00, 0.01, 0.05, 0.10$ and 0.40 , it has been found that $\lambda_{reg} = 0.10$ gives reasonable results. The set of images obtained with these 5 inversion matrices are compared and shown in Table 4.2. The experimental set-up is illustrated with Matlab figures showing cell average void fraction based on the precise knowledge of rods position.

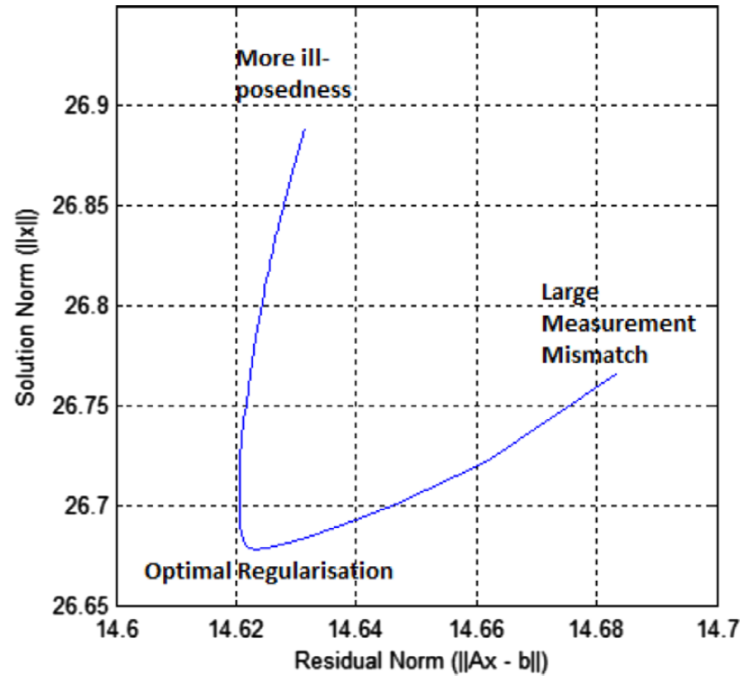


Figure 4.3: L-curve method for assessing optimal regularisation parameter. Adapted from Wei et al. (2015)

Chapter 4. Imaging

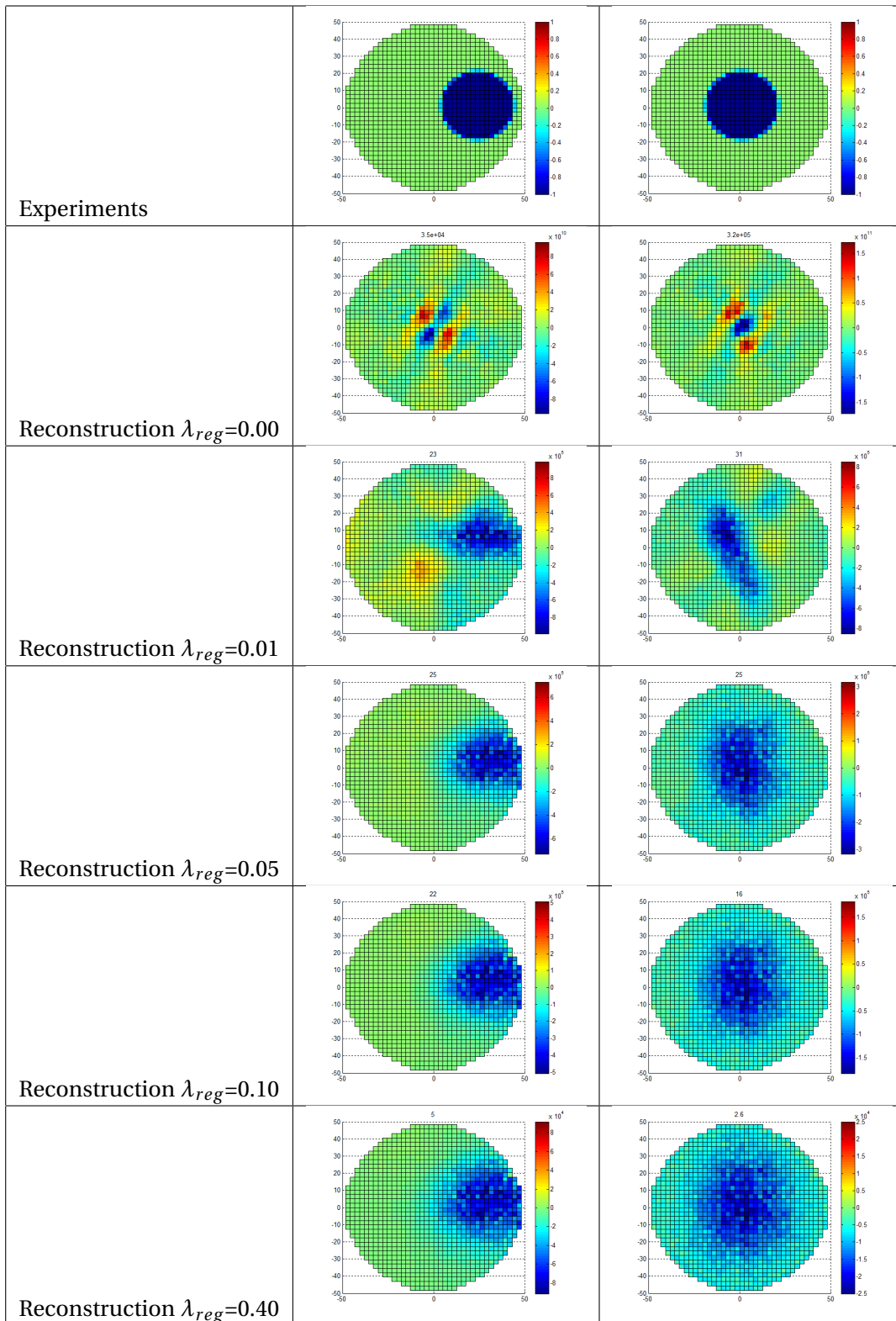


Table 4.2: Set of images obtained with 5 inversion matrices ($\lambda_{reg}=0.00, 0.01, 0.05, 0.10$ and 0.40). On the left, large cylinder ex-centred; on the right, large cylinder centred

4.2.3 Pseudo-2D image reconstruction

Though the reconstruction is made in 3D, since the electrodes are arranged in a plane, it is reasonable to assume the distribution of phases is invariant along the axis of the cylindrical study volume in order to reconstruct cross-sectional images unambiguously. The approach in AT3NA consists in collapsing the 3D inversion matrix into a pseudo-2D inversion matrix. The electrode plane is subdivided into a Cartesian grid of size 2.54 mm. Let us number the pixels in the cross-sectional image, and consider the i^{th} pixel. Its extrusion along the axis of the cylinder generates a parallelepiped Ω_i . The contribution of this pixel (for any measurement j) to the pseudo-2D inversion matrix RM' will be computed based on the contribution of the voxels of the 3D mesh Ω_k , $k = 1, 2, \dots, N_{mesh}$ to the 3D inversion matrix RM :

$$RM'_{i,j} = \frac{\sum_{k=1}^{N_{mesh}} RM_{j,k}(\Omega_k \cap \Omega_i)}{\Omega_k}. \quad (4.17)$$

AT3NA conductivity images are obtained by multiplication of the pre-computed pseudo-2D inversion matrix RM' with the difference of measurements vectors taken for the image and for the reference image:

$$\Delta\sigma = RM' \cdot \Delta V \quad (4.18)$$

The computational time for the image reconstruction has been tested on a standard laptop computer with an Intel Core I5 PCU. For a mesh with 1200 elements, not taking into account the pre-computation of the matrix and the post-processing of raw measurements into measurement vector, the reconstruction takes 1.1 ms.

The image reconstruction method developed within the frame of the thesis first consists in performing the NOSER inversion algorithm on a 3D mesh. The inversion matrix is then projected onto a 2D mesh based on an assumption of a solution invariant along the height of the cylindrical volume: $\sigma = \sigma(r, \theta)$. A binary picture of the phase distribution can finally be obtained by setting a threshold that conserve the cross-sectional average void fraction.

4.3 Assessment of reconstruction images

An objective parameter is proposed for expressing the quality of reconstructed images, *i.e.* their resemblance with the real distribution of phases. A set of benchmark images has been analysed in order to assess the performance of the image reconstruction algorithm. Various alternative versions of the algorithm are tested and the comparison helps to suggest future developments of the algorithm in order to improve further the reliability of the reconstruction.

4.3.1 Benchmark experiments

A set of experiments has been performed to constitute a benchmark. For each experiment, the parameters are identical and the position of all cylinders has been saved for comparison with reconstructed images. The conductivity of the water (doped with table salt) is about $2000 \mu\text{S} \cdot \text{cm}^{-1}$. The data collection strategy is the full scan strategy, the excitation frequency is 10 kHz, 20 samples per period and 2 period per excitation pattern are acquired. The first period is discarded from post-processing. 2 types of cylinders are used: diameter of 10 mm and 40 mm (respectively 1% and 16% void fraction). The cylinders are hanged with the positioning system shown in Figure 2.11. The breadboard matrix pitch is 2.54 mm, so positions of cylinders can be accurately recovered from pictures. A set of 64 measurements of long acrylic cylinders inserted vertically at precise locations in the test section has been obtained. The real images, reconstructed tomograms, and binary images are shown in Table 1 in Appendix. Void fractions range from 0% up to 72%, and various topologies are modelled. Mimics of stratified and annular centred flows are included in the database. The analysis of images reconstructed from benchmark experimental data with the AT3NA algorithm (see Table 1 in Appendix) has been done. The main conclusion is that the performance of the linearised non-iterative AT3NA algorithm is degraded for images with high void fraction. This is expected because these are the problems where non-linearity effects are more acute, especially for air-water two-phase flows with high conductivity contrast. The second conclusion concerns the resolution with the current version of the EIT system and the reconstruction algorithm. It is a complex question to discuss for soft-field tomography, but observation of benchmark images clearly indicate the spatial resolution is not sufficient to recover faithfully shapes of inclusions with scales 1/10 of the test section diameter. Yet, the resolution is sufficient to capture the topology of a flow (*e.g.* distinguish stratified from annular flows). For qualitative discussion, a set of real image/reconstructed image from the benchmark is repeated in Figure 4.4. The benchmark has been generated to assess the level of performance of a given version of the reconstruction algorithm for various images with different features.

Ongoing experiments will complete this benchmark. In particular, a set of experiments with homogeneous media at different liquid conductivities will give a better insight on deviation of cross-sectional average void fractions at increased void fraction (but low image contrast). Additionally, experiments with varying water level in the test section in the 3D configuration will be performed.

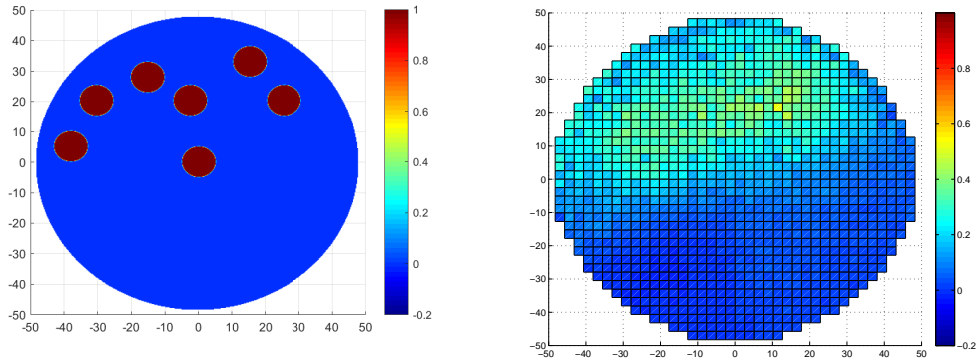


Figure 4.4: Benchmark experiments result: real image on the left and reconstructed tomographic image on the right

4.3.2 Cross-sectional average phase fraction

One of the main objective of this thesis is to provide reliable estimates of the cross-sectional average void fraction in two-phase flows. This is an objective and quantitative parameter for the figure of merit of the ProME-T EIT system and the AT3NA algorithm. In the current version, we suggest considering the sum of all pixels of the reconstructed images. The 18th experiment, the large cylinder at the centre of the test section, is used to find the calibration parameter for void fraction estimate. A threshold is set for the contribution of pixels to the estimate void fraction in order to ensure that the maximum estimate is 100%. The void fraction estimates for the benchmark experiments are indicated in Table 1 in Appendix. The results are summarised in Figure 4.5. They indicate a good performance of the estimation of cross-sectional void fraction out of reconstructed tomograms at low void fraction, but degraded performance at higher void. This is expected due to the increase importance of non-linearities in high contrast images, since the *a priori* solution is taken for the homogeneous reference medium (conducting phase). It is believed that this issue will be mitigated starting from *a priori* solution closer to the real image, selected within a pre-computed database of models. Restricting the analysis to the experiments with less than 16% void fraction, the standard deviation of the results is 1.07%.

With this estimate of the cross-sectional average void fraction, a binary image can be obtained from reconstructed images. One has to select the contour line that separates the image into two regions with the adequate ratio corresponding to the VF. Similar technique is described in Plaskowski et al. (1995) for linear back projection algorithms. The binary images for the benchmark experiments are shown in Table 1 in appendix.

4.3.3 Comparing adjacent, opposite and full scan strategies

A comparison is made with adjacent and opposite data collection strategies and highlights the merits of the full scan strategy. The same algorithm and data files are used, but the

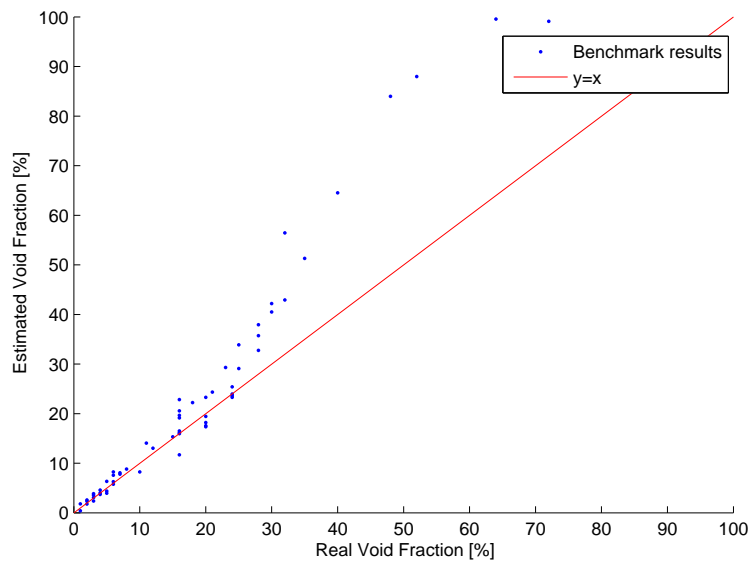
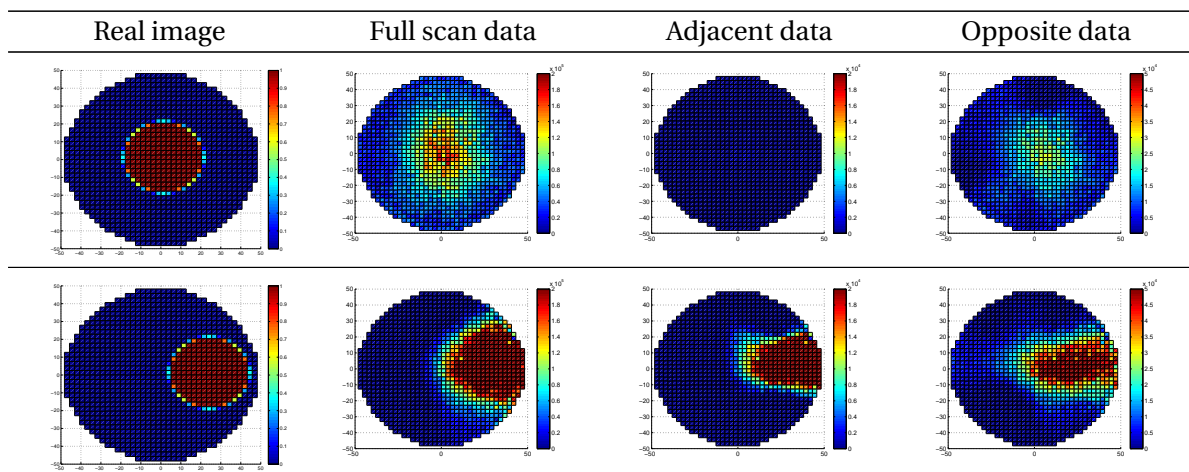


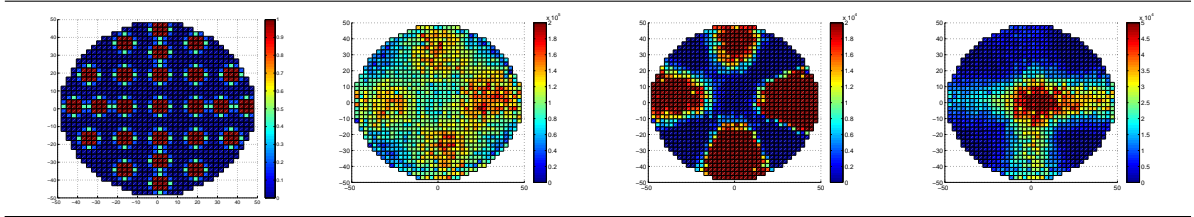
Figure 4.5: Void fraction estimate from measurements, and real void fraction

measurements corresponding to a pattern not considered in a given data collection strategy are replaced by zeros. In adjacent mode, only $S(E_1, E_2), S(E_2, E_3), \dots, S(E_{14}, E_{15})$ and $S(E_1, E_{16})$ are kept, and in opposite strategy, only $S(E_1, E_9), S(E_2, E_{10}), \dots, S(E_8, E_{16})$. The excitation patterns in full scan are given in Equation (2.13). Three benchmark experiments are analysed: $n^\circ 18$, $n^\circ 19$ and $n^\circ 40$. The comparison is shown in Table 4.3. This analysis highlights the deficiency of adjacent measurements for imaging the centre of the study volume, and the deficiency of the opposite measurements for imaging the peripheral zone. However, in this study, the higher performance of full scan data also originates from the increased number of measurements.

Table 4.3: Comparative table of adjacent, opposite and full scan data collection strategies



4.3. Assessment of reconstruction images



A set of 64 experiments has been performed and constitute a benchmark data bank. The comparison of real images and reconstructed tomograms highlight the merits and deficiencies of both the image reconstruction method AT3NA and the prototype ProME-T. The quantitative comparison of cross-sectional average void fraction highlight the reliability of the estimate for low void fraction with the current version of the algorithm. Tests with the data of adjacent and opposite strategies show the relative improvement with the full scan strategy.

5 Conclusion

Conclusion and discussion

Recent improvements of data acquisition systems open up prospects for time-resolved void fraction measurements of two-phase flows via Electrical Impedance Tomography. The ProME-T prototype sensor developed within the framework of this Ph.D. has demonstrated frame acquisition rates up to 6250 fps for adjacent data collection strategy or 833 fps for full scan strategy. The excitation strategy is fundamentally different than most other fast EIT systems reported up to date, because the excitation signal is an AC sine-wave voltage, and the current is measured across the terminals of a sense resistor. Generally, a voltage-to-current converter is included in the system to generate constant current, while differential voltage measurements are taken across the pairs of neighbouring electrodes not used for the excitation. Analysis of the measurements show the AC coupling is reduced with the simplified structured of ProME-T and the increased number of samples per period provide a more efficient filtering of the transient voltage exponential decay caused by electrode contact impedance. The control of the amplitude of the potential at 1 V guarantees that water electrolysis does not take place and provide optimal gains settings for the measurement channels. The novel full scan strategy provides a mean to correct measurements at the current injection electrodes for parasitic electrode-specific impedances. This calibration procedure is made possible by the excitation strategy yielding more excitation pattern than the number of electrodes. In future applications, the set of electrode-specific impedances can be considered as a fingerprint of the sensor to provide tests ensuring the proper state of the EIT system at start-up (no faulty contact, bubble attached to the surface of an electrode, etc.). As compared with the standard data collection strategies (adjacent, diagonal, opposite), many measurements with full scan strategy are linearly dependent but the sensitivity profile is different. According to the weighting of each measurement, the sensitivity through the study volume can be adapted. The two extreme scenarios, adjacent and opposite scanning strategies, will yield high sensitivity near the boundary or at the centre respectively. Ongoing research plan consists in determining optimal weights to get a uniform sensitivity (assuming a homogeneous reference medium).

According to their topologies, multiphase flows can be categorised into flow regimes. The approximation of a real flow to a model based on identified flow regime generally provide good results for estimation of heat transfer and other physical phenomena. Signals from sensors with high dynamical rates and sensitive to phase distribution can be used for flow regime identification. This approach is very appealing for EIT sensors because of the high frame acquisition rates and the complexity of the alternative approach to solve the inverse problem of soft-field tomography. Early in the project, a collaboration with Professor Mylvaganam of University College of South-East Norway has been launched. Experiments have been conducted using the multiphase flow rig and ECT sensor available. Developed horizontal air-water flows at ambient temperature and pressure have been generated and measured. In the methodology, four statistical parameters are used for time series analysis: mean, standard deviation, low-pass and high-pass filters. A data reduction strategy has been implemented to compress the information contained in the 66 ECT measurements into a comprehensive set of 12 eigenvalues of the capacitance matrix. The analysis is invariant under rotation. The methodology consists in a set of Boolean criteria found empirically based on experimental data sets. A very good recognition rate was observed on the experimental data, but more systematic approach to the constitution of the database will be needed to further assess the performance of the method. Numerical simulations of the continuous flow regimes (annular and stratified) support the methodology and highlight how cross-sectional average void fraction can be obtained using the model adapted to the correct flow regime. An analogy with the impedance matrix available from the data of the ProME-T EIT system with the full scan strategy is under investigation. A test section for connection into an in-house flow rig has been designed and an experimental campaign planned. The major differences expected will reside in the higher acquisition rate of ProME-T, the increased sensitivity to spatial effects due to EIT and increased number of electrodes, and the higher sensitivity to highly dynamic flows of the point-like electrode concept because of the axially restricted sensing volume.

The AT3NA algorithm for tomographic image reconstruction has been developed. The data from the full scan strategy is being used, and at this stage, all measurements are identically weighted. AT3NA is based on the NOSER method in 3D: the Newton-Raphson method is used to compute the least-square problem with a Levenberg-Marquardt regularisation and a reordering of the mesh. The inversion matrix is computed based on a *a priori* image of a homogeneous reference medium. Various regularisation parameters have been tested to select an optimal value that decrease the ill-conditioning of the 3D inversion matrix but does not overshadow the fidelity term. Next, the pseudo-2D inversion matrix is computed based on the assumption that the distribution of phases is invariant along the axis of the cylindrical study volume. Finally, the image of two-phase flow can be made binary with a post-processing truncating technique preserving the cross-sectional average void fraction. The AT3NA algorithm has been tested with experimental data obtained with the *ProME-T* prototype sensor and a set of benchmark experiments has been performed to assess the performance of the system for void fraction estimations.

Perspectives

The electrical tomography is a very active field of research for development of innovative instrumentation. There are a variety of concepts at various degree of maturity which brings prospects toward the long-term goal of adapting the ProME-T project for imaging of high pressure high temperature two phase flows.

Two concepts can be adapted with EIT to provide velocimetry capacities to the sensor. Cross-correlation of coherent signals can provide the velocity of the non-continuous phase from a set of measurements at different positions. In tomography, it consists in duplicating the sensor and positioning it upstream or downstream. The technique is relatively simple to implement and processing is not time-consuming. Electromagnetic flow tomography detects the local velocity of a conducting phase by application of a magnetic field and measurement of the electrical potentials at boundary electrodes arising from the magnetic contribution of the Lorentz force $\vec{F} = q(\vec{E} + \vec{v} \wedge \vec{B})$ (Abrolat and Musch, 2016). The theory has been generalised to multiphase flows (Leeungculsatien and Lucas, 2013). For axial velocity measurements, the sensor upgrade would consist of a pair of coils generating a homogeneous magnetic field (the measurement strategy would be identical). A possible set-up is shown in Figure 5.1. However, velocimetry measurements can not be done simultaneously, and the time consists for setting current in the coils remains a challenge for high acquisition rate measurements. Velocimetry and imaging of the flow provides a mean to mass flow rate measurements, which is of major interest in various industrial applications.

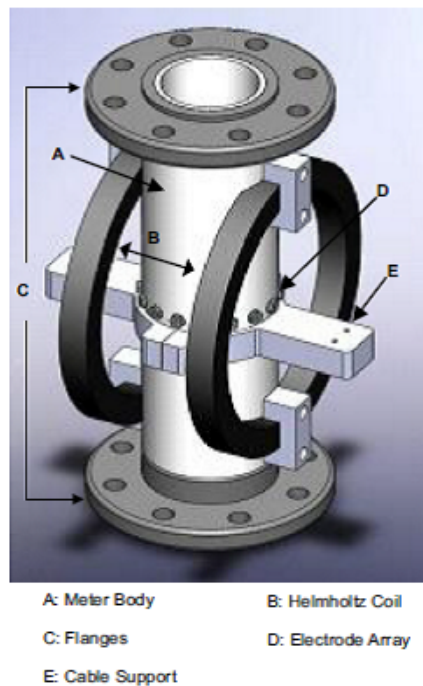


Figure 5.1: Schematic of EMFT sensor. Adapted from Leeungculsatien and Lucas (2013)

Chapter 5. Conclusion

Integration of an EIT sensor into a high pressure high temperature flow rig is a complex task. Stainless steel and carbon steels are the standard option in the nuclear industry. Some research has been done for performing EIT in a metal-walled vessel (Wang et al., 1994) and the conclusion is that the sensitivity is extremely low, notably at a certain distance from the electrodes. *"Metal walls pose a significant problem as current leaks away through the wall. A strategy to accommodate this uses common ground return for transmitted and detected signals"* (York, 2001). Another approach would consist in application of an insulating layer onto the inner diameter of the pipe. Silicon-glass ceramics provide electrical insulation, low viscosity and scratch resistance. They are high pressure high temperature resistant (up to 482 °C in continuous operation with the SGC4000 coating for stainless steel by AREMCO). Despite the efforts required to integrate an EIT sensor into a high pressure high temperature flow rig, the measurement of two-phase steam-water flow is not considerably different from ambient air-water flow if the hardware and data collection strategy allow for a suitably high frame rate. The electrical conductivity of steam is order of magnitudes lower than that of liquid water regardless of the temperature and pressure conditions. As a result, the strategy for image reconstruction will also need to be adapted to high contrast images.

Another challenging application is the measurement of liquid sodium and gas flows. Liquid sodium is considered in Gen IV reactor concepts as a coolant because of its interesting neutronic properties. The temperatures range from the melting temperature of 98 °C up to 550 °C and the pressure is ambient. Gas entrainment in liquid sodium from the surface is one of the major research field for safety assessment of this reactor concept (Moudjed et al., 2016). Important efforts are put in the development of instrumentation for void fraction measurements compatible with the liquid sodium flows (Cavaro et al., 2013).

The EIT reconstructs an image of the conductivity profile within the study volume. In this thesis, the interpretation of the phase fraction has been presented. Yet, in a multiphase flow, the variations of the conductivity would be attributed to temperature (Walker et al., 2009) and pressure to a lesser degree (Horne and Frysinger, 1963). Regarding the presence of phase, conductivity and permittivity images provide different means to discriminate between different materials. Multi-modal EIT/ECT sensors are considered for reconstruction of three-phase flows occurring in pipelines for oil extraction (Wang et al., 2016). Research for oil industry faces this challenge for steam-assisted gravity drainage (Hohrbye et al., 2016) and for the separation of phases.

In the light of the results of this thesis, continued efforts on the development of efficient reconstruction algorithms are considered at the Laboratory of Hydromechanics of Core and Circuits. The performance can be enhanced both in terms of image quality and image calculation time. A consequent amount of research has been performed in EIT image reconstruction, and the focus for flow monitoring applications is to make best use of the knowledge of fluid dynamics. Ongoing research consider pre-computing inversion matrices for various steady flow regimes (annular, stratified, dispersed) and selecting the correct matrix based on flow regime identification techniques.

Bibliography

- Abrolat, J. and Musch, T. (2016). An adaptable sensor for Electromagnetic Flow Tomography utilizing an axially split symmetric ferromagnetic circuit. In *8th World Congress on Industrial Process Tomography WCIPT8*, Foz do Iguaçu, Brazil.
- Ahmed, W. and Ismail, B. (2008). Innovative techniques for two-phase flow measurements. *Recent Patents on Electrical Engineering*, 1(1):1–13.
- Alme, K. (2007). *Material Distribution and Interface Detection Using EIT*. PhD thesis, Norwegian University of Science and Technology.
- Alme, K. and Mylvaganam, S. (2006). Electrical Capacitance Tomography—Sensor Models, Design, Simulations, and Experimental Verification. *IEEE Sensors Journal*, 6(5):1256–1266.
- Banowski, M., Beyer, M., Szalinski, L., Lucas, D., and Hampel, U. (2015). Comparative study of ultrafast X-ray tomography and wire-mesh sensors for vertical gas-liquid pipe flows. In *7th International Symposium on Process Tomography*, Dresden, Germany.
- Bates, R. H. T. (1984). Full-wave computed tomography. Part 1: Fundamental theory. *IEE Proceedings A - Physical Science, Measurement and Instrumentation, Management and Education - Reviews*, 131(8):610–615. Done.
- Borcea, L. (2002). Electrical impedance tomography. *Inverse Problems*, 18(6):R99.
- Borcea, L., Gray, G. A., and Zhang, Y. (2003). Variationally constrained numerical solution of electrical impedance tomography. *Inverse Problems*, 19(5):1159.
- Brennen, C. E. (2005). *Fundamentals of Multiphase Flows*. Cambridge University Press.
- Brühl, M. and Hanke, M. (2000). Numerical implementation of two noniterative methods for locating inclusions by impedance tomography. *Inverse Problems*, 16(4):1029.
- Calderón, A. P. (2006). On an inverse boundary value problem. *Computational & Applied Mathematics*, 25(2-3):133–138.
- Cavaro, M., Payan, C., and Jeannot, J. P. (2013). Towards the characterization of the bubble presence in liquid sodium of Sodium cooled Fast Reactors. In *2013 3rd International*

Bibliography

- Conference on Advancements in Nuclear Instrumentation, Measurement Methods and their Applications (ANIMMA)*, pages 1–11.
- Chan, T. F. and Vese, L. A. (2001). Active contours without edges. *IEEE Transactions on Image Processing*, 10(2):266–277.
- Cheney, M., Isaacson, D., Newell, J. C., Simske, S., and Goble, J. (1990). NOSER: An algorithm for solving the inverse conductivity problem. *International Journal of Imaging Systems and Technology*, 2(2):66–75. Done.
- Chung, E. T., Chan, T. F., and Tai, X.-C. (2005). Electrical Impedance Tomography Using Level Set Representation and Total Variational Regularization. *J. Comput. Phys.*, 205(1):357–372.
- Cohen-Bacrie, C., Goussard, Y., and Guardo, R. (1997). Regularized reconstruction in electrical impedance tomography using a variance uniformization constraint. *IEEE Transactions on Medical Imaging*, 16(5):562–571.
- Costigan, G. and Whalley, P. B. (1997). Slug flow regime identification from dynamic void fraction measurements in vertical air-water flows. *International Journal of Multiphase Flow*, 23(2):263–282.
- Dupré, A., Ricciardi, G., and Bourennane, S. (2015). On the feasibility of retrieving phase indicator function of a bubble flow in an electrical impedance tomography experiment. In *7th International Symposium on Process Tomography*, Dresden, Germany.
- Dupré, A., Ricciardi, G., and Bourennane, S. (2016a). Development of a prototype device for imaging two-phase flows via electrical impedance tomography. In *Specialists Workshop on Advanced Instrumentation and Measurement*, Livorno, Italy.
- Dupré, A., Ricciardi, G., and Bourennane, S. (2017). Novel Approach for Analysis and Design of High-Speed Electrical Impedance Tomographic System for Void Fraction Measurements in Fast Two-Phase Flows. *IEEE Sensors Journal*, 17(14):4472–4482.
- Dupré, A., Ricciardi, G., Bourennane, S., and Mylvaganam, S. (2016b). Identification of flow regimes using raw EIT measurements. In *8th World Congress on Industrial Process Tomography WCIPT8*, Foz do Iguaçu, Brazil.
- Dupre, A., Ricciardi, G., Bourennane, S., and Mylvaganam, S. (2017). Electrical Capacitance Based Flow Regimes Identification - Multiphase Experiments and Sensor Modelling. *IEEE Sensors Journal*, PP(99):1–1.
- Fang, W. and Cumberbatch, E. (2005). Matrix properties of data from electrical capacitance tomography. *Journal of Engineering Mathematics*, 51(2):127–146.
- Gamio, J. C. (2002). A comparative analysis of single- and multiple-electrode excitation methods in electrical capacitance tomography. *Measurement Science and Technology*, 13(12):1799. Done.

- George, D. L., Torczynski, J. R., Shollenberger, K. A., O'Hern, T. J., and Ceccio, S. L. (2000). Validation of electrical-impedance tomography for measurements of material distribution in two-phase flows. *International Journal of Multiphase Flow*, 26(4):549–581.
- Hampel, U., Banowski, M., and Krepper, E. (2016). Ultrafast X-ray tomography for two-phase flow experiments. In *Specialists Workshop on Advanced Instrumentation and Measurement*, Livorno, Italy.
- Hanke, M., Harrach, B., and Hyvönen, N. (2011). Justification of point electrode models in electrical impedance tomography. *Mathematical Models and Methods in Applied Sciences*, 21(06):1395–1413.
- Haykin, S. S. (2009). *Neural Networks and Learning Machines*. Prentice Hall.
- Hernandez, P. (2008). *Gas-liquid two-phase flow in inclined pipes*. PhD thesis, Nottingham University.
- Hervieu, E. and Seleglim jr., P. (1998). An objective indicator for two-phase flow pattern transition. *Nuclear Engineering and Design*, 184(2–3):421–435.
- Hohrbye, J., Mathiesen, V., and Moldestad, B. (2016). Heavy Oil Production With Energy Effective Steam-assisted Gravity Drainage. *International Journal of Energy Production and Management*, 1(4):349 – 358.
- Horne, R. A. and Frysinger, G. R. (1963). The effect of pressure on the electrical conductivity of sea water. *Journal of Geophysical Research*, 68(7):1967–1973.
- Huang, S. M., Plaskowski, A. B., Xie, C. G., and Beck, M. S. (1988). Capacitance-based tomographic flow imaging system. *Electronics Letters*, 24(7):418–419.
- Joseph-Mathurin, N., Dorieux, O., Kraska, A., Bertrand, A., Santin, M., Tayara, N. E. T. E., and Dhenain, M. (2010). Magnetic resonance imaging in primates. The example of the mouse lemur (*Microcebus murinus*): From detection of pathological aging to therapeutic evaluations. *Revue de primatologie*, 1(2).
- Karki, B. (2016). Electrical Conductivity Based Flow Regime Recognition of Two-Phase Flows in Horizontal Pipeline. In *8th World Congress on Industrial Process Tomography WCIPT8*, Foz do Iguaçu, Brazil.
- Kauppinen, P., Hyttinen, J., and Malmivuo, J. (2006). Sensitivity Distribution Visualizations of Impedance Tomography Measurement Strategies. *International Journal of Bioelectromagnetism*, 8(1):VII/1 – VII/9. Done.
- Kevles, B. (1997). *Naked to the Bone: Medical Imaging in the Twentieth Century*. Rutgers University Press.

Bibliography

- Kim, M. C., Kim, S., Kim, K. Y., and Lee, Y. J. (2001). Regularization methods in electrical impedance tomography technique for the two-phase flow visualization. *International Communications in Heat and Mass Transfer*, 28(6):773–782.
- Kotre, C. (1993). *Studies of image reconstruction methods for electrical impedance tomography*. PhD thesis, Newcastle University.
- Kotre, C. J. (1988). A fast approximation for the calculation of potential distributions in electrical impedance tomography. *Clinical Physics and Physiological Measurement: An Official Journal of the Hospital Physicists' Association, Deutsche Gesellschaft Fur Medizinische Physik and the European Federation of Organisations for Medical Physics*, 9(4):353–361.
- Kotre, C. J. (1994). EIT image reconstruction using sensitivity weighted filtered backprojection. *Physiological Measurement*, 15(2A):A125.
- Lakshmana, S., Maru, W., Holland, D., and Sederma, A. (2015). Multiphase flow measurement using Magnetic Resonance Imaging. In *7th International Symposium on Process Tomography*, Dresden, Germany.
- Lee, J. Y., Ishii, M., and Kim, N. S. (2008). Instantaneous and objective flow regime identification method for the vertical upward and downward co-current two-phase flow. *International Journal of Heat and Mass Transfer*, 51(13–14):3442–3459.
- Leeungculsatien, T. and Lucas, G. P. (2013). Measurement of velocity profiles in multiphase flow using a multi-electrode electromagnetic flow meter. *Flow Measurement and Instrumentation*, 31:86–95.
- Lemonnier, H. and Peytraud, J. F. (1998). Is 2d impedance tomography a reliable technique for two-phase flow? *Nuclear Engineering and Design*, 184(2–3):253–268.
- Libert, N., Morales, R. E. M., and da Silva, M. J. (2016). Capacitive measuring system for two-phase flow monitoring. Part 1: Hardware design and evaluation. *Flow Measurement and Instrumentation*, 47:90–99.
- Lowe, D. and Rezkallah, K. S. (1999). A capacitance sensor for the characterization of micro-gravity two-phase liquid-gas flows. *Measurement Science and Technology*, 10(10):965.
- Lowe, D. C. (1997). *A study on flow regime identification in microgravity gas-liquid flows using a capacitance sensor*. PhD thesis, University of Saskatchewan.
- Ma, Y., Xu, L., and Jiang, C. (1999). Experimental study of the guard electrodes in an ERT system. In *1st World Congress on Industrial Process Tomography WCIPT1*.
- Mandhane, J., Gregory, G., and Aziz, K. (1974). A flow pattern map for gas—liquid flow in horizontal pipes. *International Journal of Multiphase Flow*, 1(4):537–553.
- Mansfield, P. (2003). Nobel-Prize Lecture: Snap-shot MRI.

- McQuillan, K. W. and Whalley, P. B. (1985). Flow patterns in vertical two-phase flow. *International Journal of Multiphase Flow*, 11(2):161–175.
- Meeker, D. (2015). Finite Element Method Magnetics, Version 4.2, User's Manual.
- Mi, Y., Ishii, M., and Tsoukalas, L. H. (2001). Flow regime identification methodology with neural networks and two-phase flow models. *Nuclear Engineering and Design*, 204(1–3):87–100.
- Moudjed, B., Excoffon, J., Riva, R., and Rossi, L. (2016). Experimental study of gas entrainment from surface swirl. *Nuclear Engineering and Design*, 310:351–362.
- Nakath, R., Schuster, C., and Hurtado, A. (2013). Bubble size distribution in flow boiling of aqueous boric acid under high pressure. *Nuclear Engineering and Design*, 262:562–570.
- Nissinen, A., Heikkinen, L., Sbarbaro, D., and Vauhkonen, M. (2013). Cylindrically symmetric forward model in electrical impedance tomography with probe geometry. In *7th World Congress on Industrial Process Tomography WCIPT7*.
- Opielinski, K. J. and Gudra, T. (2006). Multi-parameter ultrasound transmission tomography of biological media. *Ultrasonics*, 44, Supplement:e295–e302.
- Paranjape, S., Ritchey, S. N., and Garimella, S. V. (2012). Electrical impedance-based void fraction measurement and flow regime identification in microchannel flows under adiabatic conditions. *International Journal of Multiphase Flow*, 42:175–183.
- Park, K. (2013). *Experimental study of bubble characteristics and heat transfer in subcooled flow boiling of R-134a*. PhD thesis, Norwegian University of Science and Technology.
- Peytraud, J. F. (1995). *Study of electrical impedance tomography for local void fraction measurements in two-phase flow*. PhD thesis, Institut National Polytechnique de Grenoble, Grenoble.
- Pidcock, M. K., Kuzuoglu, M., and Leblebicioglu, K. (1995). Analytic and semi-analytic solutions in electrical impedance tomography. I. Two-dimensional problems. *Physiological Measurement*, 16(2):77.
- Pietruske, H. and Prasser, H.-M. (2007). Wire-mesh sensors for high-resolving two-phase flow studies at high pressures and temperatures. *Flow Measurement and Instrumentation*, 18(2):87–94.
- Plaskowski, A., Beck, M. S., Thorn, R., and Dyakowski, T. (1995). *Imaging Industrial Flows: Applications of Electrical Process Tomography*. CRC Press.
- Polansky, J., Wang, M., and Faraj, J. (2015). Proper orthogonal decomposition as a technique for identifying multiphase flow regime based on electrical impedance tomography. In *7th International Symposium on Process Tomography*, Dresden, Germany.

Bibliography

- Pollak, V. (1974). An equivalent diagram for the interface impedance of metal needle electrodes. *Medical and biological engineering*, 12(4):454–459.
- Polydorides, N. (2002). *Image reconstruction algorithms for soft-field tomography*. PhD thesis, University of Manchester.
- Pradeep, C. (2012). *Tomographic approach to automatic and non-invasive flow regime identification*. PhD thesis, University of Telemark, Norway.
- Pradeep, C. and Mylvaganam, S. (2015). Characterizing slugs in multiphase flow using multi-modal tomometric systems in tilted pipelines. In *7th International Symposium on Process Tomography*, Dresden, Germany.
- Prasser, H. M., Böttger, A., and Zschau, J. (1998). A new electrode-mesh tomograph for gas–liquid flows. *Flow Measurement and Instrumentation*, 9(2):111–119.
- Prasser, H.-M., Stucki, S., Betschart, T., and Eisenberg, J. (2015). Interfacial area density measurement using a three-layer wiremesh sensor. In *International Conference NURETH-16*.
- Radon, J. (1986). On the determination of functions from their integral values along certain manifolds. *IEEE Transactions on Medical Imaging*, 5(4):170–176.
- Ramskill, N. P. and Wang, M. (2011). Boolean logic analysis for flow regime recognition of gas–liquid horizontal flow. *Measurement Science and Technology*, 22(10):104016.
- Rocha, M. S. and Simões-Moreira, J. R. (2008). Void Fraction Measurement and Signal Analysis from Multiple-Electrode Impedance Sensors. *Heat Transfer Engineering*, 29(11):924–935.
- Ru, Y. and Mylvaganam, S. (2013). Enhanced flow regime identification with SVM using electrical capacitance tomography in fluidized beds. In *7th World Congress on Industrial Process Tomography WCIPT7*.
- Schlaberg, H., Jia, J., Qiu, C., Wang, M., and Li, H. (2008). Development and application of the Fast Impedance Camera - a high performance dual-plane electrical impedance tomography system. In *5th International Symposium on Process tomography*, Zakopane, Poland. Done.
- Schleicher, E., Tschofen, M., Kipping, R., and Hampel, U. (2016). Wire-mesh sensors: recent developments and applications. In *Specialists Workshop on Advanced Instrumentation and Measurement*, Livorno, Italy.
- Seagar, A. D. and Bates, R. H. T. (1985). Full-wave computed tomography. Part 4: Low-frequency electric current CT. *IEE Proceedings A - Physical Science, Measurement and Instrumentation, Management and Education - Reviews*, 132(7):455–466. Done.
- Seleglim, P. and Hervieu, E. (1998). Direct imaging of two-phase flows by electrical impedance measurements. *Measurement Science and Technology*, 9(9):1492.

- Senftle, F. E., Grant, J. R., and Senftle, F. P. (2010). Low-voltage DC/AC electrolysis of water using porous graphite electrodes. *Electrochimica Acta*, 55(18):5148–5153.
- Smolik, W., Kryszyn, P., Wroblewski, P., Stosio, M., Olszewski, T., and Szabatin, R. (2016a). The Hardware Architecture of EVT4 Electrical Capacitance Tomograph. In *8th World Congress on Industrial Process Tomography WCIPT8*, Foz do Iguaçu, Brazil.
- Smolik, W., Kryszyn, P., Wroblewski, P., Stosio, M., Olszewski, T., and Szabatin, R. (2016b). Software for EVT4 Electrical Capacitance Tomograph. In *8th World Congress on Industrial Process Tomography WCIPT8*, Foz do Iguaçu, Brazil.
- Taitel, Y. and Dukler, A. E. (1976). A model for predicting flow regime transitions in horizontal and near horizontal gas-liquid flow. *AIChE Journal*, 22(1):47–55.
- Tan, C., Dong, F., and Wu, M. (2007). Identification of gas/liquid two-phase flow regime through ERT-based measurement and feature extraction. *Flow Measurement and Instrumentation*, 18(5–6):255–261.
- Tan, C., Zhao, J., and Dong, F. (2015). Gas–water two-phase flow characterization with Electrical Resistance Tomography and Multivariate Multiscale Entropy analysis. *ISA Transactions*, 55:241–249.
- Tanushev, N. M. and Vese, L. A. (2007). A Piecewise-Constant Binary Model for Electrical Impedance Tomography. *Inverse Problems and Imaging*, 2:423–435.
- Terzija, N., Yin, W., Gerbeth, G., Stefani, F., Timmel, K., Wondrak, T., and Peyton, A. J. (2011). Use of electromagnetic induction tomography for monitoring liquid metal/gas flow regimes on a model of an industrial steel caster. *Measurement Science and Technology*, 22(1):015501.
- Torczynski, J. R., O’Hern, T. J., Shollenberger, K. A., Ceccio, S. L., and Tassin, A. L. (1996). Finite element method electrical impedance tomography for phase distribution determination in multiphase flows. *Unknown Journal*, 236:497–499.
- Walker, C., Simiano, M., Zboray, R., and Prasser, H. M. (2009). Investigations on mixing phenomena in single-phase flow in a T-junction geometry. *Nuclear Engineering and Design*, 239(1):116–126.
- Wang, H. X. and Zhang, L. F. (2009). Identification of two-phase flow regimes based on support vector machine and electrical capacitance tomography. *Measurement Science and Technology*, 20(11):114007.
- Wang, M. (2005). Seeing a new dimension—The past decade’s developments On electrical impedance tomography. *Progress in Natural Science*, 15(sup1):1–13.
- Wang, M., Dickin, F. J., and Williams, R. A. (1994). Electrical resistance tomography of metal walled vessels and pipelines. *Electronics Letters*, 30(10):771–773.

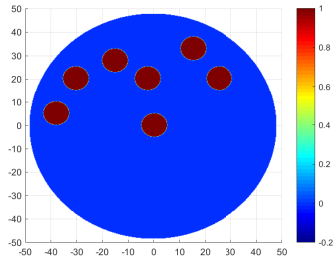
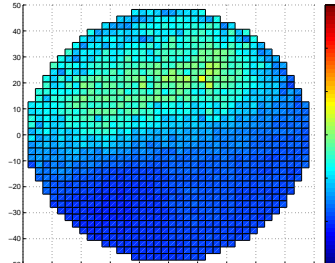
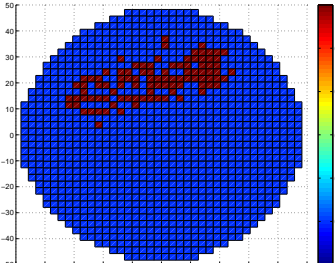
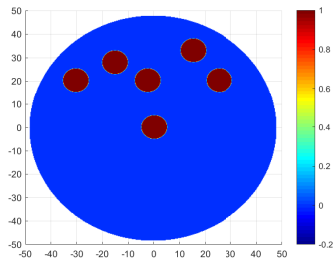
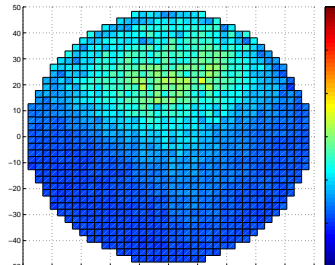
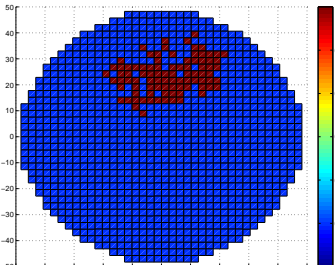
Bibliography

- Wang, M. and Ma, Y. (2006). Over-zero switching scheme for fast data collection operation in electrical impedance tomography. *Measurement Science and Technology*, 17(8):2078.
- Wang, M., Ma, Y., Holliday, N., Dai, Y., Williams, R. A., and Lucas, G. (2005). A high-performance EIT system. *IEEE Sensors Journal*, 5(2):289–299.
- Wang, Q., Polansky, J., Wang, M., Wei, K., Qiu, C., Kenbar, A., and Millington, D. (2016). Experimental evaluation of dual-modality electrical tomographic systems on gas-oil-water flow in horizontal pipeline. In *8th World Congress on Industrial Process Tomography WCIPT8*, Foz do Iguaçu, Brazil.
- Wei, K., Qiu, C., Soleimani, M., and Primrose, K. (2015). ITS Reconstruction Tool-Suite: An inverse algorithm package for industrial process tomography. *Flow Measurement and Instrumentation*, 46, Part B:292–302. Done.
- Wilkinson, A. J., Randall, E. W., Cilliers, J. J., Durrett, D. R., Naidoo, T., and Long, T. (2005). A 1000-measurement frames/second ERT data capture system with real-time visualization. *IEEE Sensors Journal*, 5(2):300–307.
- Xie, C. G., Plaskowski, A., and Beck, M. S. (1989a). 8-electrode capacitance system for two-component flow identification. Part 1: Tomographic flow imaging. *IEE Proceedings A (Physical Science, Measurement and Instrumentation, Management and Education)*, 136(4):173–183.
- Xie, C. G., Plaskowski, A., and Beck, M. S. (1989b). 8-electrode capacitance system for two-component flow identification. Part 2: Flow regime identification. *IEE Proceedings A (Physical Science, Measurement and Instrumentation, Management and Education)*, 136(4):184–190.
- Yang, W. Q., Spink, D. M., York, T. A., and McCann, H. (1999). An image-reconstruction algorithm based on Landweber’s iteration method for electrical-capacitance tomography. *Measurement Science and Technology*, 10(11):1065. Done.
- York, T. (2001). Status of electrical tomography in industrial applications. *Journal of Electronic Imaging*, 10(3):608–619. Done.
- Yorkey, T. J., Webster, J. G., and Tompkins, W. J. (1987). Comparing Reconstruction Algorithms for Electrical Impedance Tomography. *IEEE Transactions on Biomedical Engineering*, BME-34(11):843–852.
- Zhou, J. (2013). *Flow patterns in vertical air/water flow with and without surfactant*. PhD thesis, University of Dayton.

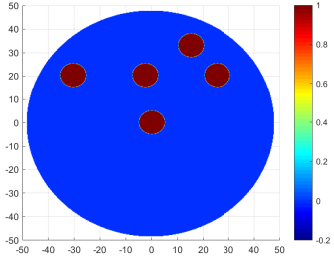
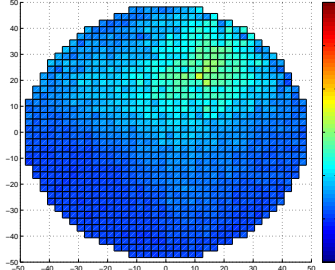
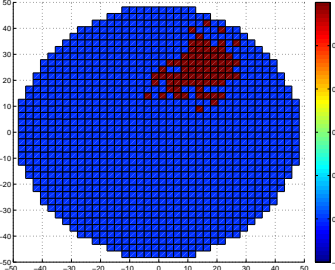
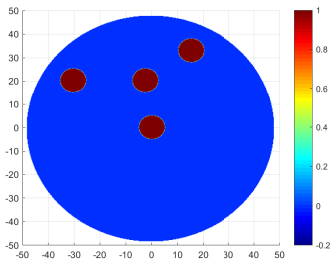
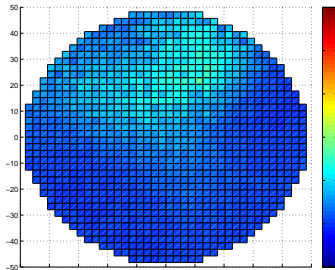
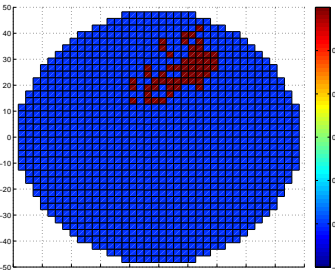
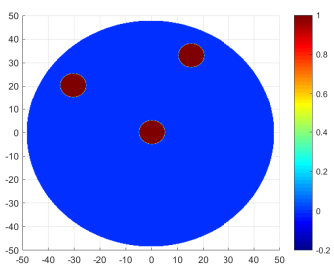
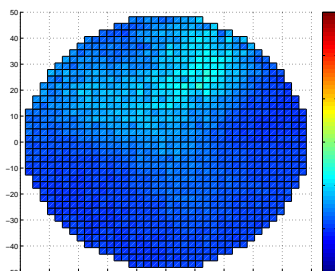
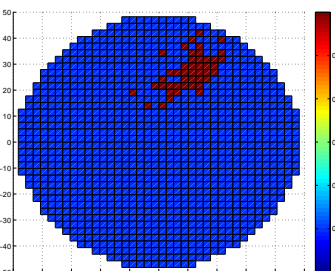
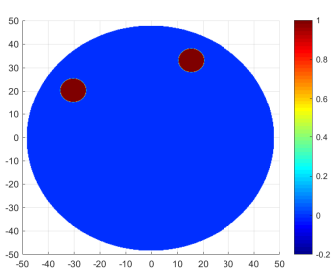
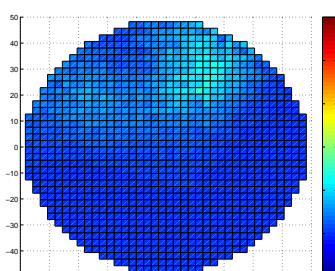
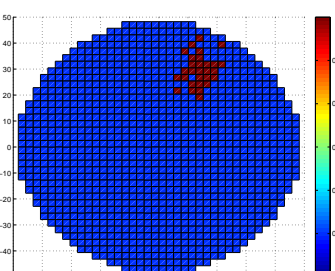
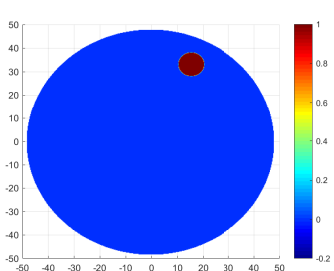
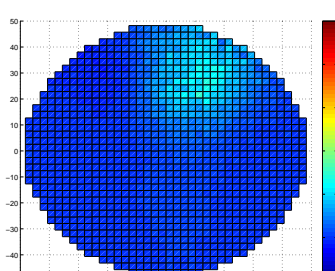
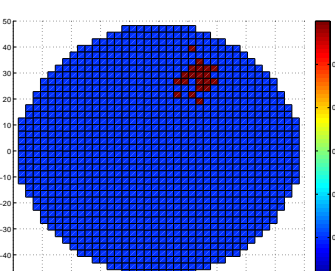
Benchmark images

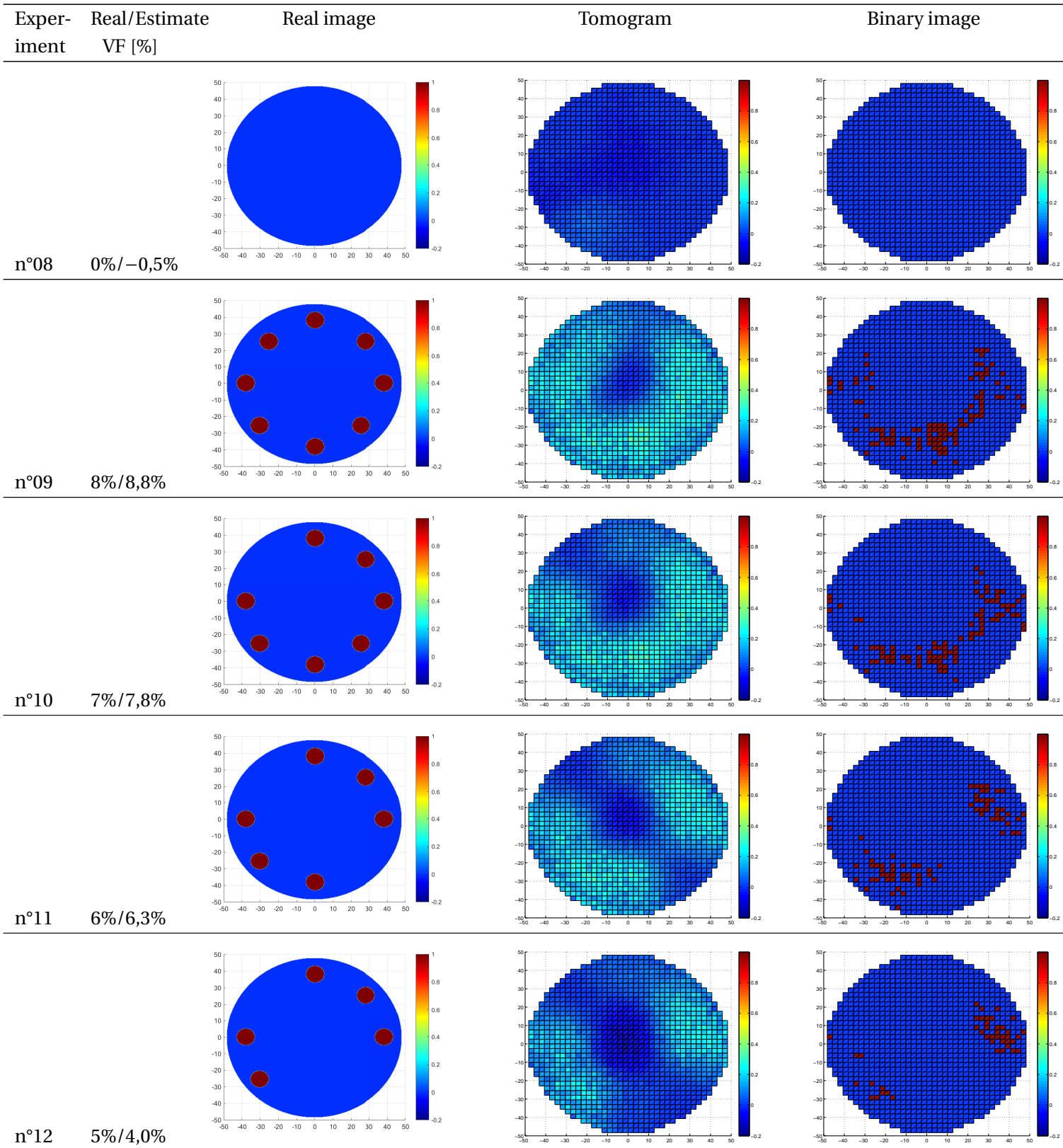
A database of 64 experiments has been compiled into a benchmark to test the performance of reconstruction algorithms. Various void fractions (from 0% up to 72%) and flow topologies (annular, stratified, etc.) are represented. Acrylic cylinders of diameter 10 and 40 mm are hanged vertically in the test section at precise locations with the rod positioning system described in Section 2.3.1. The real images and reconstructed tomograms of the benchmark experiments are shown in Table 1. The void fraction and its estimate from the tomogram are also indicated.

Benchmark for image reconstruction: void fraction (real/estimate), reference image and reconstructed tomograms

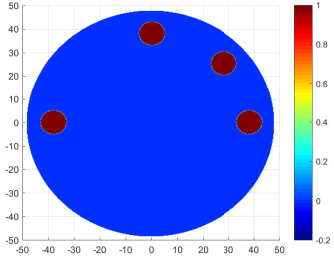
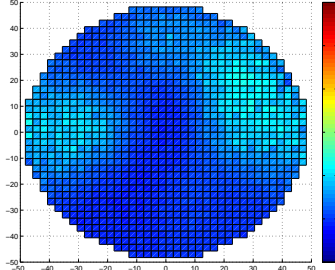
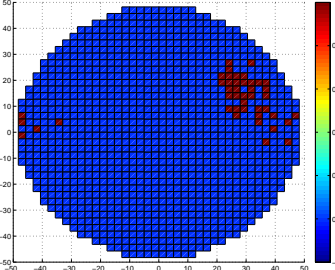
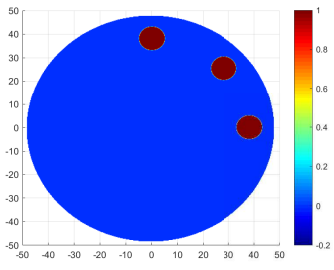
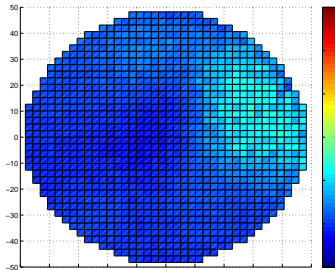
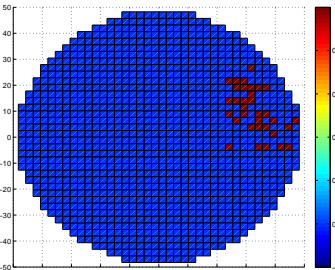
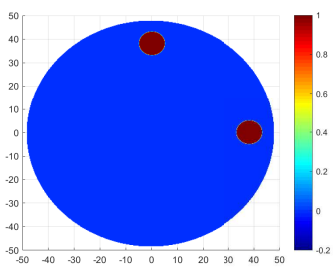
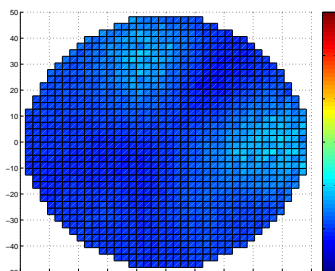
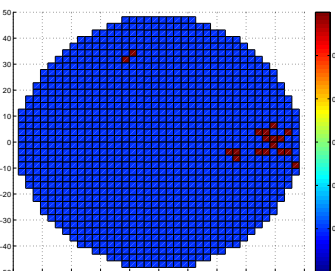
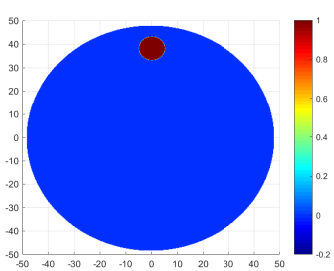
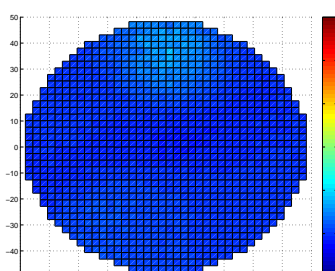
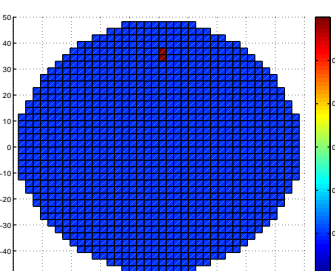
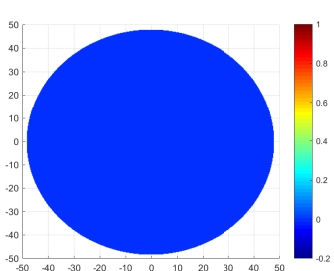
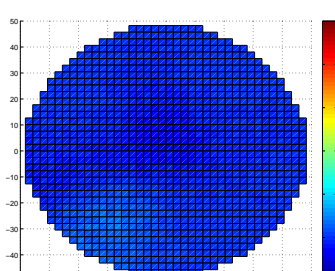
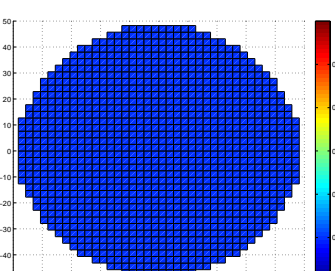
Experiment	Real/Estimate VF [%]	Real image	Tomogram	Binary image
n°01	7%/8,1%			
n°02	6%/7,6%			

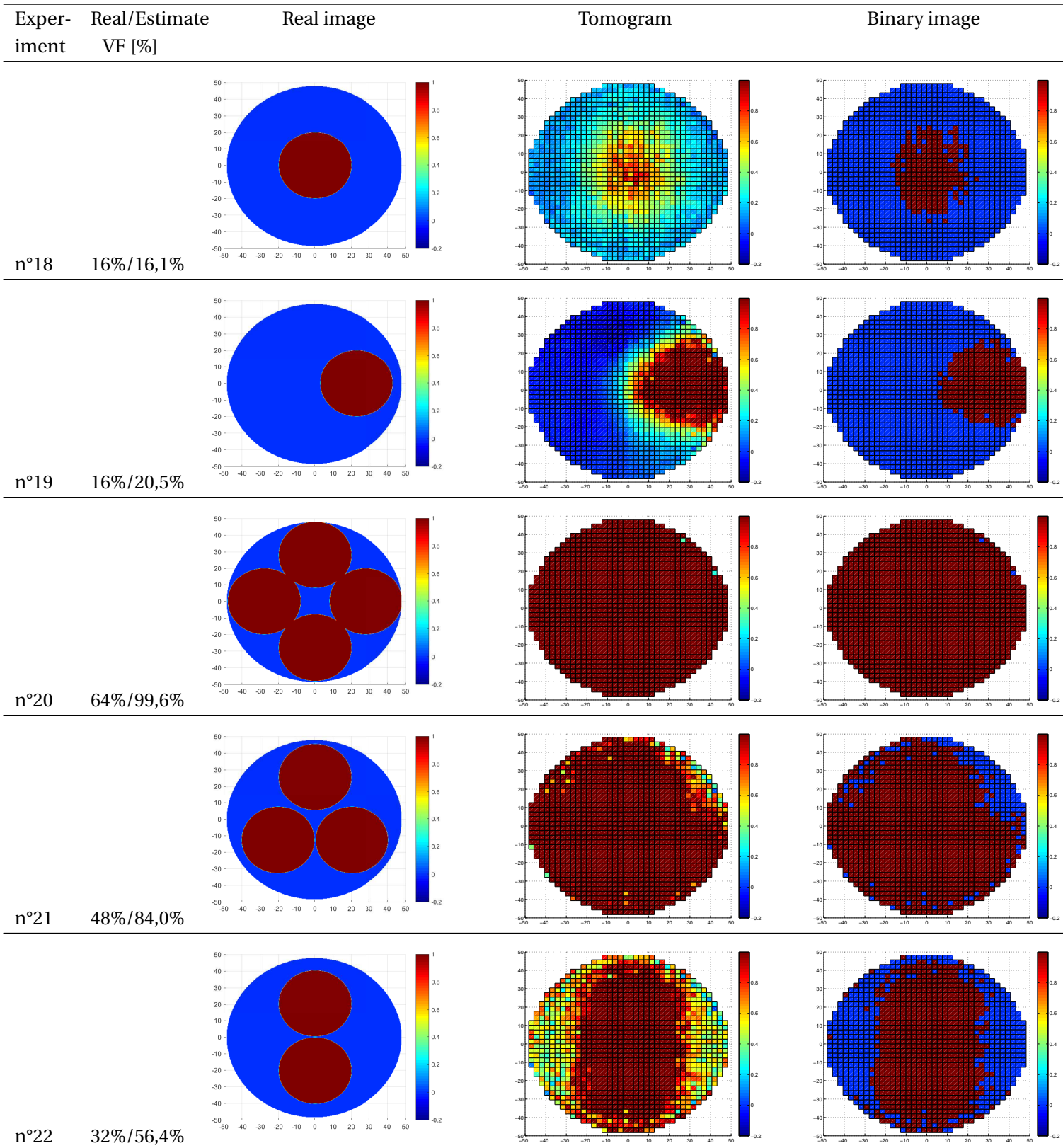
Appendix . Benchmark images

Experiment	Real/Estimate VF [%]	Real image	Tomogram	Binary image
n°03	5%/6,3%			
n°04	4%/4,6%			
n°05	3%/3,9%			
n°06	2%/2,6%			
n°07	1%/1,8%			



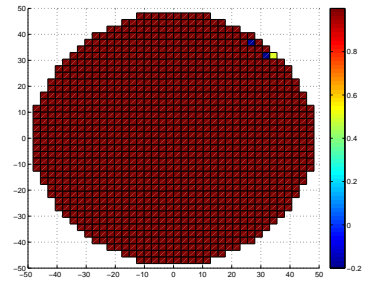
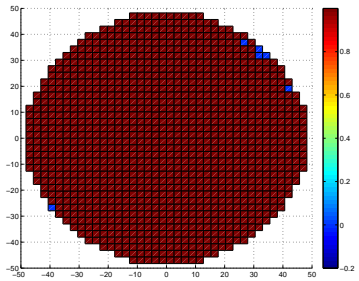
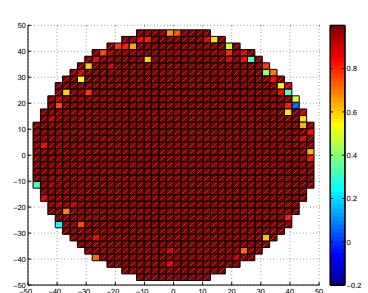
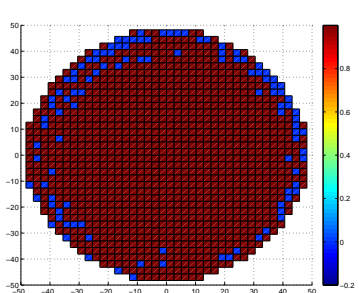
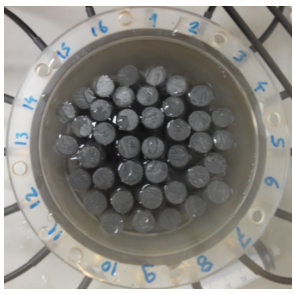
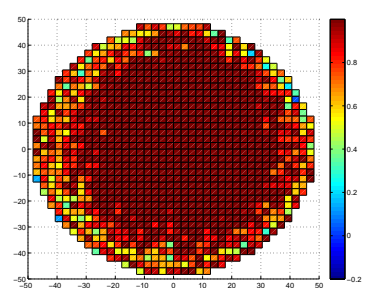
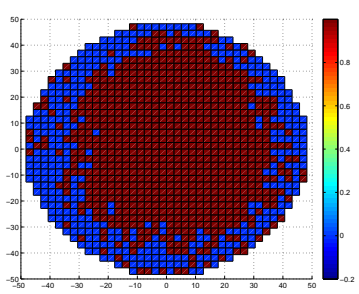
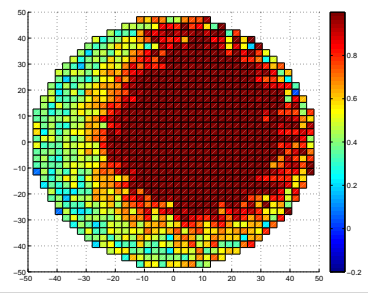
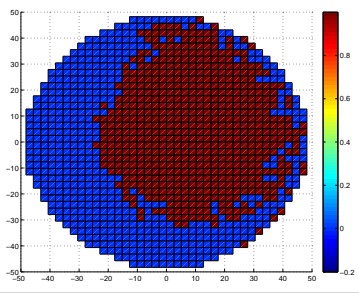
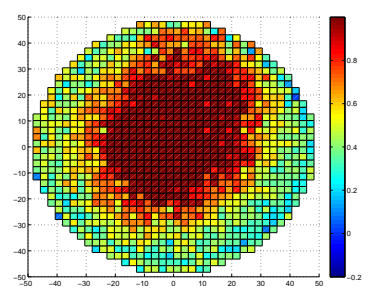
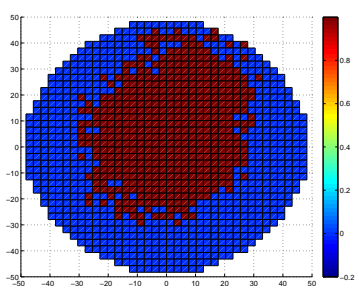
Appendix . Benchmark images

Experiment	Real/Estimate VF [%]	Real image	Tomogram	Binary image
n°13	4%/4,0%			
n°14	3%/3,1%			
n°15	2%/1,8%			
n°16	1%/0,4%			
n°17	0%/-0,6%			

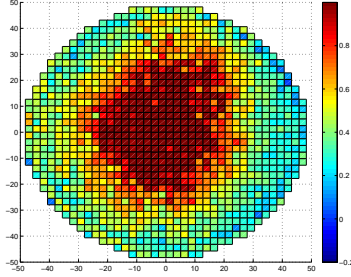
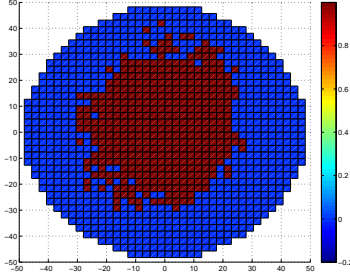
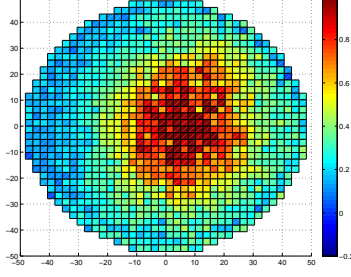
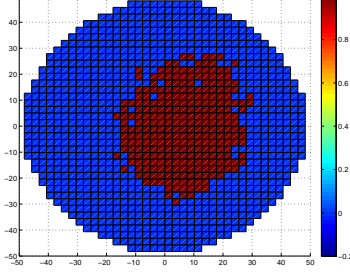
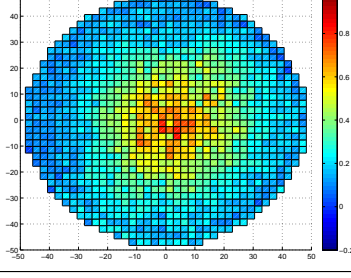
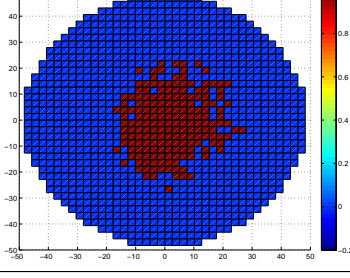
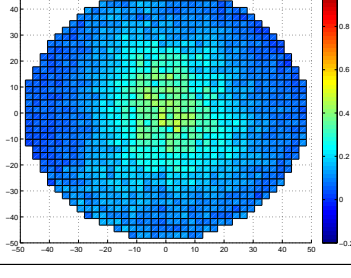
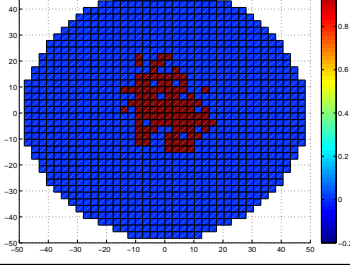
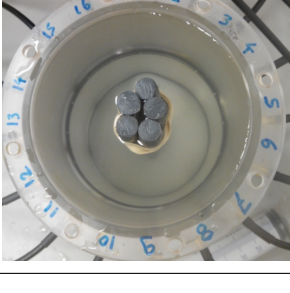
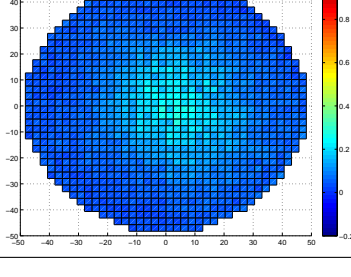
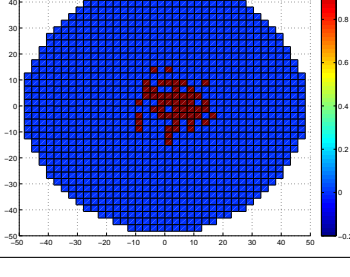


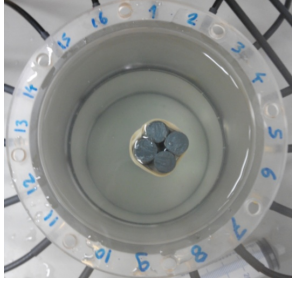
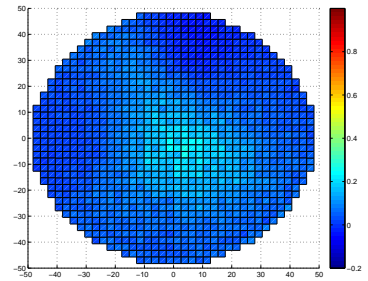
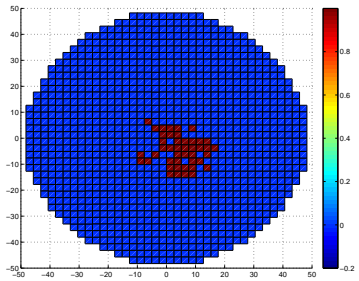
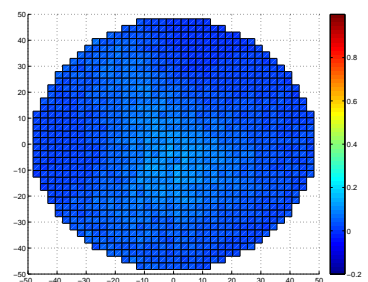
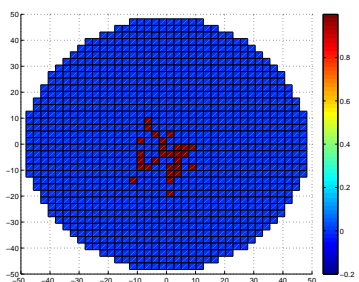
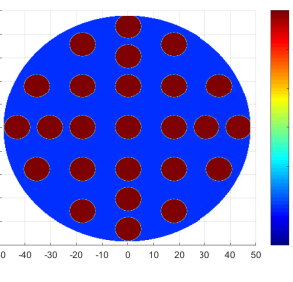
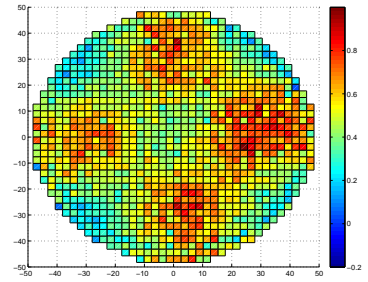
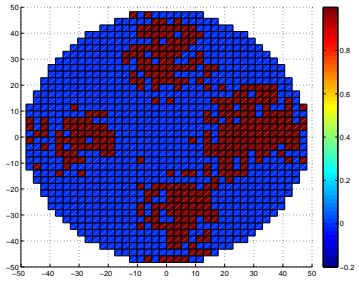
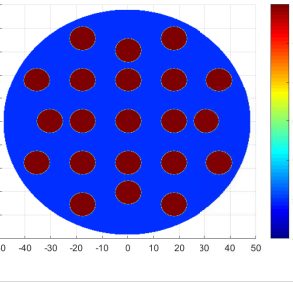
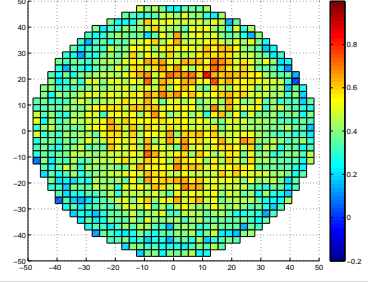
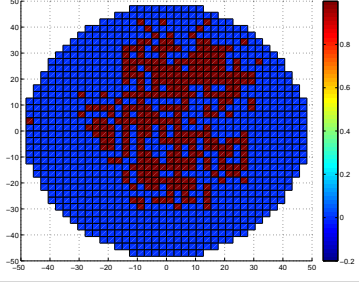
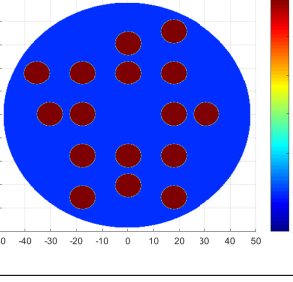
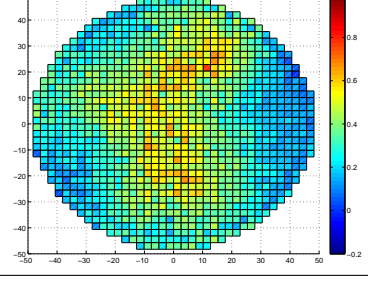
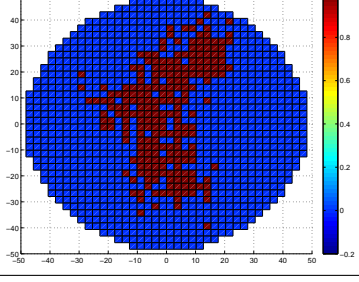
Appendix . Benchmark images

Experiment	Real/Estimate VF [%]	Real image	Tomogram	Binary image
n°23	16%/16,0%			
n°24	16%/16,5%			
n°25	16%/19,7%			
n°26	16%/22,8%			
n°27	0%/-0,1%			

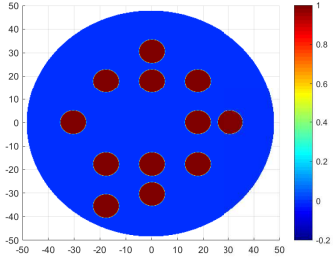
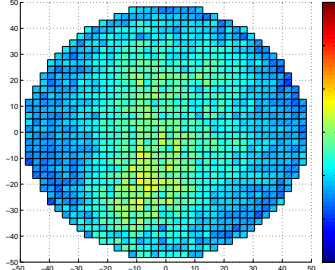
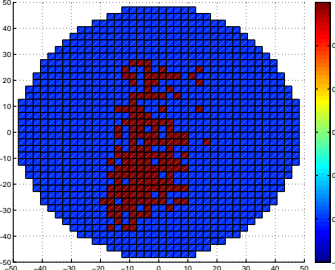
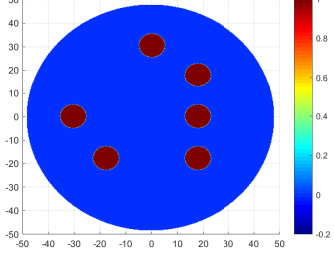
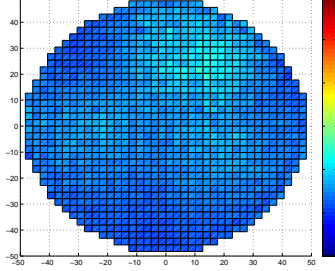
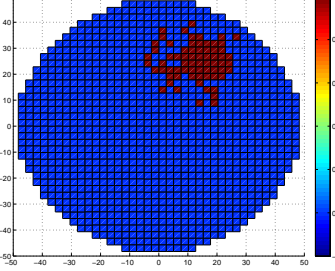
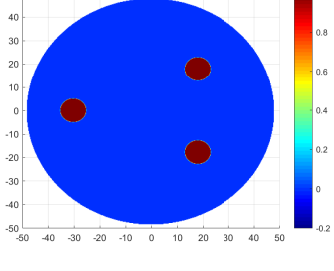
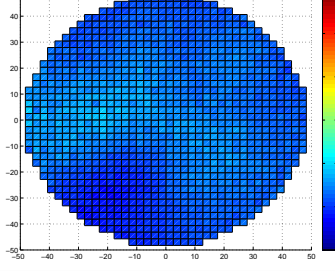
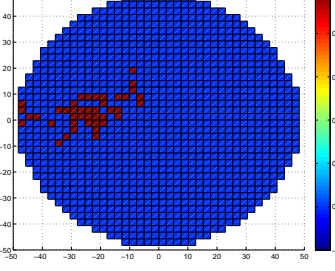
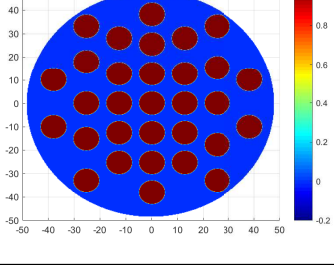
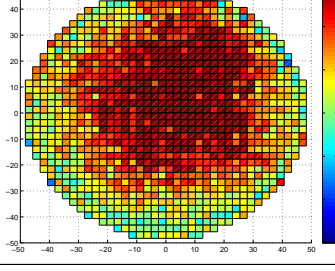
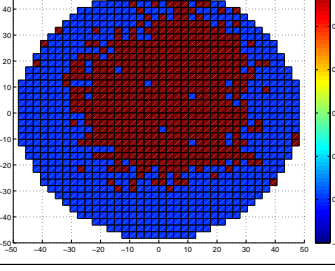
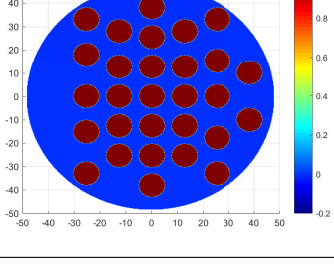
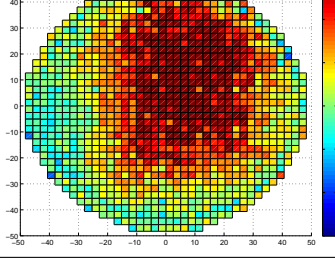
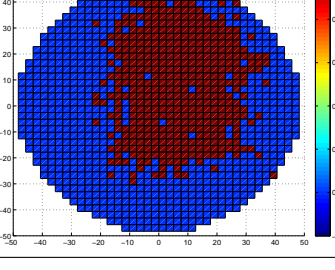
Experiment	Real/Estimate VF [%]	Real image	Tomogram	Binary image
n°28	72%/99,1%			
n°29	52%/88,0%			
n°30	40%/64,5%			
n°31	35%/51,3%			
n°32	30%/40,5%			

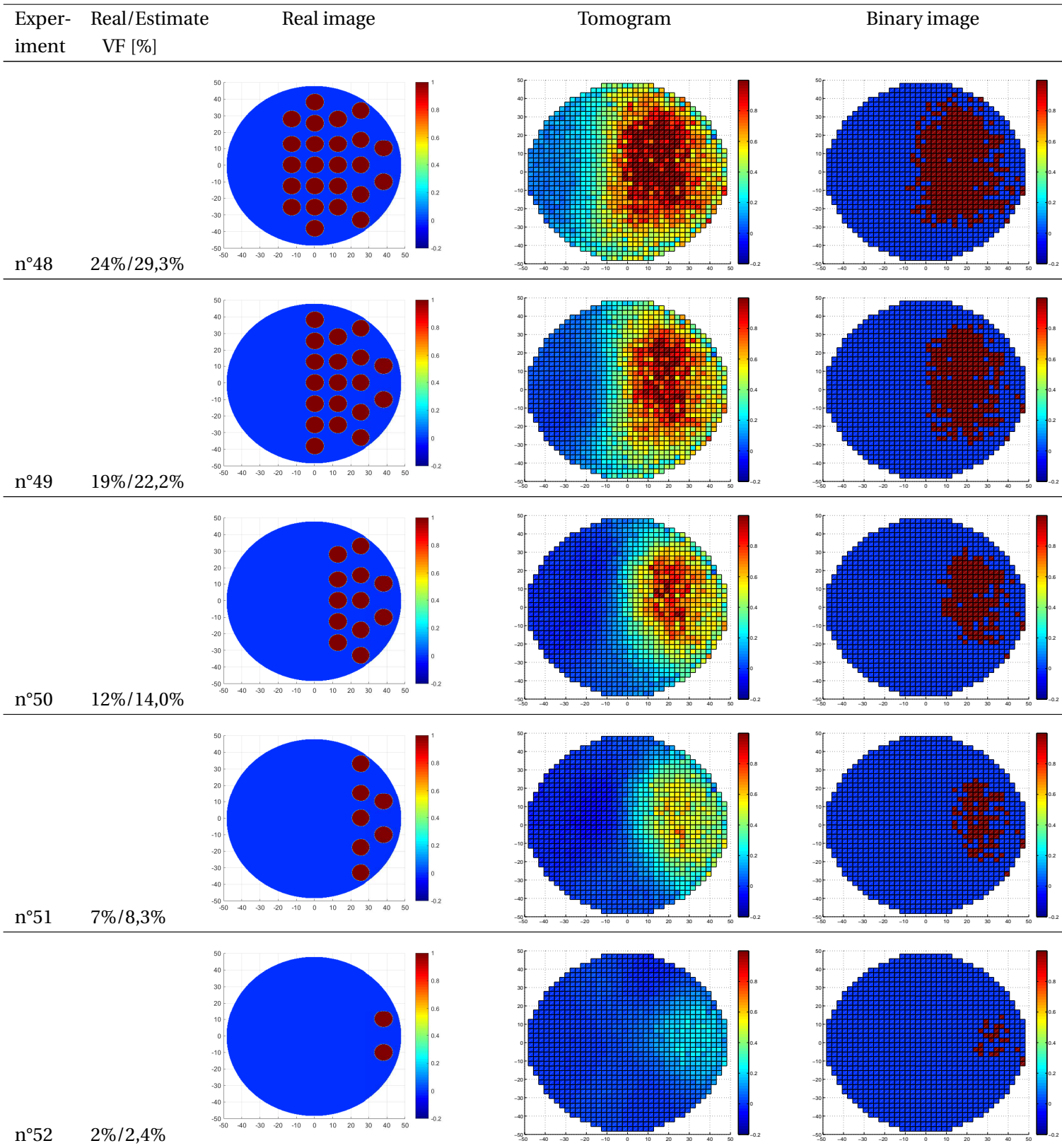
Appendix . Benchmark images

Experiment	Real/Estimate VF [%]	Real image	Tomogram	Binary image
n°33	25%/33,9%			
n°34	20%/23,3%			
n°35	15%/15,3%			
n°36	10%/8,3%			
n°37	5%/4,4%			

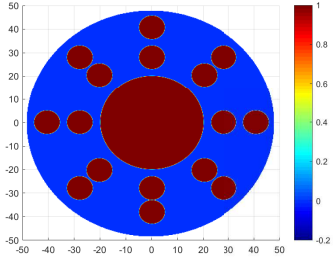
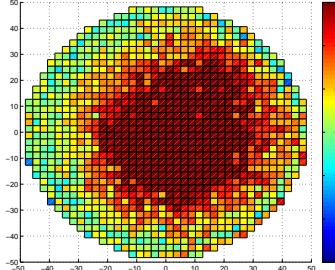
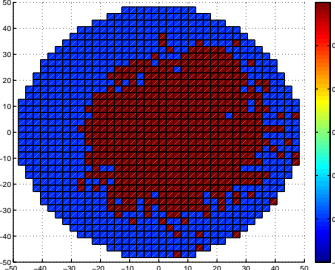
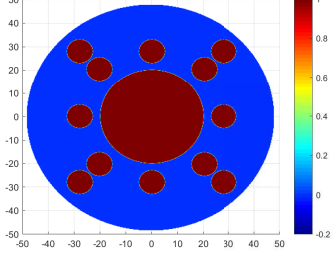
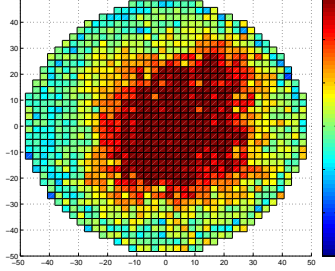
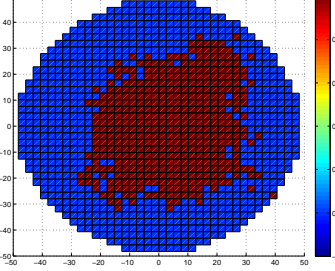
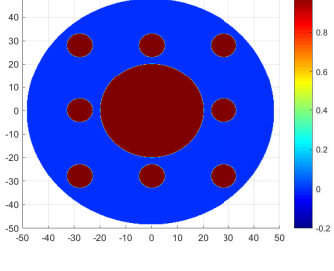
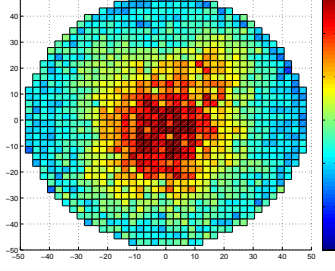
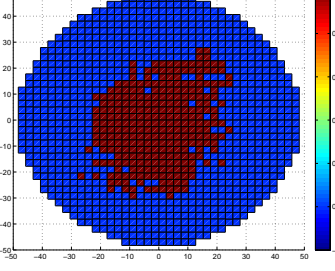
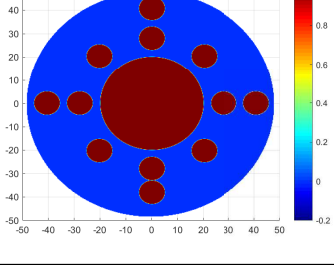
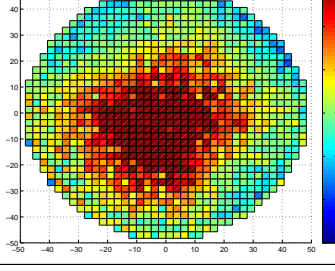
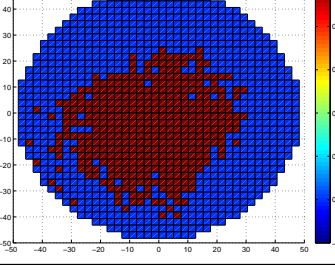
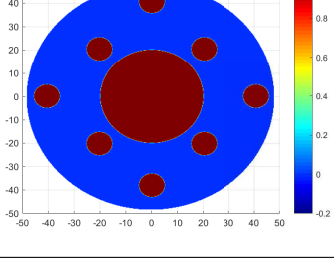
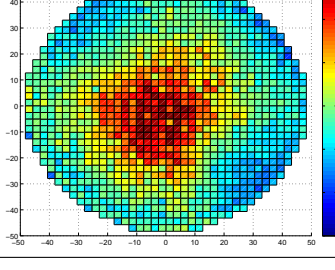
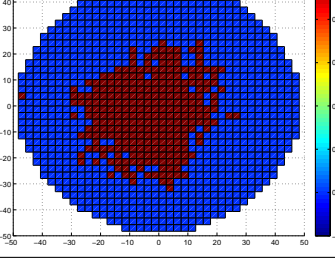
Experiment	Real/Estimate VF [%]	Real image	Tomogram	Binary image
n°38	4%/3,7%			
n°39	3%/2,4%			
n°40	25%/29,1%			
n°41	21%/24,3%			
n°42	16%/19,1%			

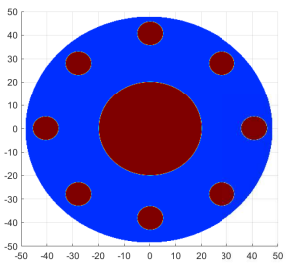
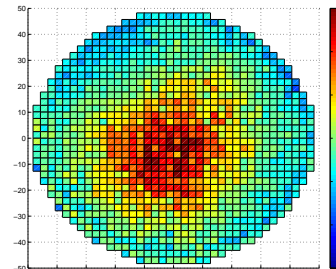
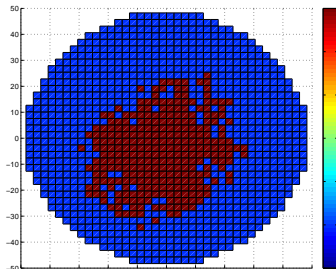
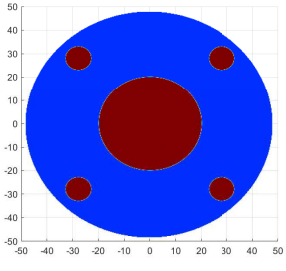
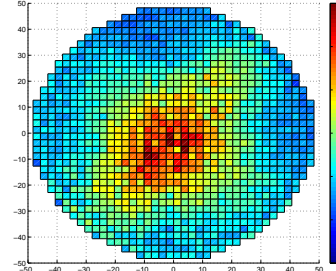
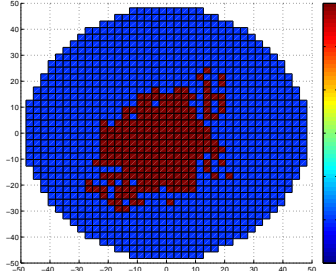
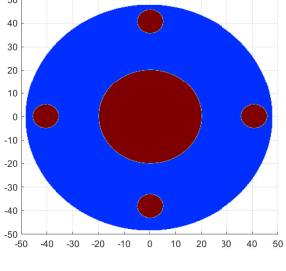
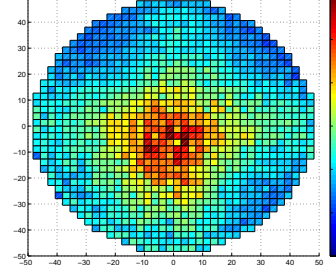
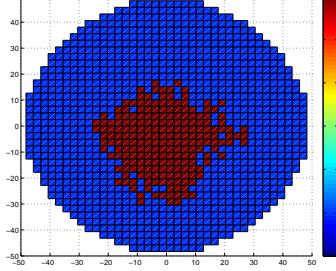
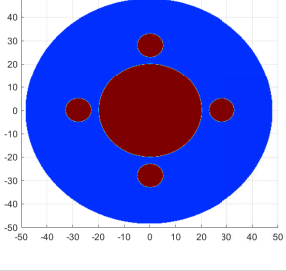
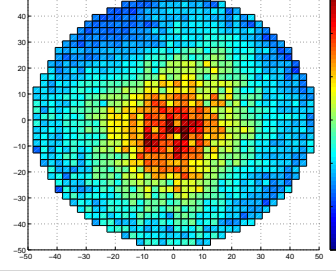
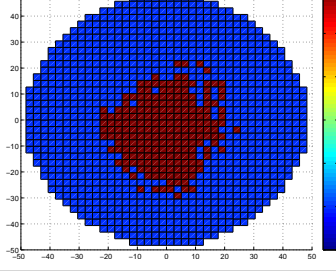
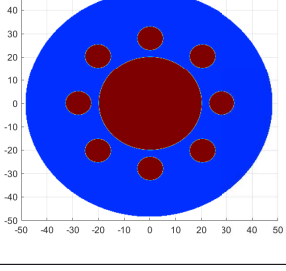
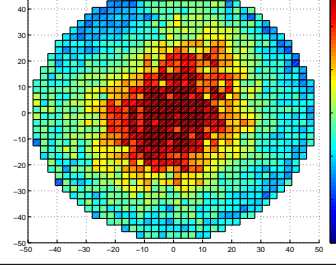
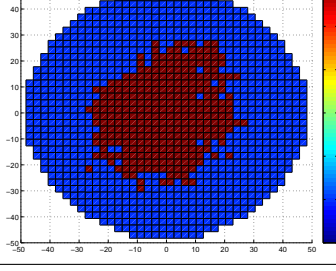
Appendix . Benchmark images

Experiment	Real/Estimate VF [%]	Real image	Tomogram	Binary image
n°43	12%/13,0%			
n°44	6%/5,8%			
n°45	3%/3,5%			
n°46	31%/42,2%			
n°47	29%/37,9%			



Appendix . Benchmark images

Experiment	Real/Estimate VF [%]	Real image	Tomogram	Binary image
n°53	32%/43,0%			
n°54	28%/35,7%			
n°55	24%/23,6%			
n°56	28%/32,8%			
n°57	24%/23,3%			

Experiment	Real/Estimate VF [%]	Real image	Tomogram	Binary image
n°58	24%/23,9%			
n°59	20%/18,2%			
n°60	20%/17,6%			
n°61	20%/17,4%			
n°62	24%/25,4%			

Appendix . Benchmark images

